

Photonic Band Gap Structures for Superconducting Radio-frequency Particle Accelerators

by
Sergey A. Arsenyev

Submitted to the Department of Nuclear Science and Engineering
in partial fulfillment of the requirements for the degree of
Doctor of Philosophy in Nuclear Science and Engineering
at the

MASSACHUSETTS INSTITUTE OF TECHNOLOGY

September 2016

© Massachusetts Institute of Technology 2016. All rights reserved.

Author
Department of Nuclear Science and Engineering
June 23, 2016

Certified by.....
Richard J. Temkin
Senior Research Scientist, Department of Physics
Thesis Supervisor

Certified by.....
Evgenya Simakov
Physicist IV, Los Alamos National Laboratory
Thesis Supervisor

Certified by.....
Anne White
Associate Professor, Nuclear Science and Engineering
Thesis Reader

Accepted by.....
Ju Li
Battelle Energy Alliance Professor of Nuclear Science and Engineering
Professor of Material Science and Engineering
Chair, Department Committee on Graduate Theses

Photonic Band Gap Structures for Superconducting Radio-frequency Particle Accelerators

by

Sergey A. Arsenyev

Submitted to the Department of Nuclear Science and Engineering
on June 23, 2016, in partial fulfillment of the
requirements for the degree of
Doctor of Philosophy in Nuclear Science and Engineering

Abstract

This thesis presents the design and testing of the first multi-cell superconducting accelerating cavity with a photonic band gap (PBG) coupler cell. The structure serves as a building block for superconducting radio-frequency (SRF) electron accelerators. It has five accelerating cells: four cells of elliptical shape, commonly used for SRF cavities, and one PBG cell in the middle.

The purpose of the PBG cell is to damp unwanted Higher-Order electromagnetic Modes (HOMs) in the structure. Strong HOM damping is highly desirable for SRF cavities because it increases maximum achievable beam current by reducing the negative effect that HOMs have on the propagating electron beam. In the presented structure, effective HOM damping is achieved because of the inherent frequency selective properties of the PBG cell.

The HOM spectrum in the five-cell cavity was carefully analyzed using eigenmode and wakefield simulations with good agreement between the two methods. The simulations showed that most of the dangerous HOMs were damped to fairly low external quality factors on the order of $10^2 - 10^4$. This in principle implies that the new multi-cell cavity will support much higher beam currents than achievable in conventional SRF cavities that are not optimized for high-current operation. The improved HOM damping does not significantly compromise the accelerating properties of the cavity which are comparable to those of the cavities that only use the elliptical cells. Additionally, the PBG cavity does not need HOM couplers on the beam-pipe sections of the structure, and hence for the same amount of acceleration has a shorter length in the direction of the propagating beam.

The five-cell cavity was fabricated of high purity niobium. Fabrication and tuning mechanisms were successfully tested on a copper prototype before being implemented for the niobium cavity. The accelerating gradient profile in the tuned niobium cavity matched the desired profile within a 5% accuracy.

Two cryogenic tests were conducted with the five-cell cavity. The first test did not succeed due to a problem with the low quality factor of the cavity's accelerating mode. The problem was identified as a poor waveguide joint in the fundamental power cou-

pler. Modifications were made to the waveguide joint and a second cryogenic test was conducted. In the second test, the high cavity quality factor was demonstrated at the temperature of 4.2 K for accelerating gradients up to 3 MV/m. The measured value of the cavity's quality factor with all ports closed was 1.55×10^8 , in agreement with the prediction. This agreement indicated that the implemented surface treatment was effective in the cavity, including the complex PBG cell. No cavity leaks were observed during the tests in superfluid helium, proving the reliability of the fabrication process which included difficult electron-beam welds. No hard barriers in the accelerating gradient were observed during the test, indicating the absence of fundamental limits to cavity's operation for the gradient of at least several MV/m.

A series of room-temperature experiments were conducted to measure external quality factors of six dangerous HOMs in the fabricated five-cell cavity. The measurements agreed with the simulations, showing all of the measured Q-factors below 3×10^3 . Effective HOM damping, together with the ability to support accelerating gradients of multiple MV/m at cryogenic temperatures, makes the cavity an attractive candidate for future high-current accelerators.

Thesis Supervisor: Richard J. Temkin

Title: Senior Research Scientist, Department of Physics

Thesis Supervisor: Evgenya Simakov

Title: Physicist IV, Los Alamos National Laboratory

Acknowledgments

I want to thank my professional collaborators to whom much of the scientific success of this thesis is owed. My research supervisor at Los Alamos National Laboratory, Dr. Evgenya Simakov, is the person without whom my research project would not be possible. Evgenya was always available for discussions and extremely helpful in all aspects of the research. I am especially grateful for her care about my career development, extending the boundaries of the particular project we worked on.

I thank Dr. Richard Temkin, my MIT supervisor, who is a brilliant scientist and a very good mentor. I was honored to have worked with the “Waves and Beams” group at MIT and I thank all the members of the group for helping with this project. I particularly thank Dr. Michael Shapiro, Dr. Brian Munroe, Dr. Emilio Nanni, and Dr. JieXi Zhang for very useful discussions. Big thanks goes to my office mates Dr. Min Hu, Xueying Lu, and Samuel Schaub. I am also grateful to all of my professors at MIT, including the Plasma Science and Fusion Center, for giving me a broader understanding of science in general.

I would also like to thank the scientists of Los Alamos National Laboratory and Niowave Inc for helping me with the experimental work. Among them, I especially thank Dr. Dmitry Shchegolkov, Dr. Tsuyoshi Tajima, Dr. Brian Haynes, Dr. Frank Krawczyk, Dr. Chase Boulware, Prof. Terry Grimm, and Adam Rogacki. Very much appreciated support and encouragement also came from my family and friends in Russia and my American friends in Massachusetts, New Mexico, and Michigan. Among my friends, special thanks goes to Polina for almost reading this entire thesis, and motivating me to stop procrastinating during our tea breaks at “Flour”.

Contents

1	Introduction	31
1.1	Energy-recovery-linacs	34
1.2	Superconducting RF accelerators	37
1.3	Introduction to photonic band gap structures	41
1.4	Summary of thesis	45
2	Theory	47
2.1	Wakefields and higher order modes	47
2.1.1	Relationship between wake impedance and deflecting voltages	51
2.1.2	Higher order mode damping in energy-recovery-linacs	53
2.2	Photonic band gap structures	54
2.3	RF superconductivity	57
2.3.1	RF surface resistance	60
2.3.2	Surface fields	61
2.4	Summary	69
3	Design and simulations	71
3.1	Photonic band gap lattice	71
3.1.1	Choice of the lattice parameter	72
3.1.2	Truncation of the photonic band gap structure	73
3.1.3	Optimization of the photonic band gap lattice	76
3.1.4	Shape of the photonic band gap rods	80
3.2	Design of the photonic band gap cell	82

3.3	Design of the elliptical cells	85
3.4	Design of the five-cell cavity	88
3.4.1	Circuit model	89
3.4.2	Incorporating the photonic band gap cell into the five-cell cavity	93
3.4.3	Accelerating properties of the five-cell cavity with a photonic band gap cell	95
3.5	Simulations of higher order modes	97
3.5.1	Wakefield solver	98
3.5.2	Eigenmode solver	100
4	Fabrication and tuning of the niobium five-cell cavity	105
4.1	Fabrication of the cavity components	106
4.2	Tuning and assembling the cavity	107
4.3	Preparation to cryogenic tests	113
4.4	Fabrication of RF loads and sliding shorts	116
4.5	Summary	118
5	Higher order mode damping measurements	121
5.1	Measurement setup	122
5.2	Identifying the modes	124
5.3	Quality factor measurements	130
5.3.1	Measurements with RF loads	133
5.3.2	Measurements with sliding shorts	134
5.4	Summary	137
6	Cryogenic tests of the niobium five-cell cavity	139
6.1	First cryogenic testing at LANL	141
6.2	Identification of the problem and modification to the joint design . .	148
6.3	Second cryogenic testing at Niowave Inc.	152
6.4	Summary	157

7 Discussion and future work	159
7.1 Summary of results	159
7.2 Future work	162
A Simulations setup	165
A.1 CST wakefield simulations	165
A.2 HFSS eigenmode simulations	168
A.3 HFSS driven modal simulations	173

List of Figures

1-1	Livingston plot of accelerated particle energy versus year of accelerator commissioning [6].	32
1-2	An overview graphic of the planned ILC based on the accelerator design of the Technical Design Report.	33
1-3	A diagram showing an ERL-based X-ray source.	35
1-4	An example of superconducting RF cavities: two 1500 MHz 5-cell niobium cavities adopted by TJNAF (formerly CEBAF).	37
1-5	A simplified diagram of an SRF cavity in a helium bath with RF coupling and a passing particle beam. The picture is taken from [31]. . .	38
1-6	Examples of photonic crystals in one, two and three dimensions. Different colors represents different dielectric constants in space [3]. . . .	41
1-7	Opal's natural photonic band gap structure is responsible for its iridescent light. The picture is taken from [49].	42
1-8	Internal structure of photonic crystal fibers is a 2D PBG array.	42
1-9	An example of an RF cavity formed by a removed rod in a photonic crystal. The color is showing the magnitude of the electric field. Metal parts are shown in white.	43
1-10	A schematic diagram of the first superconducting PBG cavity [61]. The beam passes in the up-down direction through the holes in the walls. Microwave absorber is placed around the periphery of the structure. . .	44
1-11	The fabricated niobium 5-cell accelerating cavity with a coupler PBG cell in the middle. The cavity resonates at the RF frequency of 2.1 GHz.	45

2-1	Numerically calculated electric wakefields generated by a passing bunch in a PETRA cavity at DESY [68]. The beam moves along the dashed line on an axis of cylindrical symmetry. The solid lines connect the vectors of the electric field.	48
2-2	A graphical representation of the quantities used in Equations 2.1 and 2.2 (from [67]). An ultrarelativistic source charge q_1 passes through a geometric perturbation (RF cavity). A following test charge q can be affected by the wakefield excited by the source charge.	49
2-3	Typical frequency spectrum of the real part of an accelerator cavity wake impedance from [67].	50
2-4	Fundamental unit cell is shown in a dashed line for the case of the 2D triangular lattice. The picture is taken from [73].	55
2-5	Dispersion relation including several TM and TE modes of the lowest normalized frequency of the triangular PBG lattice with $a/b = 0.15$. Yellow shadow indicates the band gap.	57
2-6	Global band gap map for the TE modes (top) and the TM modes (bottom) for the triangular lattice. The plotted map is based on numerical computations by E. Smirnova [73]. A choice of parameter a/b imposes a vertical dashed line that slices through the regions of propagation and no propagation (the case $a/b = 0.15$ is shown).	58
2-7	A simplified view of the electron-phonon interaction [31]. An electron moving through the lattice distorts the lattice. The deformed lattice acts on a second electron moving in the opposite direction through the positive charge accumulation.	59
2-8	Surface resistance measured for a 1.5 GHz single-cell niobium cavity plotted as a function of inverse reduced temperature T_c/T [31]. At low temperatures surface resistance is dominated by the residual loss. . .	62
2-9	Normal-conducting regions appearing inside a superconductor at a magnetic field level $H > H_{c1}$. The picture is taken from [31].	63

2-10	Electron trajectories in an elliptical cavity [31]. The charges drift to the equator where multipacting is not possible.	65
2-11	Quenching on the surface of a niobium cavity at the location of a defect [31]. (a) At low field, the temperature in the vicinity of the defect is higher than that in surrounding areas but lower than T_c . (b) As the field is raised, the temperature exceeds T_c , so that the niobium near the defect becomes normal conducting, and the power dissipation increases unstably.	66
2-12	RF power levels for a cavity during quenching [31]. The power reflected from the cavity and the power transmitted through the cavity exhibit the saw tooth shape.	67
2-13	Calculated trajectories of emitted electrons in a 5-cell 1.5 GHz cavity [31].	68
3-1	Frequency of eigenmode solutions in an infinite photonic crystal as a function of wave vector in the plane of the crystal. The crystal has a triangular lattice of metal rods with a ratio of the rod radius, a , to the spacing between the rods, b , equal to 0.15. Frequencies are shown for the monopole and the dipole modes with dashed straight lines in a resonator formed by a single removed rod.	73
3-2	An early idea of an open SRF PBG structure with three layers of rods (shown with white dashed lines). Cooling is done through tubes inside the PBG rods and the walls.	74
3-3	A drawing of the 5-cell SRF cavity with a PBG cell "closed" in the transverse plane with a metal wall. The entire structure is made of pure niobium	75
3-4	PBG cell as seen from the Z axis pointing along the beam trajectory. The vacuum region is shown in blue.	76
3-5	Optimized dielectric PBG cavity from [53]. Color is showing normalized electric field of the confined mode.	77

3-6	Initial and optimized positions of the rods in the metal PBG structure (black and red circles, respectively). The scale is arbitrary, the obtained results apply to a structure of any size.	78
3-7	(a) Regular metal triangular lattice, monopole mode, $Q=3150$. (b) Regular metal triangular lattice, dipole mode, $Q=46$. (c) Optimized metal triangular lattice, monopole mode, $Q=3220$. (d) Optimized metal triangular lattice, dipole mode, $Q=10.7$. Simulation setups are described in Appendix A and additional files are provided in Supplemental Materials [1].	79
3-8	Elliptical rod PBG structure for breakdown testing at SLAC [82]. . .	81
3-9	Change in the shape of the inner rods of the PBG cavity to reduce peak surface magnetic fields [85].	81
3-10	The vacuum region enclosed by the PBG cell. One quarter of the cell is cut out to show the structure. The beam goes along the z -axis. . .	83
3-11	Main dimensions of the PBG cell (top) and dimensions of the waveguides attached to the cell (bottom). The vacuum region is shown in blue. The pictures are taken from HFSS eigenmode simulations provided in Supplemental Materials [2].	84
3-12	The vacuum region enclosed by a cell of the elliptical “low-loss” shape. One quarter of the cell is cut out to show the structure. The beam goes along the z -axis. The picture is taken from HFSS eigenmode simulations provided in Supplemental Materials [2].	87
3-13	The dimensions of the elliptical cells of the “low-loss” shape [44], scaled to the frequency of 2.1 GHz. (a) an elliptical cell not located at the end of the 5-cell cavity. (b) a “trimmed” elliptical cell at the end of the 5-cell cavity.	87
3-14	Sketch of the electric field lines of the π -mode of a 5-cell accelerating cavity [31].	88
3-15	A circuit model representing the 5-cell accelerating cavity.	90

3-16	Design accelerating gradient profile, compared to the profile measured in the welded cavity using the bead-pulling method. The field in the center cell is intentionally lowered to ensure equal peak surface magnetic field in every cell.	94
3-17	Transverse impedance calculated by CST Particle Studio for the electron beam displaced in X direction (a) and Y direction (b). 10 most dangerous modes correspond to the biggest peaks in impedance. Analytical shapes for the peaks were fitted using a MATLAB algorithm presented in Supplemental Materials [7]. Input data for the Figure is provided in Supplemental Materials [6].	99
3-18	Shunt impedances (a) and external Q factors (b) for monopoles and dipoles in the 5-cell PBG cavity obtained in HFSS eigenmode simulations described in Appendix A and Supplemental Materials [4]. Only modes with $R/Q \geq 1\Omega$ are shown. Input data for the Figure is provided in Tables 3.4 and 3.5.	103
3-19	BBU figure of merit $(R/Q)Q_{ext}f$ for the dipole modes for two different cavities: the 9-cell TESLA and the 5-cell PBG. Dipole shunt impedance is in units of Ohms. Simulation data for the TESLA cavity is from Ref [41, 65]. Simulation data for the PBG cavity is taken from Tables 3.4 and 3.5.	104
4-1	Parts of the 5-cell cavity before trim-tuning. All of the elliptical half-cells are trimmed at the equator, where an additional 0.1 inch of material was left on each side for tuning.	106
4-2	Two “dumbbells” used on the opposite sides of the five-cell cavity. Each dumbbells formed by two halves of the elliptical cells welded together at the irises.	107

4-3	(a) Holes for the PBG rods were made in the walls of the PBG cell. (b) The PBG rods were cleaned in ultra-pure water. (c) The rods were welded to the walls of the cell. (d) Waveguide flanges were made and welded to the cell.	108
4-4	The PBG cell is stacked with two half-cells, terminated with metal plates to excite the π -mode (the copper structure is shown in the picture rather than the niobium structure due to the better photograph).	109
4-5	The bead-pull setup for the electric field measurement. The bead is being pulled by a string attached to a small motor. The copper structure is shown in the picture rather than the niobium structure due to the better photograph.	110
4-6	The initial gradient profile for the π -mode, excited in a 3-cell setup of untuned niobium cells from Figure 4-4.	111
4-7	The niobium 5-cell cavity after all the parts were electron-beam welded.	113
4-8	Accelerating gradient profile measured in the welded niobium cavity using the bead-pulling method, compared to the design profile. The field in the center cell is intentionally lowered to ensure equal peak surface magnetic field in every cell.	114
4-9	(a) The niobium cavity just before the buffered chemical polish treatment. The cavity is filled through the pipe with a mix of HF, HNO ₃ , and H ₃ PO ₄ . (b) The cavity is undergoing a high-pressure rinsing cycle after the chemical treatment.	114
4-10	Structure of the FPC waveguide cover for the niobium cavity, made as preparation for cryogenic tests. Niobium-to-niobium contact provides an RF seal, while a "diamond" gasket provides a vacuum seal.	115
4-11	A schematic showing an addition of the helium vessel to the cavity.	116
4-12	The mechanical setup for measuring the tuning capability of the niobium cavity in the helium vessel.	117
4-13	(a) Drawing of the RF load for the FPC. (b) A schematic showing the arrangement of RF loads and tapers.	117

4-14	Sliding short for the FPC waveguide. An aluminum plate with a sliding spring is put inside a piece of WR430 waveguide. The antenna is inserted through a hole in the plate.	118
5-1	A typical setup for HOM damping measurements shown for the copper cavity. The FPC is connected to a waveguide-to-coaxial mode converter. The HOM waveguides are tapered out and terminated with RF loads. Loop antennas are inserted in the beam-pipe and aligned with the central axis.	123
5-2	Comparison between the measurement and the simulation of the S_{21} profile for the X and the Y polarizations. Measured S_{21} for copper cavity was shifted down by 50 dB for illustration purposes. All waveguides were terminated with RF loads. Similarity of the shapes gives an insight on which simulation peaks correspond to the modes in the fabricated cavities. Mode overlapping (merging of two peaks with close frequencies) can be seen for the simulation peaks at around 2.7 GHz for both X and Y polarizations due to the low Q-factors of the modes.	125
5-3	Simulated electric field patterns of the modes corresponding to the six peaks in Figure 5-2 marked with the vertical dashed lines (see Appendix A and additional files in Supplemental Materials [11]). These patterns match with the patterns of the X_1 , X_2 , and X_3 modes simulated in Chapter 3.	128
5-4	Comparison between the two different excitation methods: the two-antenna excitation and the FPC-antenna excitation. The green curve is shifted down by 60 dB illustration purposes. Some peaks exist if the first excitation method is used but disappear in the second method is used. Such modes must have the field pattern prohibiting the FPC-excitation (zero electric field along the X -axis.	129

5-5	Comparison between the bead-pull field measurements (solid green lines) and the simulated profiles (dashed blue lines, see the simulation files in Supplemental Materials [4]) for the monopole modes with frequencies below 3 GHz. Only the 5 passband modes fall within the measured frequency range 0 - 3 GHz.	131
5-6	Comparison between the bead-pull measurements (solid green lines) and the simulated profiles (dashed blue lines, see the simulation files in Supplemental Materials [4]) for the dipole modes with frequencies below 3 GHz. Six of the ten dangerous modes fall within the measured frequency range 0 - 3 GHz. Shapes of the measured curves resemble the shapes of simulated curves, indicating that the identification of the modes in the experimental S_{21} profile is correct.	132
5-7	Comparison between the profile of the S_{21} peaks of the X_1 mode for the two boundary conditions on the waveguides. The cross-shaped markers are used to independently estimate Q-factors for the left and the right parts of the peaks.	134
5-8	An HFSS simulation of damping of the X_2 mode with the FPC sliding short. One-quarter of the structure is shown because of the $X - Y$ and the $X - Z$ symmetry planes. The color is showing the magnitude of the electric field in the $X - Z$ plane. A significant part of the mode's energy is coupled to the waveguide due to the resonance condition between the cavity mode and the waveguide mode.	136
6-1	Phase diagram of ^4He at low temperatures. The dependence of the temperature of liquid helium on pressure (lower red curve) allows varying the temperature in a cryotest by changing the pressure inside the dewar. Superfluid state can be achieved by lowering the dewar pressure below the pressure of the "triple point".	140
6-2	A drawing (a) and a photograph (b) of the 5-cell cavity with the drive probe assembly the pickup probe assembly.	142

6-3	A photo of the cryostat and a schematic of the RF setup used for the vertical testing at LANL. The cryostat is a well 2.97 m deep and 0.965 m in diameter, covered with a lid in the photo. The RF setup includes a standard for vertical testing phase-lock loop to lock on the cavity's frequency (picture is taken from [31]).	143
6-4	Simulated gradient profiles for the 5 passband modes in the five-cell cavity (see the simulation files in Supplemental Materials [4]).	144
6-5	Photographs of the inside of the cavity, taken during the inspection. No visible defects were found.	145
6-6	Power reflected from the cavity when excited with a pulse at the frequency of the π -mode. Decay time was calculated by measuring the slope of the curve just after the pulse was turned on (by comparing the points given by the intersections of the red and the blue lines). The power is measured in arbitrary units.	146
6-7	Cavity's quality factor for different modes as a function of the peak surface electric field at 4K. The drive probe was adjusted to provide near critical coupling to the $2\pi/5$ and $4\pi/5$ modes, or max achievable coupling for π and $3\pi/5$ modes.	147
6-8	Magnitude of the E field of the trapped waveguide mode in a plane that goes through the center of the PBG cell. The mode is an effective tool in diagnosing the low Q problem. The picture is taken from an eigenmode simulation described in Supplemental Materials [9].	150
6-9	The modified niobium gasket used in the FPC joint. A part of the gasket was cut out to form a "tooth" that gets pressed against the flange.	151
6-10	A photograph of the 2.1 GHz 5-cell cavity in the helium vessel ready to be placed in a cryostat in preparation for the second cryogenic test.	153
6-11	A schematic and a photograph of the cryostat used in the second cryogenic test.	154

6-12	Unloaded Q-factor and accelerating gradient in the accelerating mode, obtained during the second test at Niowave Inc. The helium bath temperature was 4.2 K. The point at $E = 4.6$ MV/m corresponds to the expected value of Q_0 (listed in Table 6.3) assuming no Q-degradation, and the accelerating gradient estimate based on the available RF power and measured losses in the transmission lines.	156
7-1	Shunt impedances (a) and external Q factors (b) for monopoles and dipoles in the 5-cell PBG cavity (simulation). Most of the high-impedance HOMs are damped to fairly low external Q-factors on the order of 10^3 (the green arrows show the Q-factors corresponding to the two highest-impedance dipole modes). Strong HOM damping means higher achievable beam current in the accelerator.	160
7-2	Unloaded Q-factor and accelerating gradient in the accelerating mode, obtained during the second cryogenic test. The helium bath temperature was 4.2 K. The point at $E = 4.6$ MV/m corresponds to the expected value of Q_0 assuming no Q-degradation, and the accelerating gradient estimate based on the available RF power. The expected accelerating gradient was not achieved possibly due to some unaccounted losses in the transmission lines. However, the cavity performed as expected (measured Q agreed with the expectation) at the fields up to 3 MV/m.	161
7-3	A Solid Works drawing of a cryomodule assembly housing the 5-cell cavity, proposed as a continuation of the project.	163
7-4	Concept of the "horizontal test" to demonstrate acceleration of an electron beam and probe HOM damping.	164
A-1	A diagram of an example wakefield simulation, taken from the CST user manual. The color shows the magnitude of the the electric field.	166

A-2	The structure used in the wakefield simulations. The vacuum region is shown in blue. The waveguide ports are shown with pink lines. The beam path is shown with blue and orange arrows (the path is displaced in X in this picture).	167
A-3	Geometrical design for the simulations used in Section 3.1.3. A 60° slice of the structure is used to simulate the monopole mode (a), and and a 180° slice was used to simulate the dipole mode (b). Vacuum regions are shown in blue. PML volumes are shown in pink. “Master” and “slave” boundary conditions were used with the appropriate phase advances.	171
A-4	Geometrical design for the simulations used in Section 3.5.2. A quarter of the structure is simulated to take advantage of the symmetry planes. The waveguides are covered with PML. The yellow line was used for R/Q calculation (see Section 3.5.2).	171
A-5	Geometrical design for the simulations used in Section 5.2. Half of the structure is used in the simulations to take advantage of the $X - Z$ symmetry plane. Vacuum regions are shown in blue. PML volumes are shown in pink. The two ports are defined on the coss-sections of the coaxial lines.	174

List of Tables

3.1	Comparison between diffractive Q-factors for the first monopole and the first dipole modes in the original and the optimized geometry . . .	78
3.2	Final dimensions of the PBG cell, shown in Figure 3-11.	86
3.3	Accelerating properties of the 5-cell cavity with a PBG cell compared to the accelerating properties of the cavity with 5 elliptical "low-loss" cells from [44]. The values for the PBG cavity were obtained using eigenmode simulations provided in Supplemental Materials [2].	96
3.4	Simulation results for the dipole modes with $(R/Q)^d > 1\Omega$	101
3.5	Simulation results for the monopole modes with $R/Q > 1\Omega$	102
4.1	Amounts trimmed off the equators of the half-cells.	112
5.1	Differences in frequencies of the modes identified in the niobium cavity from the design frequencies (from Tables 3.4 and 3.5).	127
5.2	Comparison between simulated and measured external Q factors for 6 of the dangerous HOMs.	135
6.1	Theoretical and measured unloaded Q Factors for the passband modes.	148
6.2	Theoretical and measured quality factors for the trapped waveguide mode. The theoretical Q_0 is based on the measured conductivity σ and the simulated G constant (see the simulation files in Supplemental Materials [9]).	151

6.3	Comparison between the low-field Q_L measured at the temperature of 4.2 K and the expected values of Q_L based on the estimated Q_{ext} and Q_0 for different modes.	155
A.1	Parameters used in the wakefield simulation described in Section 3.5.1.	169
A.2	Parameters for the eigenmode simulations described in Section 3.1.3.	172
A.3	Parameters for the eigenmode simulations described in Section 3.5.2.	172
A.4	Parameters for the driven modal simulations described in Section 5.2.	174

Glossary

Accelerating gradient, $\langle E \rangle$

One of the main characteristics of an accelerating structure. $\langle E \rangle$ is defined as the amount of acceleration in the units of Volts that a charged particle gets while traversing the structure, divided by the lengths of the accelerating structure.

BBU

Beam break-up. BBU is caused by the interaction of deflecting modes with a particle beam, leading to effective emittance growth and eventually a loss of the beam in the walls of the accelerating structures.

Beam-pipe

A pipe connecting accelerating structures, necessary to create a vacuum in the beam line.

Brilliance

A term that applies to light sources such as the synchrotron, the free electron laser, or the inverse Compton light source. Brilliance is defined as the number of produced photons in the light source with a wavelength within 0.1% of the central wavelength, per unit time per unit solid angle per unit area.

Bunch

An ensemble of charged particles traveling in an accelerator.

Coupling β factor

A number that describes the strength of coupling between an electromagnetic mode in a structure and an RF coupler (e.g. waveguide) attached to the structure. β is defined as

$$\beta = \frac{Q_0}{Q_{ext}},$$

where Q_0 is the unloaded Q-factor and Q_{ext} is the external Q-factor related to the power loss through the coupler.

Critical coupling

The case when the coupling β factor is equal to one. It means that no RF power is reflected from the coupled structure.

CW

Continuous wave. The CW operation of an accelerating structure means that the RF power is being supplied to the structure continuously (as opposed to the pulsed regime) and the particle beam is being produced continuously (as opposed to single bunches).

Dipole mode

An electromagnetic mode in an RF cavity that has one angular variation in the plane perpendicular to the axis of the beam.

Driver linac

A linear accelerator that is used to supply accelerated particles to a particle collider or a light source.

E-boundary

A boundary condition used in electromagnetic simulations. This condition, defined on a plane, requires the vector of the electric field to be perpendicular to the plane.

Eigenmode simulation

A type of numerical simulation that aims to solve Maxwell's equations and find natural modes (eigenmodes) in a closed RF structure.

Emittance, ϵ

A term that characterizes the internal structure and divergence of an accelerated particle beam. Emittance is defined as the area that the beam occupies in the transverse or the longitudinal (with respect to the beam's trajectory) phase space. In the transverse phase space the emittance ϵ is proportional to the area of an ellipse enclosing the beam in the phase space

$$\epsilon = 1/\pi \int_{\text{ellipse}} dx dx',$$

where x is a transverse coordinate and x' is the corresponding angle of motion with respect to the beam's trajectory.

ERL

Energy recovery linac. A type of a linear accelerator that "recycles" the energy of the

accelerated particles by slowing the particles down and generating RF power after the particles were used for generating light (in a light source) or in collisions (in a particle collider).

Field emission

Field emission is the effect caused by the emission of electrons from the regions of the high electric field on the surface of an RF cavity. The emitted electrons travel in the RF fields of the cavity and impact the cavity's surface. This leads to excessive heating and production of X-rays.

Fundamental power coupler (FPC)

A waveguide or a coaxial line used to feed RF power into an accelerating structure.

H-boundary

A boundary condition used in electromagnetic simulations. This condition, defined on a plane, requires the vector of the electric field to be strictly parallel to the plane.

HOM

A higher order mode. An HOM is an electromagnetic mode with a frequency higher than the frequency of the operating (accelerating) mode.

Linac

Short for the linear accelerator. In a linear accelerator, a particle beam is accelerated along a straight line, as opposed to a circular accelerator.

Luminosity, L

A term that applies to particle colliders. L is defined as the number of collisions between the accelerated particles, per unit area per unit time.

Monopole mode

An electromagnetic mode in an RF cavity that has zero angular variation in the plane perpendicular to the axis of the beam.

Multipacting

Multipacting in RF structures is a resonant process in which a large number of electrons build up spontaneously, absorbing RF power.

PBG

Photonic band gap. A frequency gap between bands in a dispersion diagram for a

periodic structure. An electromagnetic wave cannot propagate in a periodic structure if its frequency is in the band gap.

Perfectly matched layer (PML)

PML is used in electromagnetic simulations to create a no-reflection boundary. Properties of the layer are chosen to cancel out reflection for the specific geometry [93].

Q-factor

A number that describes the decay of an electromagnetic mode in a structure. Defined as the number of periods it takes for the amplitude of the mode's energy to decay by a factor of e . Can also be written as

$$Q = \frac{\omega U}{P_{loss}},$$

where ω is the angular frequency of the mode, U is the electromagnetic energy stored in the mode, and P_{loss} is the power loss due to Ohmic loss, radiation, etc.

Loaded (total) Q-factor Q_L

The Q-factor of an electromagnetic mode due to all kinds of losses in the cavity, including Ohmic loss and radiation loss.

Unloaded Q-factor Q_0

The Q-factor of an electromagnetic mode due to only the Ohmic loss in the walls of the RF cavity, as opposed to the total Q-factor that includes losses of all kinds.

External Q-factor Q_{ext}

The Q-factor of an electromagnetic mode that only includes the power loss to an external coupler (e.g. waveguide). It is different from the total Q-factor that includes losses of all kinds.

Quenching (thermal breakdown)

Quenching is a sudden transition from the superconducting state to the normal conducting state due to heating in "defects" on the surface of a superconducting cavity. Quenching results in a sharp drop in the RF cavity unloaded quality factor.

Real estate gradient

Same as accelerating gradient, but averaged over the whole length of an accelerator,

including non-accelerating structures, e.g. HOM dampers. The real estate gradient characterizes the whole accelerator as opposed to an accelerating structure.

RF

Radio frequency. A range of frequencies from 3 kHz to 300 GHz.

S-parameters

S-parameters relate output signals from a structure (e.g. an accelerating cavity) to the input signals. For a two-port system, there are four S-parameters: S_{11} , S_{12} , S_{21} , and S_{22} . In our case, the indices indicate the output and the input waveguide or coaxial ports of the cavity.

SRF

Superconducting radio-frequency. The acronym SRF is used to describe a part of accelerator science and technology that involves the application of electrical superconductors to radio frequency accelerating structures.

TESLA cavity

A superconducting RF 9-cell accelerating cavity [65] developed for the International Linear Collider [9].

Wake impedance, $\mathbf{Z}(\omega)$

The Fourier spectrum of wake potential $\mathbf{w}(s)$ with respect to the distance between the bunches s . Wake impedance $\mathbf{Z}(\omega)$ shows the frequency (ω) content of a wakefield and is used to analyze the impact of individual HOMs on the beam. Longitudinal and transverse wake impedances are mathematically defined in Equations (2.3) and (2.4).

Wake potential, $\mathbf{w}(s)$

A quantity that describes the strength of interaction between a test bunch and a wakefield excited by a source bunch. Wake potential $\mathbf{w}(s)$ is a function of the distance between the source bunch and the test bunch s . Longitudinal and transverse wake potentials are mathematically defined in Equations (2.1) and (2.2).

Wakefield

Electromagnetic fields excited in an RF structure by a passing particle beam (see also: HOM).

Wakefield simulation

A type of numerical simulation that aims to solve Maxwell's equation in the time-domain using a passing particle beam as a source of excitation.

Chapter 1

Introduction

Particle accelerators constitute a very important part of modern-day science. Applications of particle acceleration are incredibly diverse and include industrial applications, medicine, and studying fundamental particle physics, condensed matter physics, material science, and biology. In this thesis, a new photonic band gap (PBG) structure resonating at an RF frequency is developed for use in particle accelerators. The remainder of this Chapter introduces basic concepts and terminology used to understand particle accelerators.

For example, a particular kind of accelerators, particle colliders, is exclusively used for studying high-energy physics. By colliding particle beams of extremely high temperatures, scientists can simulate the events that happened shortly after the Big Bang. High energy physics is also of great interest for verifying the currently dominant theory describing fundamental particles and fields, the Standard Model.

The Standard Model, sometimes regarded as “the theory of almost everything”, is currently the closest model to a complete theory of particle interactions. It continues to demonstrate success in accurately predicting diverse experimental results. In the Model, all elementary particles are divided into 12 fermions (quarks and leptons), 4 gauge bosons, and the Higgs boson. The Higgs boson, predicted by the Standard Model decades ago, was finally discovered in ATLAS and CMS detectors of the Large Hadron Collider (LHC) at CERN [1, 2] in 2012. This discovery marked a great physics breakthrough of the 21st century [3, 4]. Future applications of particle collid-

ers include making more precise measurements of the properties of the fundamental particles [5] and possibly answering the questions on the origin of dark matter.

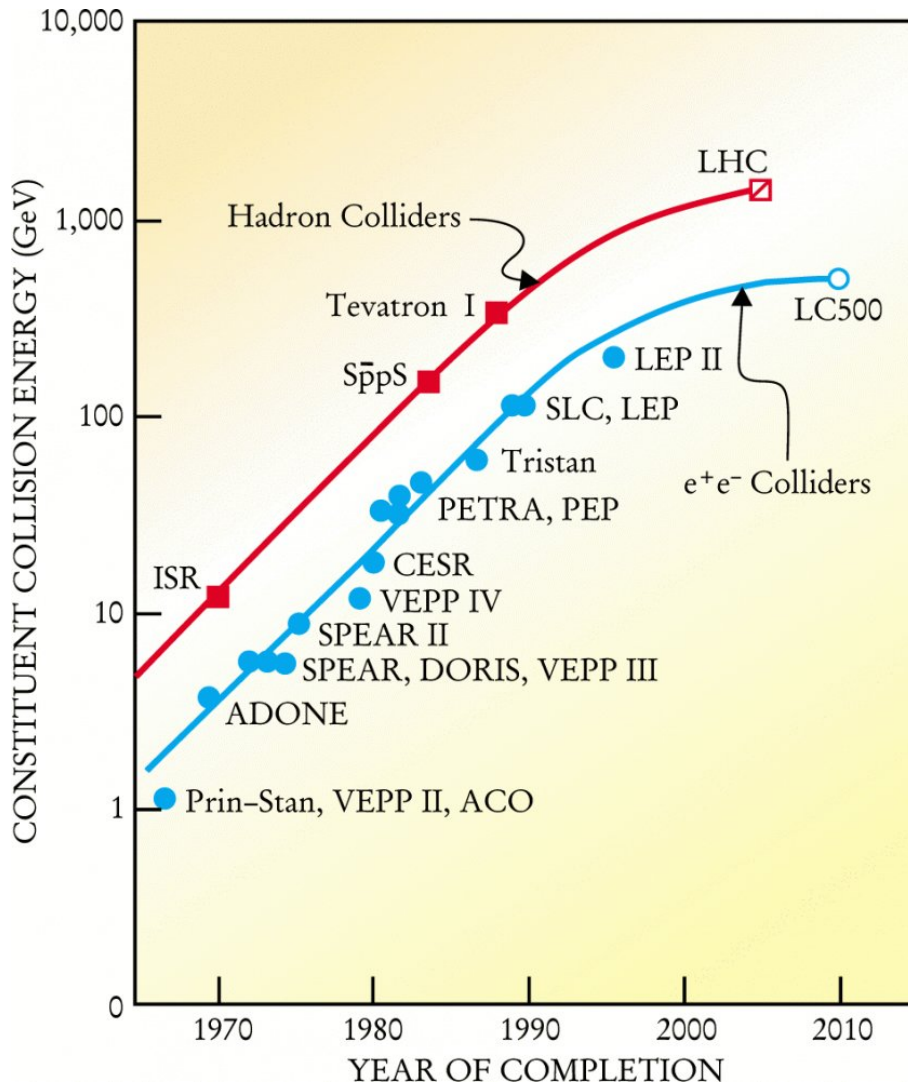


Figure 1-1: Livingston plot of accelerated particle energy versus year of accelerator commissioning [6].

Some of the most important parameters of particle colliders are collision energy and luminosity, the latter defined as the number of collisions per unit area per unit time. Progress towards higher collision energy of particle accelerators for high-energy physics applications can be summarized in the “Livingston” plot shown in Figure 1-1. The figure plots particle energy against the year the accelerator was commissioned. In the plot, particle colliders are separated into two major families: hadron colliders

and lepton colliders.

As can be seen in Figure 1-1, higher collision energies can be achieved by accelerating heavy particles (hadrons) in circular machines. Updates to the current energy frontier colliders like LHC promise to achieve even higher energy and luminosity [7]. However, hadron collisions are not “clean”, meaning that the colliding particles are not elementary particles, but instead, consist of quarks. This makes results of hadron collisions hard to analyze.

On the other hand, acceleration of lighter particles (leptons) allows “cleaner” collisions. However, achieving collision energies on the order of 1 TeV is much harder in circular machines for leptons due to significant synchrotron radiation losses. This calls for future linear lepton colliders such as CLIC [8] and ILC [9]. For example, the proposed ILC is a 30-50 km long electron-positron collider (Figure 1-2), more than 10 times longer than today’s largest linear accelerator, SLAC [10]. Its planned collision energy of 500 GeV with a possible upgrade to 1000 GeV puts it right above the existing blue line on the “Livingston” plot (Figure 1-1).

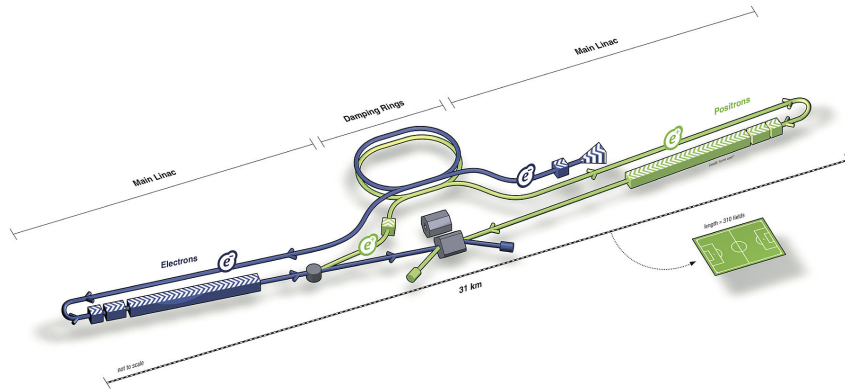


Figure 1-2: An overview graphic of the planned ILC based on the accelerator design of the Technical Design Report.

Other important type of particle accelerators, distinct from colliders, is so-called light sources. In light sources, the energy of the accelerated particles is converted to (typically X-ray) radiation, which is then used to study condensed matter physics, material science, biology, and medicine. The conversion is done in bending magnets of a synchrotron storage ring or an undulator of a free-electron laser [11].

Instead of luminosity used for colliders, the figure of merit used for light sources is brilliance. Brilliance is defined as the number of produced photons with a wavelength within 0.1% of the central wavelength, per unit time per unit solid angle per unit area. Various projects for light sources have been recently built or proposed, aiming for higher energy and brilliance of the produced X-rays [12, 13, 14, 15, 16]. Other methods of producing X-ray radiation in a more compact machine are also emerging [17].

All of these concepts for colliders and light sources rely on accelerators to provide energetic beams of charged particles. Traditionally, room-temperature radio-frequency or superconducting radio-frequency accelerators are used. Besides the two traditionally used types of accelerators, advanced far future concepts, such as plasma accelerators and dielectric accelerators, are being actively explored [18]. Their main advantage is the ability to provide a much higher accelerating gradient, defined as the accelerating voltage divided by the length of an accelerator. For example, an impressive accelerating gradient was recently demonstrated using laser-driven plasma acceleration, resulting in the energy gain of 4.2 GV over the length of mere 9 cm [19].

1.1 Energy-recovery-linacs

One especially interesting type of a particle accelerator utilized in both colliders and light sources is the energy recovery linear accelerator (energy-recover-linac or ERL). In the last decade ERLs have been proposed as driver accelerators for light sources [20, 21, 22, 16] and an electron-proton collider [23]. An ERL-based light source is an alternative to a more conventional design that relies on a synchrotron storage ring [24].

A schematic diagram of an ERL-based X-ray light source is shown in Figure 1-3. First, charged particles (typically electrons) are injected in radio-frequency (RF) or microwave cavities at the proper time for acceleration, which produces a high energy electron beam. This electron beam is then forced to oscillate in an arrangement of magnets of alternating orientation. As a consequence of this oscillation, X-rays are produced and the beam loses about 0.1% of its energy. Then, electrons are re-injected into the linac at the proper time for deceleration to recapture the remaining

99.9% of their energy. The recaptured energy is then available for the acceleration of subsequent bunches of electrons. Every bunch of electrons therefore first traverses the linac for acceleration, and after being used for X-ray production or in collisions with another beam traverses the same linac for deceleration.

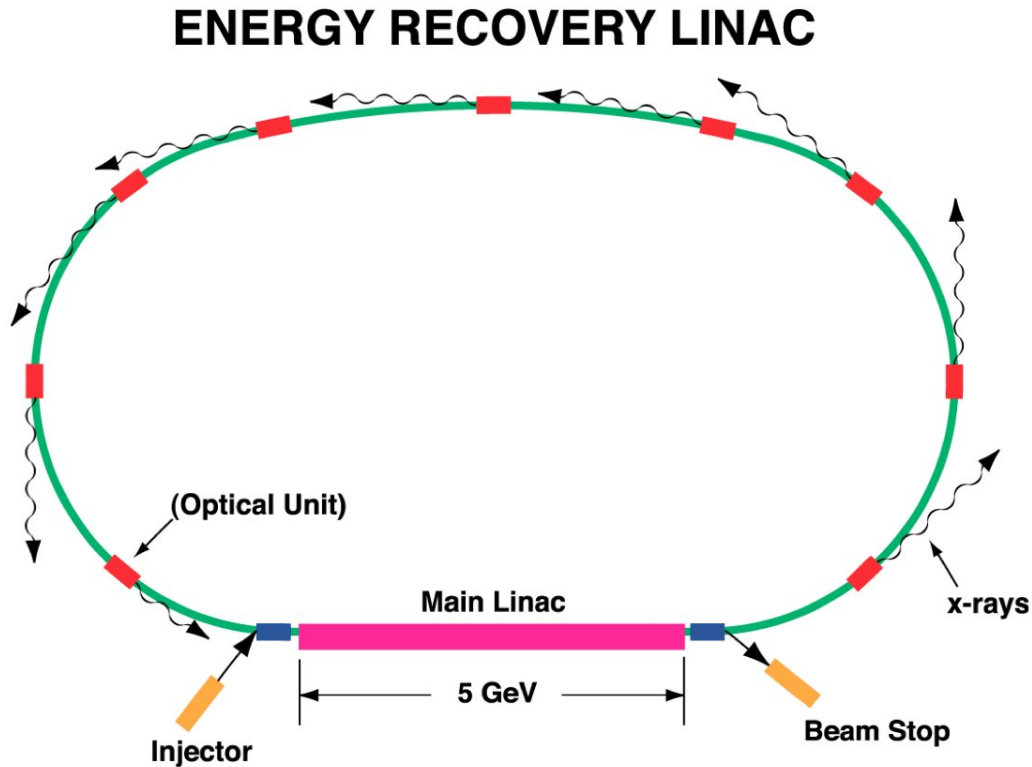


Figure 1-3: A diagram showing an ERL-based X-ray source.

One particularly important quantity characterizing the quality of a particle beam is called emittance. Emittance is the area that the beam occupies in the transverse or the longitudinal (with respect to the beam’s trajectory) phase space. In the transverse plane the phase space is defined in the dimensions of a transverse coordinate x and the corresponding angle of motion with respect to the beam’s trajectory x' . The emittance ϵ is proportional to the area of an ellipse enclosing the beam in the phase space $\epsilon = 1/\pi \int_{\text{ellipse}} dx dx'$ [25]. Emittance depends on a layout of an accelerator beamline and properties of all of its components (accelerating cavities, bending magnets, etc). Minimizing beam emittance is one of the major goals of accelerator design and is necessary for achieving high luminosity and brightness.

One of the motivations for using ERLs is their capability to provide the beam with an emittance much smaller than can be attained in a storage-ring based light source [24]. This can be explained by the fact that a conventional storage-ring in a synchrotron recycles bunches at high energy billions of times, compromising their beam quality, whereas in an ERL bunches are only accelerated once before being used for X-ray production or collisions.

Using energetic low-emittance bunches after they only pass an accelerator once would not be practical without energy recovery. Energy recovery is especially important for the projects mentioned above [21, 22, 16, 23] because they require electron beams with energies of multiple GeV and high continuous wave (CW) beam currents on the order of hundreds of mA. Indeed, this means that driver linacs would have to produce beam power as high as 1 GW, which is only feasible if the energy used to accelerate the beam is somehow recovered [24].

Besides low emittance, the high average beam current is also required for the projects [21, 22, 16, 23] to achieve the desired brilliance in the light sources or luminosity in the colliders. Even higher currents up to the ampere level are desirable for the future projects, as described in [26, 27]. While currents up to the ampere level are possible in ERLs with relatively low electron energies of multiple MeV [28, 29, 30], raising the beam current for a multi-GeV machine is highly challenging. This is due to the fact that multi-GeV ERLs have to be much longer, which makes the beam more vulnerable to instabilities and thus limits the achievable current. The main limitation comes from the beam break-up instability (BBU), which comes as a result of an interaction of the beam with parasitic electromagnetic modes in accelerating structures. This effect is caused primarily by the modes of dipole or quadrupole nature with frequencies above the accelerating RF frequency (hence they are called higher order modes or HOMs). Damping of HOMs is required to achieve high beam currents and subsequently high brilliances and luminosities.

1.2 Superconducting RF accelerators

In RF accelerators, electromagnetic waves at RF and microwave frequencies (from a fraction of 1 GHz to multiple GHz) are used to accelerate charged particles. The RF/microwave power is typically generated by a vacuum electronics device such as the klystron and fed into an array of accelerating cavities. Acceleration is done via beam interaction with the longitudinal component of the electric field of the electromagnetic wave. In room-temperature accelerators, cavities are normally made of copper due to its low resistivity. However, even copper's resistivity can be too high for certain accelerator applications and it is instead necessary to use superconducting materials.

Superconducting RF (SRF) cavities are traditionally made of high-purity niobium (Figure 1-4) and immersed into a bath of liquid helium to keep their temperature under the temperature of superconducting transition. The cavity, the cryogenic system, the tuners, and the RF power lines form a complete SRF accelerating module, shown schematically in Figure 1-5.

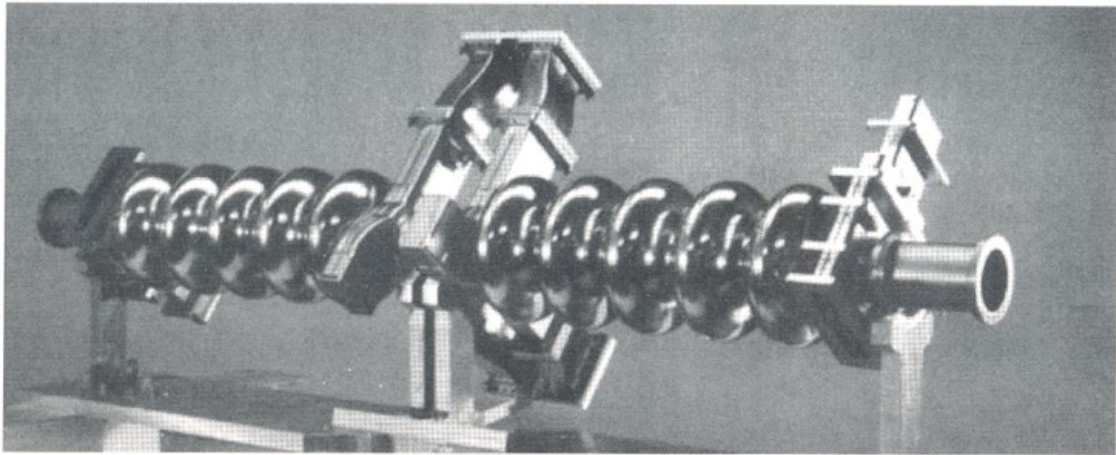


Figure 1-4: An example of superconducting RF cavities: two 1500 MHz 5-cell niobium cavities adopted by TJNAF (formerly CEBAF).

Superconducting cavities are especially helpful in accelerators that use continuous wave (CW) mode or a high duty factor, defined as the fraction of time when the RF is on [32]. For ERLs, the CW regime of operation is a natural choice. This can be explained by the fact that the energy of the electron bunches is periodically taken

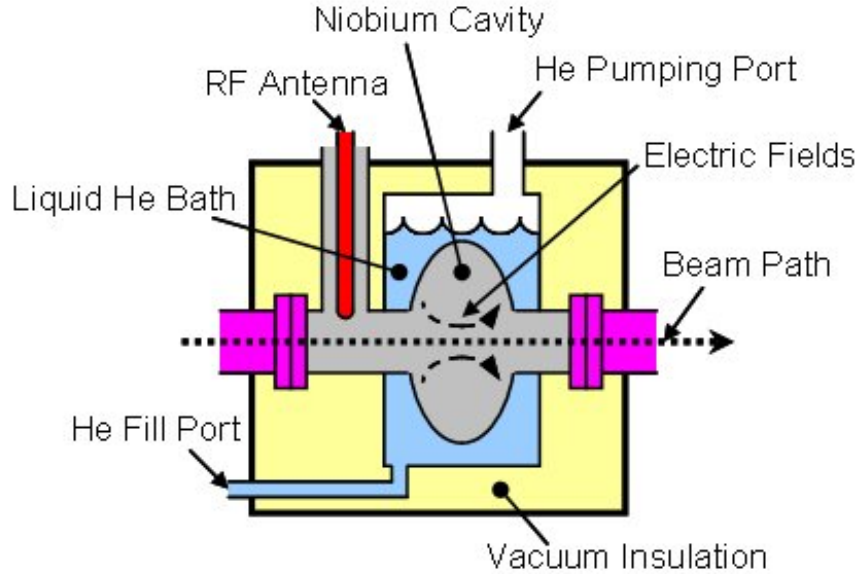


Figure 1-5: A simplified diagram of an SRF cavity in a helium bath with RF coupling and a passing particle beam. The picture is taken from [31].

from and then put back into the electromagnetic fields in accelerating cavities. If a copper structure is used in the CW regime, power dissipation in the walls could be unacceptable. On the other hand, RF/microwave surface resistance of a superconductor is typically five orders of magnitude lower than that of copper. Hence, all of the ERLs mentioned earlier [20, 21, 22, 16, 23] rely on SRF accelerating cavities.

Low surface resistance of superconducting cavities results in very high (although finite) Q-factors, typically $10^8 - 10^{11}$. The Q-factor for an electromagnetic mode is defined as the number of periods it takes for the mode's energy to decay by a factor of e (see Glossary for details). High Q-factor in SRF cavities gives a very significant reduction in the amount of AC power used per unit length of an accelerator. However, the tiny power dissipated in the walls of a superconducting cavity has to be taken out by a refrigerator system at liquid helium temperature. Therefore, one has to take into account the Carnot efficiency

$$\eta = \frac{T}{300 - T} = 0.014 \quad (1.1)$$

at $T = 4.2K$. This, together with the technical efficiency of refrigerator systems, gives

a factor of 200 of typical reduction of AC power due to the use of superconducting cavities [31], which is still very significant. In practice, it means that generated RF power is spent entirely on beam acceleration, which is not the case for room-temperature accelerators.

However, operation in the CW has drawbacks. Superconductors are fundamentally defined to expel all magnetic flux up to a critical field at which they lose their superconductivity. This critical field defines an upper bound on the surface magnetic field allowable in a superconducting accelerating cavity, which in turn limits the accelerating gradient. Over the past few decades, advances in cavity surface treatment and preparation significantly increased the maximum achievable gradient. However, for traditionally used niobium cavities an upper limit of 50 MV/m on the accelerating gradient is considered unavoidable.

New techniques are being developed today to increase the accelerating gradient and the Q-factor in superconducting cavities. Nitrogen doping of niobium walls has been proven to increase Q-factor by up to a factor of 4 [33], and has been adopted for the LCLS II accelerator [14]. Application of thin films to the niobium surface, although not fully developed yet, has the potential to increase the maximum achievable accelerating gradient and decrease surface losses [34, 35].

Besides the gradient limitation, superconducting cavities are costly. Although SRF cavities save expensive RF power, their cost can be very significant due to the complexity of SRF accelerating modules (Figure 1-5). Nevertheless, the advantages of superconducting RF accelerators tend to overcome the disadvantages for the overwhelming majority of today's big accelerator projects. They include ILC (possibly in Japan) [9], High-luminosity LHC in Switzerland [7], ESS in Sweden [36], European X-FEL in Germany [13], eRHIC [23], FRIB [37], MaRIE X-FEL [12], LCLS II [14], NSLS II [15], Advanced Photon Source Upgrade [16] (all in USA). Recently, SRF technology was also proposed for some industrial applications, where copper accelerators were traditionally used [38, 39, 40].

Consideration of beam break-up instability becomes especially important for SRF cavities. Once HOMs are excited in a superconducting cavity, they can oscillate for

a long time with very high Q-factors due to extremely low losses in the walls of the cavity. For this reason, all SRF cavities are equipped with HOM dampers such as antennas or ferrite absorbers located on the beampipe just outside of the main cavity space.

For example, the highly optimized TESLA cavity (which is a 1.3 GHz 9-cell SRF cavity) utilizes coaxial couplers located on the beam pipes on both sides of the cavity [41]. However, the TESLA cavity does not have HOM damping ability adequate for the high-current ERL projects [42]. Modifications of this design have been suggested to improve HOM damping by altering beam pipe and iris radii, somewhat sacrificing accelerating properties. Simulations confirmed the effectiveness of the new designs at providing the HOM damping required for 100 mA operation of the corresponding ERLs ([42, 43]).

Other examples are the 5-cell cavities developed at JLAB [26, 44, 45] for the frequencies of 748.5 MHz and 1.497 GHz. These designs are specifically optimized for HOM damping. Each design utilizes 6 waveguides on the beam pipe (3 on each side, arranged in a Y shape – so-called “waveguide endgroup”). Simulations [45] have demonstrated that a BBU threshold of 1A can be achieved for the 1.497 GHz cavity in a proposed ERL-based free electron laser.

Another design was recently proposed for a 1.4 GHz 9-cell cavity with waveguides attached directly to the accelerating cells, coupling through thin slots [27]. Simulations have shown its ability to provide a BBU current threshold as high as 1.5 A if used for the driver accelerator in the proposed Advanced Photon Source upgrade [16]. The design can be very promising if the required confinement of the fundamental mode is demonstrated. But good HOM suppression comes at a price of the increased surface fields.

PBG cavities are attractive candidates for particle accelerators and ERLs in particular because of their frequency selective property. This property can be used to confine the accelerating mode but not the HOMs, thus providing effective HOM damping.

1.3 Introduction to photonic band gap structures

The term “photonic band gap (PBG) structure”, or “photonic crystal”, refers to a structure that consists of regions with alternating dielectric constants, arranged in a periodic pattern. The pattern can be one-dimensional (1D), two-dimensional (2D), or three-dimensional (3D), as shown in Figure 1-6 [46]. The unique property of PBG structures is their frequency-selectivity. The effect of the spatially periodic structure on a propagating electromagnetic wave is analogous to the effect that semiconductors have on electrons. A PBG structure with characteristic spatial distance comparable to the wavelength of the propagating wave can either be transparent to the wave or act as a mirror, depending on the wave’s frequency. This behavior is explained by band gaps in dispersion diagrams of photonic crystals (see Chapter 2) - hence the name “photonic band gap structure”.

A one-dimensional PBG structure is analogous to the Bragg’s mirror used in optics to reflect incident light at certain frequencies. Examples of a three-dimensional PBG structure can be found in nature in the wings of butterflies [47] and in mineraloids like opal [48]. A natural periodic microstructure in the opal is responsible for its iridescent color (Figure 1-7).

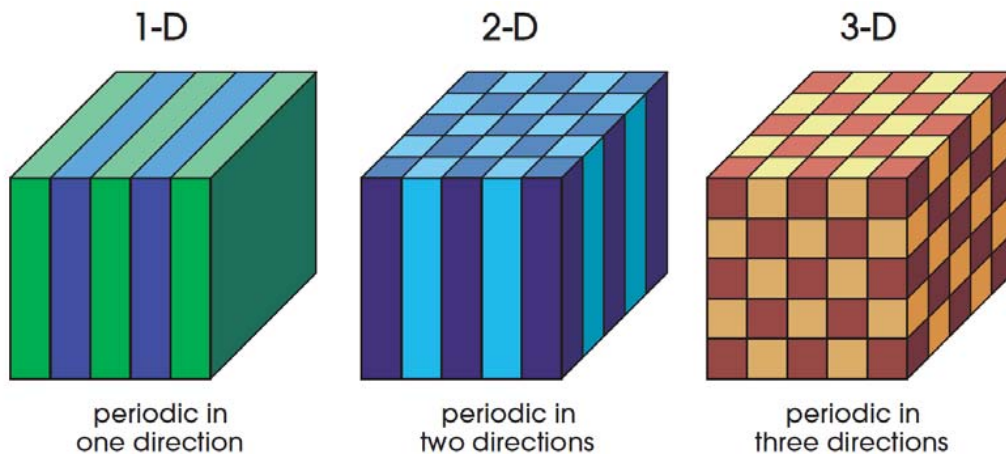


Figure 1-6: Examples of photonic crystals in one, two and three dimensions. Different colors represents different dielectric constants in space [3].

However, for us, the most interesting type of a PBG structure is the two-dimensional PBG structure. A 2D PBG structure is used in photonic crystal fibers (a special case



Figure 1-7: Opal’s natural photonic band gap structure is responsible for its iridescent light. The picture is taken from [49].

of an optical fiber) that find wide usage in fiber-optic communications (Figure 1-8). 2D PBG structures scaled up to resonate at RF/microwave frequencies are used in particle accelerators and vacuum devices [50, 51, 52, 53, 54, 55], including the one presented in this thesis.

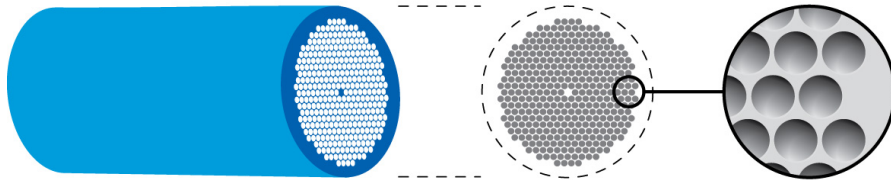


Figure 1-8: Internal structure of photonic crystal fibers is a 2D PBG array.

To form an accelerator cavity, a metal or dielectric 2D PBG structure is placed in between two walls. One of the PBG rods is removed from the 2D lattice of rods to form a hexagonally-shaped “cavity” (Figure 1-9). For accelerators, the PBG structure is used to confine the accelerating electromagnetic mode (the TM_{01} mode in the circular waveguide’s notation) in the formed “cavity”. At the same time, the frequency-selective property of the PBG structure is used to allow the parasitic modes with higher frequencies (HOMs) leak out in the radial direction to the periphery of the PBG structure [50]. In other words, HOM can be damped in a PBG structure with the right choice of parameters.

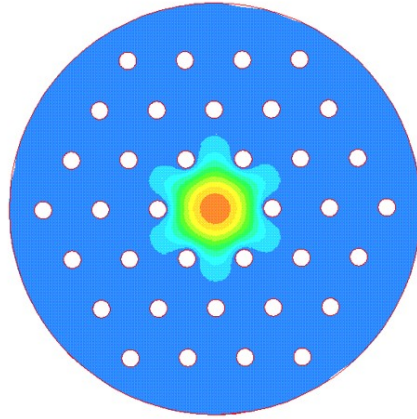


Figure 1-9: An example of an RF cavity formed by a removed rod in a photonic crystal. The color is showing the magnitude of the electric field. Metal parts are shown in white.

The first multi-cell PBG accelerating cavity was designed and tested at MIT in the early 2000-s [50, 56]. This was a traveling wave copper structure operating at room temperature at the frequency of 17.14 GHz. The structure confined the accelerating mode to successfully accelerate electrons at a gradient of 35 MV/m. After the proof-of-principle demonstration, an experiment and simulations were carried out to get some insight into HOM damping properties of the structure [57]. Copper PBG structures were later tested with high power at SLAC and MIT to investigate the breakdown phenomena at the frequencies of 11.424 GHz and 17.14 GHz and accelerating gradients comparable to conventional disk-loaded cavities were achieved [58, 59, 52]. Recently, it has been experimentally shown that a copper PBG module at the frequency of 11.7 GHz has a reduced level of HOMs [60].

Other versions of room-temperature PBG structures were later investigated. A dielectric PBG structure was designed and optimized for stronger HOM damping at the University of Colorado [53]. A hybrid (metal and dielectric) PBG module operating at the frequency of 17.14 GHz was recently designed and tested at high power at MIT [51].

The first superconducting PBG prototype resonator, operating at the frequency of 11 GHz, was designed and fabricated about two decades ago even before the copper

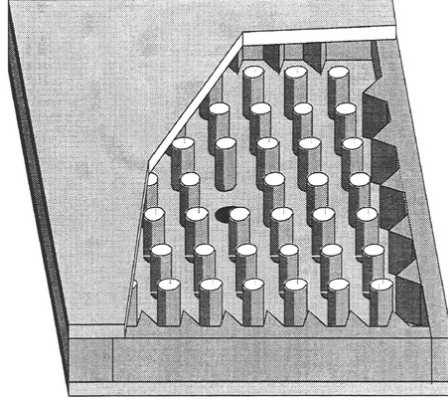


Figure 1-10: A schematic diagram of the first superconducting PBG cavity [61]. The beam passes in the up-down direction through the holes in the walls. Microwave absorber is placed around the periphery of the structure.

MIT structure [61]. The cavity is schematically shown in Figure 1-10. The resonator's unloaded Q -factor was shown to be at least 1.2×10^6 at the temperature of 4.8 K. The measurement technique did not allow the authors of [61] to show that the Q -factor was greater than 1.2×10^6 . This value is not sufficient for a superconducting cavity, where a typical Q -factor due to the losses in the walls is between 10^8 and 10^{11} and further tests were needed. However, this research was not continued at the time.

Later, advances in PBG technology for room-temperature accelerators mentioned above revived interest in superconducting PBG cavities. A superconducting PBG resonator design was proposed in [62]. A prototype, operating at the frequency of 16 GHz, was tested at cryogenic temperatures and showed the unloaded $Q = 1.2 \times 10^5$ limited by radiation losses. Recently, several single SRF PBG cells operating at 2.1 GHz were fabricated and tested at Los Alamos National Laboratory (LANL) [63, 64]. A promising accelerating gradient of 18 MV/m and an unloaded quality factor $Q = 4 \times 10^9$ were achieved.

All of the superconducting PBG structures tested in the past were single-cell versions of an accelerating cavity, designed and built specifically for proof-of-principle experiments. For practical use, it is best to employ multi-cell SRF cavities such as the DESY's TESLA 9-cell cavity [65], the Cornell's 7-cell cavity [66], the JLAB's 5-cell cavity [44], and many others. A motivation for employing a multi-cell design

is the increased “packing factor”, meaning that the ratio of the length where acceleration happens to the total length of a cryomodule is higher. Therefore, the logical continuation of the research of PBG cavities for SRF accelerators is to build a multi-cell cavity. This thesis presents the first-ever multi-cell SRF cavity with a PBG cell, shown in Figure 1-11.



Figure 1-11: The fabricated niobium 5-cell accelerating cavity with a coupler PBG cell in the middle. The cavity resonates at the RF frequency of 2.1 GHz.

1.4 Summary of thesis

SRF cavities with PBG cells can be useful for particle accelerators that require strong HOM damping. An example of such accelerators is future ERLs that push toward higher beam current and lower beam emittance. These ERLs are useful for both light sources and lepton colliders, with the end goals including studying high-energy physics, condensed matter physics, material science, biology, and medicine.

A detailed discussion of the results of this work is presented in Chapter 7 of this thesis. Here we briefly summarize the results and describe the contents of the Chapters.

The first-ever multi-cell superconducting PBG cavity was designed and optimized to achieve a more effective HOM damping than is achieved in conventional multi-cell SRF cavities employing elliptical cells. The HOM spectrum in the designed cavity was carefully analyzed using eigenmode and wakefield simulations with good agreement between the two methods. In addition to the effective HOM damping, the cavity design reduces the length of accelerator required to get to a given energy. The design and simulations are described in Chapter 3 of the thesis.

Novel fabrication and tuning mechanisms were successfully tested on a copper prototype and later used for the niobium cavity. The accelerating gradient profile in the tuned cavity matched the desired profile to a 5% accuracy. The process of fabrication and tuning is described in Chapter 4.

HOM damping properties were experimentally measured in the fabricated cavity at room temperature. The measurements generally agreed with the simulations with the exception of two modes that were damped even stronger than was predicted. Damping techniques using RF loads and a sliding short were studied. The measurements are summarized in Chapter 5.

The fabricated cavity was tested at cryogenic temperatures. The Q-factor of the accelerating mode agreed with the expectations. No hard barriers in the accelerating gradient were observed during the test, which indicated the absence of fundamental limits to the cavity's operation for an accelerating gradient of at least a few MV/m. The cryogenic tests are described in Chapter 6.

The bibliography and a list of supplemental materials are written in the end of Thesis.

Chapter 2

Theory

In this Chapter, we discuss various aspects of the theory of RF cavities. The Chapter is divided into 3 parts: the theory of wakefields and higher order modes (HOMs), the theory of PBG structures, and the theory of operation of SRF cavities. These theories form the background for the further Chapters of this thesis. In particular, the theory of PBG cavities is used in the design of the 5-cell cavity to justify the choice of the parameter a/b of the PBG lattice (Chapter 3). The theory of wakefields and HOMs is used in analyzing the HOM damping properties of the cavity (Chapter 3). The theory of operation of SRF cavities is used in the experimental part of this thesis (Chapter 6).

2.1 Wakefields and higher order modes

Wakefields are defined as electromagnetic fields excited in an RF cavity by a passing particle beam. An example of the profile of the electric field excited in an RF cavity following a pass of an electron beam is shown in Figure 2-1 [67].

Wakefields can be expressed as a sum of electromagnetic modes of the cavity. In addition to the accelerating mode, this sum generally includes higher order modes (HOMs) – unwanted parasitic modes present in accelerating cavities. Accelerating cavities are designed in a way to ensure that only the accelerating mode is exactly at resonance with the beam, meaning that the phase velocity of the mode $v_{ph} = \omega/k$

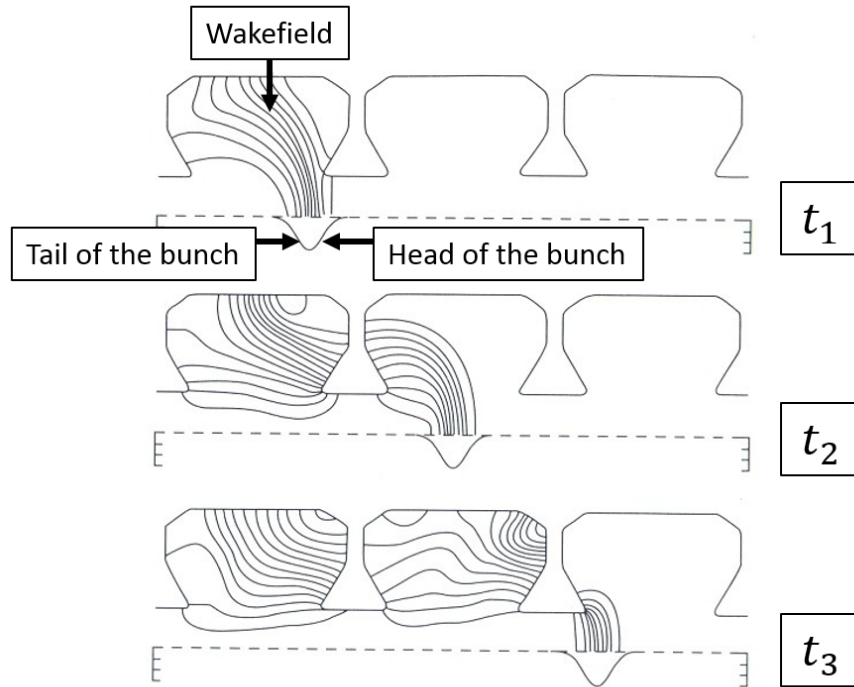


Figure 2-1: Numerically calculated electric wakefields generated by a passing bunch in a PETRA cavity at DESY [68]. The beam moves along the dashed line on an axis of cylindrical symmetry. The solid lines connect the vectors of the electric field.

is equal to the velocity of the beam. Nevertheless, some near-resonant excitation of HOM wakefields also takes place. Excited HOMs interact with the beam and can have a very significant effect on the quality of the particle beam, limiting the maximum beam current achievable in the accelerator.

According to their spatial range, wakefields are classified as short-range and long-range wakefields. Short-range wakefields are induced by the head of a single bunch of particles (the front part of the bunch, as shown in Figure 2-1) and affect the trailing particles in the same bunch, causing energy spread for the following on-axis trailing particles, and, additionally, transverse deflection for the following off-axis particles. Long-range wakefields act on scales comparable to or greater than the wavelength of the accelerating mode. The most serious effect of the long-range wakefields is caused by transverse deflecting modes that induce time-varying transverse deflections in trailing bunches [67].

One way to quantify long-range wakefields is to use longitudinal wake potential \mathbf{w}_{\parallel} and transverse wake potential \mathbf{w}_{\perp} [67, 69] for point-bunches (much smaller than the wavelength):

$$\mathbf{w}_{\parallel}(\mathbf{r}, \mathbf{r}_1, s) = -\frac{1}{qq_1} \int_0^L dz \mathbf{F}_{\parallel t=(z+s)/c}, \quad (2.1)$$

$$\mathbf{w}_{\perp}(\mathbf{r}, \mathbf{r}_1, s) = \frac{1}{qq_1} \int_0^L dz \mathbf{F}_{\perp t=(z+s)/c}, \quad (2.2)$$

where \mathbf{r} is the transverse displacement of the source charge q_1 , \mathbf{r}_1 is the transverse displacement of the test charge q , s is the distance between the charges, $\widetilde{F}_{\perp n}$ is a complex phasor of the transverse electromagnetic force acting on the test charge, and L is the length of the structure. A graphical representation is shown in Figure 2-2. For ultrarelativistic (relativistic $\gamma \gg 1$) bunches, s is the product of the speed of light c , and the time-separation between the bunches: $s = ct$.

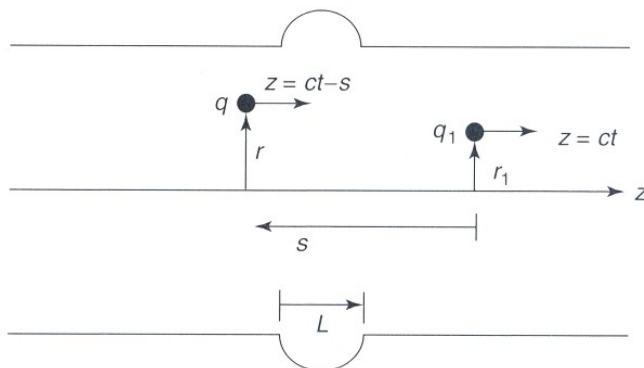


Figure 2-2: A graphical representation of the quantities used in Equations 2.1 and 2.2 (from [67]). An ultrarelativistic source charge q_1 passes through a geometric perturbation (RF cavity). A following test charge q can be affected by the wakefield excited by the source charge.

Wake potential includes contributions from all the HOMs with different frequencies and Q-factors. In real structures modes have finite Q-factors and the wake potential can be represented as a sum of decaying sinusoidal functions of s approaching zero as s approaches infinity. If a subsequent bunch is separated by some distance s_* such that $\mathbf{w}(\mathbf{r}, \mathbf{r}_1, s_*) = 0$, the bunch is not affected by the wakefield at all. However, zeros of the wake potential are not equidistant so minimizing wake potential at one

particular distance is not beneficial to an acceleration of trains of bunches. Hence, the only way to minimize the negative effect of the long-range wakefields is to make wake potential decay faster, in other words, to provide effective HOM damping.

To analyze the frequency content of wakefields, we use the Fourier spectrum of wake potential, called wake impedance Z . Longitudinal and transverse wake impedances are defined in [67] as

$$\mathbf{Z}_{\parallel}(\mathbf{r}, \mathbf{r}_1, \omega) = \frac{1}{c} \int_{-\infty}^{\infty} \mathbf{w}_{\parallel}(\mathbf{r}, \mathbf{r}_1, s) e^{-i\omega s/c} ds, \quad (2.3)$$

$$\mathbf{Z}_{\perp}(\mathbf{r}, \mathbf{r}_1, \omega) = \frac{1}{ic} \int_{-\infty}^{\infty} \mathbf{w}_{\perp}(\mathbf{r}, \mathbf{r}_1, s) e^{-i\omega s/c} ds. \quad (2.4)$$

The wake impedance computed for a particular cavity carries information about frequencies and impedances of the HOMs comprising the wakefield. For example, the most dangerous dipole and quadrupole HOMs appear as peaks in transverse wake impedance. An example of a possible wake impedance profile is shown in Figure 2-3.

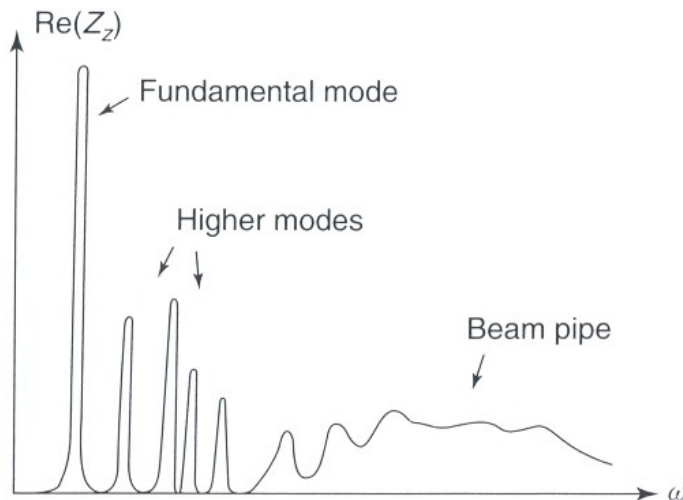


Figure 2-3: Typical frequency spectrum of the real part of an accelerator cavity wake impedance from [67].

For a given geometry, wake potential and wake impedance can be computed numerically using a wakefield solver, such as CST Particle Studio [70]. An alternative

way to quantitatively describe the effect of wakefield HOMs on particle bunches is to use the effective induced voltages. Unlike wake impedance, effective voltages can be computed using an eigenmode solver such as Ansys HFSS [71]. An eigenmode simulation is typically a simpler computational problem, however, eigenmode simulations are only useful if the dangerous HOMs have been identified beforehand.

Effective voltages $V_{\parallel n}$ and $V_{\perp n}$ describe how the n -th HOM affects the test charge q . $V_{\parallel n}$ and $V_{\perp n}$ are defined in [31] as

$$V_{\parallel n} = \frac{1}{q} \int_0^L \widetilde{F}_{\parallel n} e^{i\omega_n z/c} dz, \quad (2.5)$$

$$V_{\perp n} = \frac{1}{q} \int_0^L \widetilde{F}_{\perp n} e^{i\omega_n z/c} dz. \quad (2.6)$$

Here $\widetilde{F}_{\parallel n}$ and $\widetilde{F}_{\perp n}$ are complex phasors of the longitudinal and the transverse electromagnetic forces acting on the test charge q , c is the speed of light, and $\omega_n = 2\pi f_n$ is the angular frequency of the n -th HOM. We will demonstrate in the next section that deflecting voltage for a dipole mode is proportional to the integrated area under the corresponding peak of the transverse wake impedance.

2.1.1 Relationship between wake impedance and deflecting voltages

In this section, we find the relationship between the effective deflecting voltages of the dipole higher order modes (HOMs) defined in Equation (2.6) and the sizes of the corresponding peaks in the transverse wake impedance.

Transverse wake potential from a relativistic point charge and related transverse wake impedance are defined in Equations (2.2) and (2.4). In the following derivation, we only consider the special case $\mathbf{r} = \mathbf{r}_1$ used in the Wakefield solver of CST Particle Studio. We also consider a component of the wake potential along a particular axis X and set $\mathbf{r} = \mathbf{r}_1 = x\hat{x}$, however, the same applies to the component along the orthogonal axis Y . Our goal is to use wakefield impedance to calculate the effective deflecting voltage V_{xn} defined in Equation (2.6).

The expressions for wake potential (2.2) and the deflecting voltage (2.6) for the case $\mathbf{r} = \mathbf{r}_1 = x\hat{x}$ become

$$w_x(x, s) = -\frac{1}{qq_1} \int_0^L dz F_{xt=(z+s)/c}, \quad (2.7)$$

$$V_{xn} = \frac{1}{q} \int_0^L \widetilde{F}_{xn} e^{i\omega_n z/c} dz, \quad (2.8)$$

To relate Equation (2.7) to Equation (2.8), we write the electromagnetic force in the phasor notation:

$$F_{xn}(x, z, t) = \text{Re} \left(\widetilde{F}_{xn}(x, z) e^{i\omega_n t} \right) e^{-\frac{\omega_n t}{2Q_n}}, \quad (2.9)$$

where Q_n is the total quality factor of the n -th HOM. By plugging Equation (2.9) in the Equation (2.7) and using Equation (2.8), we get

$$w_x(x, s) = \frac{1}{q_1} \sum_n \text{Re} \left(V_{xn} e^{i\omega_n s/c} \right) e^{-\frac{\omega_n s}{2Q_n c}}. \quad (2.10)$$

Subsequently, the expression for the wake impedance (2.4) becomes

$$\begin{aligned} Z_x(x, \omega > 0) &= \frac{1}{ic} \int_{-\infty}^{\infty} w_x(x, s) e^{-i\omega s/c} ds = \\ &= \sum_n \frac{V_{xn}}{2iq_1} \frac{1}{\frac{\omega_n}{2Q_n} - i(\omega_n - \omega)}, \end{aligned} \quad (2.11)$$

where the wake impedance is written as a sum of individual peaks. The integration steps are omitted. The absolute value of the wake impedance in the vicinity of the n -th peak becomes:

$$|Z_{xn}| = \frac{V_{xn}}{2q_1} \frac{1}{\sqrt{(\omega_n - \omega)^2 + \frac{\omega_n^2}{4Q_n^2}}}, \quad (2.12)$$

which is the square-root of the Lorentzian shape.

Given Equation (2.12), we find the half-max width of the n -th peak $\Delta f_n = \sqrt{3}f_n/Q_n$. By substituting Q_n with Δf_n we can finally express the effective deflecting voltage through the height of the peak $|Z_{xn}^{peak}| = |Z_{xn}|_{f=f_n}$ and the width of

the peak Δf_n :

$$|V_{x_n}| = \frac{2\pi}{\sqrt{3}} q_1 |Z_{x_n}^{peak}| \Delta f. \quad (2.13)$$

Thus, the two ways to quantify wakefield HOMs are closely connected. We can use the relation in Equation (2.13) to compute the deflecting voltages for the dipole HOMs by only using a wakefield simulation. Then, eigenmode simulations can be used to verify the results.

2.1.2 Higher order mode damping in energy-recovery-linacs

In Chapter 1 we mentioned that the beam break-up (BBU) instability caused by higher order modes (HOMs) is a major limiting factor for achieving high beam currents in energy-recovery-linacs (ERLs). For ERLs with one recirculating turn, an estimate for the BBU threshold current I_{th} was derived for the n -th HOM in [72]:

$$I_{th} = -\frac{2c^2}{e\left(\frac{R}{Q}\right)_n Q_n \omega_n T_{12}^* \sin \omega_n t_r}, \quad (2.14)$$

where the matrix T describes how the beam's transverse momentum translates into the transverse displacement after one turn:

$$T_{12}^* = T_{12} \cos^2 \theta_n + (T_{14} + T_{32}) \sin \theta_n \cos \theta_n + T_{34} \sin^2 \theta_n. \quad (2.15)$$

Here c is the speed of light, e is the elementary charge, $(R/Q)_n$ is the shunt impedance of the n -th HOM (in Ohms), Q_n is its total quality factor, $\omega_n = 2\pi f_n$ is its angular frequency, θ_n is the polarization angle from the x direction, t_r is the bunch return time.

It follows from the Equation (2.14) that the current limit I_{th} due to the n -th HOM is inversely proportional to the quantity $(R/Q)_n Q_n f_n$. Thus, the modes with higher shunt impedance $(R/Q)_n$ are considered more dangerous. In order to keep the quantity $(R/Q)_n Q_n f_n$ small and therefore maximize the current, Q_n for such modes must be reduced by means of external couplers or ferrite absorbers, usually located in the beam pipe sections of the cavities [32]. PBG structures are an alternative solution

to the problem of HOM damping.

2.2 Photonic band gap structures

In this Chapter, we explain the frequency-selective properties of photonic band gap structures introduced in Chapter 1. The frequency-selective nature of PBG structures is related to their spatial periodicity. An example of a periodic structure is an array of rods arranged in a regular tiling, meaning that the same polygon must be used to cover the entire 2D plane. This limits the rods to be placed at the vertices of either equilateral triangles or squares.

With one of the rods removed, the resulting cavity would have the 4-fold rotational symmetry in the case of the square lattice and the 6-fold rotational symmetry in the case of the triangular lattice. A higher degree of symmetry is desired to avoid distortions to the beam profile in accelerating cavities operating in the TM_{01} mode, which is the lowest-frequency solution to Maxwell's equations in the cylindrical cavity. The 6-fold symmetry resembles the full rotational symmetry very closely in the central part of the formed cavity (Figure 1-9). We, therefore, conclude that the triangular lattice is better suited for accelerating cavities working in the lowest TM_{01} mode.

We therefore only discuss the theory of the triangular PBG lattice, shown in Figure 2-4. The fundamental unit cell of the triangular 2D PBG lattice is shown in Figure 2-4 with the dashed black lines. The triangular lattice has two parameters: the radius of the rods a and the distance between the centers of neighboring rods b . Scaling of the structure without changing the ratio a/b only changes the frequency but does not change the field patterns of the electromagnetic modes. We can, therefore, reduce the number of parameters to one – the ratio of a/b , by using the normalized value of frequency $\omega b/c$. Here c is the speed of light.

Solutions to Maxwell's equation for structures with the translational symmetry in the direction of the rods can be decomposed into two independent classes of modes: the transverse electric (TE) modes and the transverse magnetic (TM) modes. In the TE mode, the electric field is perpendicular to the z -axis, while in the TM mode the

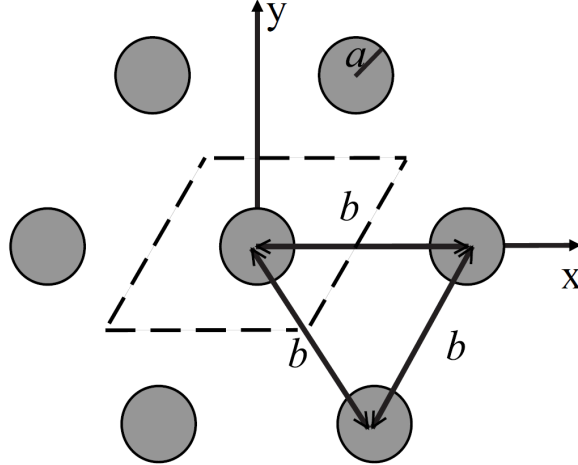


Figure 2-4: Fundamental unit cell is shown in a dashed line for the case of the 2D triangular lattice. The picture is taken from [73].

magnetic field is perpendicular to the z -axis. All of the components of electric and magnetic fields can be expressed as functions of the non-zero z -component of the field (either electric or magnetic), which we will call $\psi(x, y)$.

Another consequence of the translational symmetry in the z -direction is the fact that the longitudinal wave number k_z is conserved for any given solution, and can be viewed as a parameter. Maxwell's equations can, therefore, be reduced to the Helmholtz equation

$$\nabla_{\perp}^2 \psi(x, y) = \left(k_z^2 - \frac{\omega^2}{c^2} \right) \psi(x, y), \quad (2.16)$$

together with the appropriate boundary condition dictated by the geometry of the structure. In this thesis, we only focus on PBG structures that consist of metal rods, and the boundary condition on the surface of the rods is approximated by a perfect conductor (zero longitudinal component of the electric field on the surface).

As can be seen from Equation (2.16), the longitudinal component of the wave number k_z is "decoupled" from the problem, as it only produces a shift in frequency. In the following derivations, we assume the case $k_z = 0$ without a loss of generality. In the case of a non-zero k_z , frequencies of the obtained dispersion relationships $\omega(k_{\perp})$ should be shifted upwards by the appropriate amount.

We can now use the periodicity in the $x - y$ plane, and express a solution as a

wave propagating with a wave number $\vec{k}_\perp = k_x \hat{e}_x + k_y \hat{e}_y$ in the $x - y$ plane. The solution ψ satisfies the Bloch's equation:

$$\psi(\vec{r} + \vec{T}) = e^{i\vec{k}_\perp \vec{T}} \psi(\vec{r}), \quad (2.17)$$

where $\vec{r} = x\hat{e}_x + y\hat{e}_y$ is the vector in the $X - Y$ plane, and \vec{T} is any vector connecting two vertices of the PBG lattice. Such solution is called a Bloch wave.

Equation (2.16) can be numerically solved in the unit cell for a wave satisfying the condition in Equation (2.17). Thus dispersion relationships $\omega(k_\perp)$ for different solutions (bands) can be obtained. It is only necessary to consider k_\perp -values inside the so-called irreducible Brillouin zone. The irreducible Brillouin zone for the triangular lattice is a triangle in the k -space with vertices in the points Γ ($\vec{k}_\perp = 0$), X ($\vec{k}_\perp = \frac{2\pi}{\sqrt{3}b} \hat{e}_y$), and J ($\vec{k}_\perp = \frac{2\pi}{\sqrt{3}b} (\hat{e}_x + \hat{e}_y/\sqrt{3})$) [46]. To plot the dispersion relationships, we vary k_\perp along the border of the irreducible Brillouin zone, through the points Γ , X , J , and back to Γ . An example of a numerical solution for a particular choice of the ratio $a/b = 0.15$ is shown in Figure 2-5.

As can be seen in Figure 2-5, a gap in the frequencies of TM bands (a photonic band gap) is formed at the frequency range shown in yellow. TM Bloch waves at frequencies in the band gap cannot propagate in the infinite PBG structure. Such dispersion diagrams can be plotted for various ratios of a/b and the frequency ranges of the bandgaps can be viewed as functions of a/b . The results of numerical simulations of the band gaps for the TE and the TM polarizations for a/b in the range from 0 to 0.5 are shown in Figure 2-6 [73].

For a design of a particular RF/microwave PBG cavity the parameter a/b needs to be chosen based on Figure 2-6 so that the frequency of the operating mode is inside of the band gap (the “no propagation” region in Figure), but the frequencies of the unwanted modes are outside of the band gap.

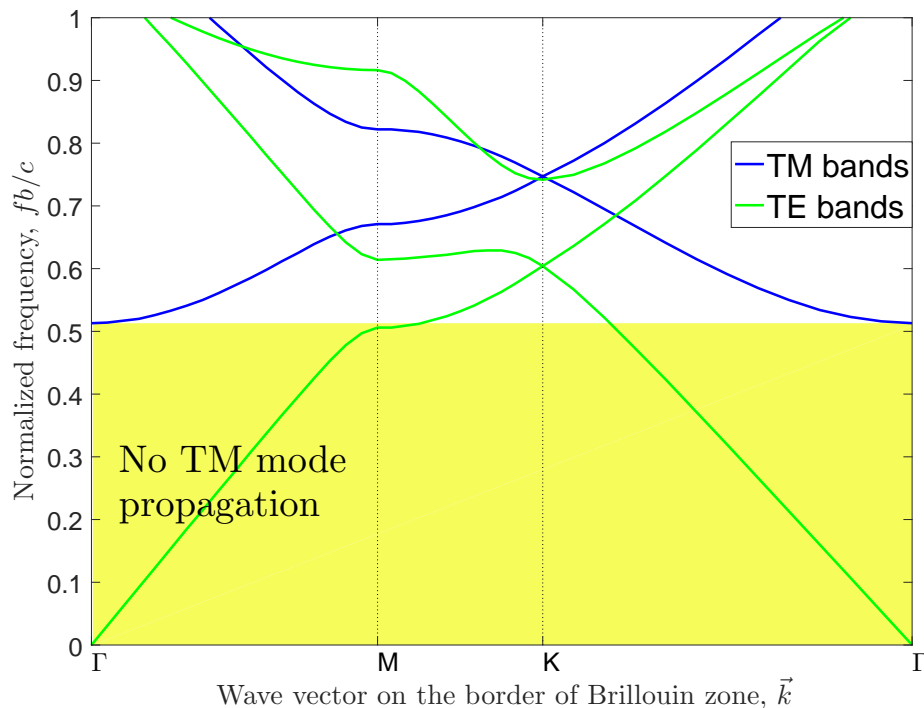


Figure 2-5: Dispersion relation including several TM and TE modes of the lowest normalized frequency of the triangular PBG lattice with $a/b = 0.15$. Yellow shadow indicates the band gap.

2.3 RF superconductivity

A complete description of the theory of superconductivity is beyond the scope of this thesis. However, we present brief explanations for a few key concepts used in this manuscript. In this section we will discuss the RF superconducting surface resistance R_s , and also the maximum electromagnetic fields achievable in a superconducting cavity.

Superconductivity, discovered in 1911 by Kammerlingh-Onnes [75], is a phenomenon where below a certain temperature, called the critical temperature T_c , some materials show a sudden drop of the DC electrical resistance to zero. This effect is found in metals such as lead and niobium, various alloys, and ceramics.

Forty years after the discovery of superconductivity by Kammerlingh-Onnes, the first theory of superconductivity was presented by Bardeen, Cooper, and Schrieffer, referred to as BCS theory [76]. The theory relies on concepts of quantum mechanics

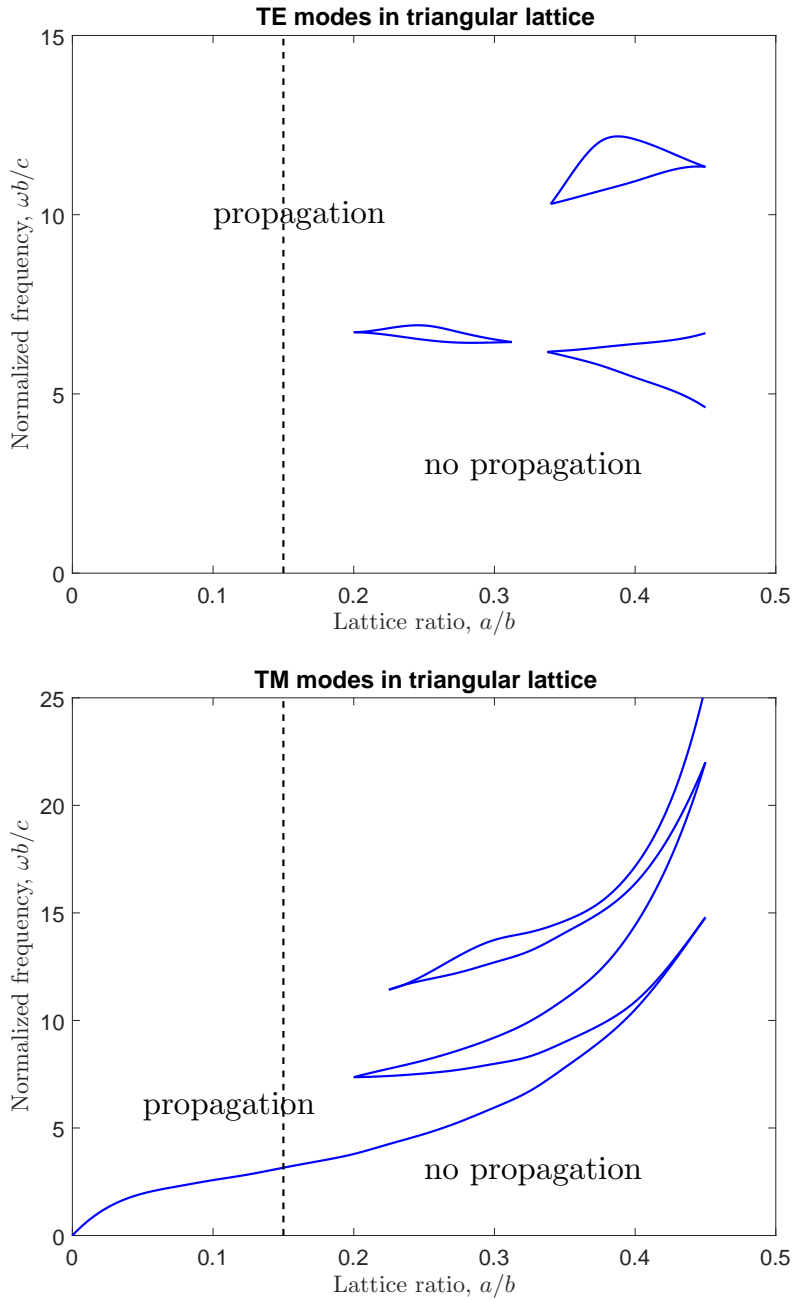


Figure 2-6: Global band gap map for the TE modes (top) and the TM modes (bottom) for the triangular lattice. The plotted map is based on numerical computations by E. Smirnova [73]. A choice of parameter a/b imposes a vertical dashed line that slices through the regions of propagation and no propagation (the case $a/b = 0.15$ is shown).

to describe the effect of superconductivity, and it has been very successful in providing a microscopic explanation for many aspects of superconductivity. According

to the theory, free electrons in a superconducting material experience a small net attraction due to the inertia of positive ions of the lattice of material. This attraction is analogous to the electromagnetic interaction between moving charges, except that the interaction is done not through photons, but through phonons - distortions of the ion lattice. This mechanism is visualized in Figure 2-7 from [31].

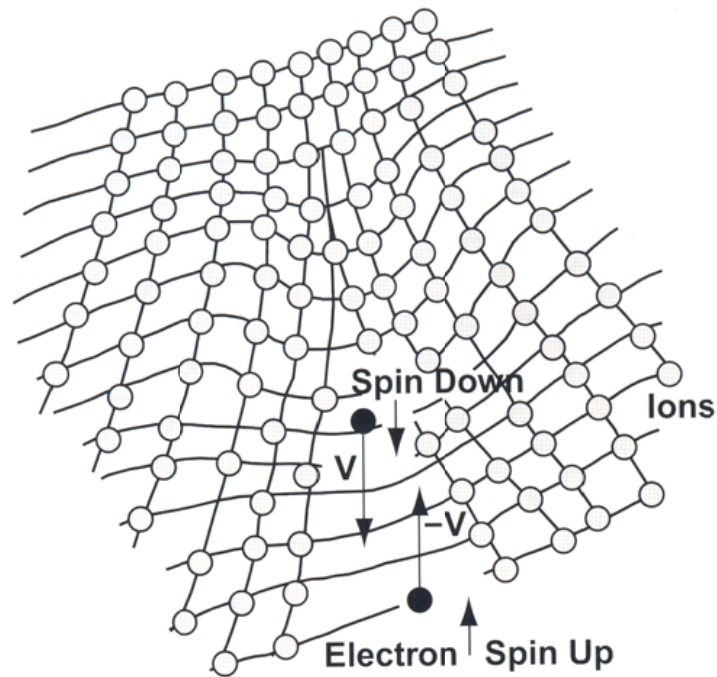


Figure 2-7: A simplified view of the electron-phonon interaction [31]. An electron moving through the lattice distorts the lattice. The deformed lattice acts on a second electron moving in the opposite direction through the positive charge accumulation.

The presence of the attractive potential makes quantum states redistributed, such that an energy gap of size $\Delta(T)$ is created around the Fermi energy ϵ_F . This makes it energetically favorable for electrons to be removed from energy levels slightly below the Fermi energy ϵ_F , and form pairs with electrons with energies higher than ϵ_F . These electron pairs are called Cooper pairs, and can be regarded as new particles with twice the charge and twice the mass of an electron. The spatial extent of a Cooper pair is about 39 nm in niobium and about 83 nm in lead.

2.3.1 RF surface resistance

A two-fluid model can be used to understand the zero DC resistance and very low RF resistance of a superconductor. One fluid is a “superfluid” of paired electrons and the other is a normal fluid of “free” electrons. Both fluids can carry current in parallel. However, since the “supercurrent” flows with zero resistance, it can carry the entire current. This is indeed what happens if a DC electric field is applied to a superconductor - paired electrons effectively “screen” the field from unpaired electrons.

However, the situation is different for RF currents. Cooper pairs do not screen the applied field perfectly because of their inertia. As a result, some current is carried by unpaired electrons. Power, dissipated in the walls, is proportional to the product of electric field E_{int} and current density j_{int} , and is related to the magnetic field H and the density of unpaired electrons n_{normal} :

$$P_{diss} = \frac{1}{2}R_s H^2 \propto E_{int} j_{int} \propto n_{normal} f^2 H^2. \quad (2.18)$$

At temperatures below about half of the superconducting transition temperature T_c , a fraction of unpaired electrons is approximately given by the Boltzmann factor [31]:

$$n_{normal} \propto \exp\left(-\frac{\Delta(0)}{k_B T}\right), \quad (2.19)$$

where k_B is the Boltzmann’s constant and $\Delta(0)$ is size of an energy gap around at the absolute zero temperature.

Using Equations 2.19 and 2.18, we can carry out the following simplified expression for surface resistance, valid for $T < T_c/2$:

$$R_s = A_s f^2 \exp\left(-\frac{\Delta(0)}{k_B T}\right), \quad (2.20)$$

where A_s is some proportionality constant.

A more complicated analysis involves material parameters such as penetration depth, Cooper pair coherence length, Fermi velocity, and the mean free path. Sophisticated calculations have been found to confirm the simplified form of the tem-

perature dependence of surface resistance of niobium for $T < T_c/2$, described in Equation (2.20). A good fit for surface resistance is

$$R_{BCS} = 2 \times 10^{-4} \frac{1}{T} \left(\frac{f}{1.5} \right)^2 \exp \left(-\frac{17.67}{T} \right), \quad (2.21)$$

where f is the frequency in GHz and T is the temperature in K [77].

From the above expressions, one may expect that surface resistance can be made arbitrarily small by going to lower a temperature. However, it has been found that below a certain temperature the experimentally observed surface resistance is higher than the BCS prediction (Figure 2-8). It is explained by a residual resistance R_0 that is independent of temperature. The total resistance can, therefore, be expressed as a sum of the two contributions:

$$R_s = R_{BCS}(T) + R_0 \quad (2.22)$$

Mechanism of residual loss are complex and depend on the surface preparation of a superconductor and the manner in which it was cooled to a superconducting temperature. In particular, cooling, if not done correctly, can result in ambient magnetic field flux being “trapped” in the superconductor. An estimate for residual surface resistance due to trapped magnetic flux can be found in [78]. Typical values for R_0 are tens of $n\Omega$, with the record values near $1n\Omega$, as stated in [31].

2.3.2 Surface fields

Theoretical limit to surface magnetic field

When an external DC magnetic field is turned on, supercurrents flow in the penetration depth to cancel out the field in the interior of the superconductor. Expulsion of the external magnetic field in a superconductor is called the Meissner effect. However, there is a theoretical limit H_c to the maximum external DC magnetic field that can be completely expelled. This limit is called the thermodynamic critical field. The

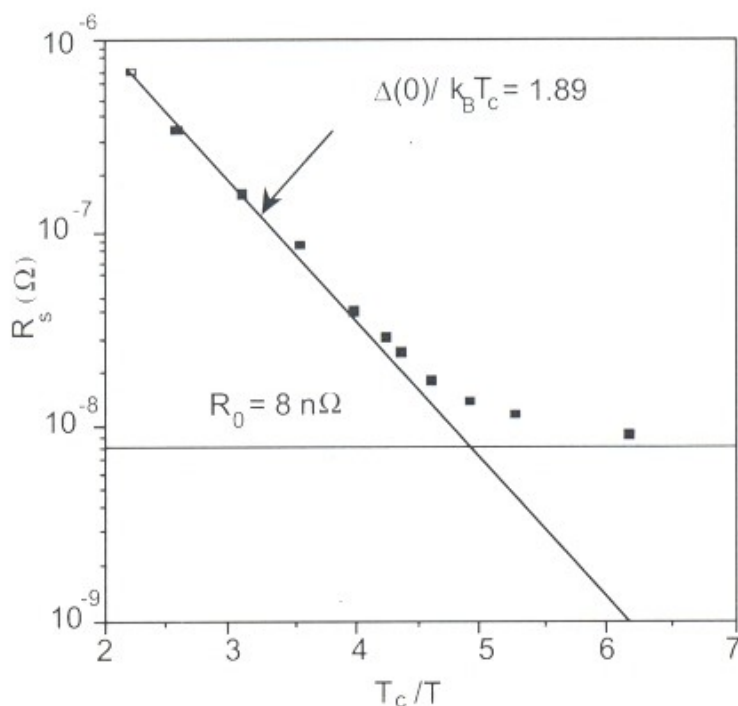


Figure 2-8: Surface resistance measured for a 1.5 GHz single-cell niobium cavity plotted as a function of inverse reduced temperature T_c/T [31]. At low temperatures surface resistance is dominated by the residual loss.

BCS theory predicts the following thermodynamic critical field [31]:

$$H_c(T) = H_c(0) \left(1 - \left(\frac{T}{T_c} \right)^2 \right), \quad (2.23)$$

$$H_c(0) = \sqrt{\frac{0.472}{\mu_0} \gamma T_c}. \quad (2.24)$$

Here γ is the coefficient of the linear electronic specific heat in the normal state, and μ_0 is the permeability constant. One consequence of Equation (2.23) is that cavities made of higher temperature superconductors, such as Nb_3Sn , can operate at higher fields.

For a certain class of superconductors, the theoretical limit H_c is not sufficient to describe their behavior. This class is called Type II superconductors and is important for us because it includes pure niobium. For a Type II superconductor, it

is energetically favorable for magnetic flux to enter inside the superconductor below H_c . Above a lower critical field, H_{c1} , the superconductor breaks up into normal and superconducting zones in a periodic lattice arranged periodically (Figure 2-9). Up to the upper critical field, H_{c2} , part of the material remains superconducting. The transition from the superconducting state to the normal state therefore does not happen sharply at $H = H_c$, but is instead happening continuously between $H = H_{c1}$ and $H = H_{c2}$, where $H_{c1} < H_c < H_{c2}$.

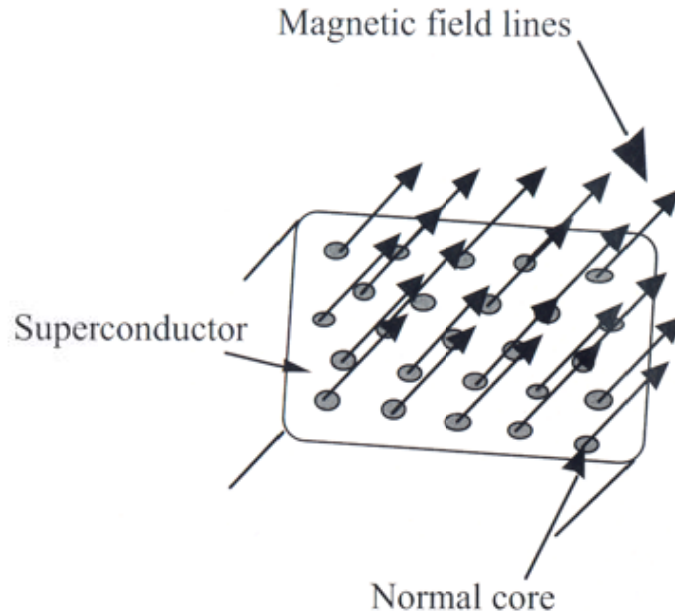


Figure 2-9: Normal-conducting regions appearing inside a superconductor at a magnetic field level $H > H_{c1}$. The picture is taken from [31].

For pure niobium, the values for the 3 critical fields at zero temperature are [31]:

$$H_{c1} = 170 \text{ mT}, \quad H_c = 200 \text{ mT}, \quad H_{c2} = 240 \text{ mT}. \quad (2.25)$$

Assuming a typical ratio of the peak surface magnetic field to the accelerating gradient to be $4.3 \text{ mT}/(\text{MV}/\text{m})$, as in the 5-cell cavity design from [44], we get the following maximum accelerating gradients, corresponding to the 3 critical magnetic fields: $E_{c1} \approx 40 \text{ MV}/\text{m}$, $E_c \approx 47 \text{ MV}/\text{m}$, $E_{c2} \approx 56 \text{ MV}/\text{m}$.

In practice, however, achieved surface fields are always lower than the theoretical

limits. This is due to other effects limiting the fields: multipacting, quenching, and field emission. These three effects are described below.

Multipacting

Multipacting in RF structures is a resonant process in which a large number of electrons build up spontaneously, absorbing RF power. Thus, it becomes impossible to increase the cavity fields by raising the incident power. The electrons collide with structure walls, leading to a large temperature rise and eventually, in the case of superconducting cavities, to thermal breakdown (quenching).

The accepted mechanism for multipacting is as follows: an electron is emitted from one of the structure's surfaces. This may be precipitated by a cosmic ray, photoemission, or an impacting field emission electron. The emitted electron is accelerated by the RF fields and eventually impacts a wall again, thereby producing secondary electrons. The number of secondary electrons depends on the surface characteristics and on the impact energy of the primary. In turn, the secondaries are accelerated and, upon impact, produce another generation of electrons. The process then repeats. The electron current increases exponentially if the number of emitted electrons exceeds the number of impacting ones and if the trajectories satisfy specific resonance conditions.

The most successful solution to multipacting is to round the cavity walls to make an elliptical cavity (Figure 1-4). In such shape, the magnetic field varies along the entire cavity wall so that there are no stable electron trajectories, as electrons drift to the equator within a few generations. At the equator, the electric field perpendicular to the wall vanishes, so that the secondaries do not gain any energy and the avalanche is stopped (Figure 2-10).

Although the introduction of SRF cavities of elliptical shape allowed to largely avoid multipacting in cavities working with ultra-relativistic beams, it can still be a major concern for structures of more complex shapes. This applies to low- β cavities, couplers, transmission lines, RF windows, and, most importantly, PBG cells.

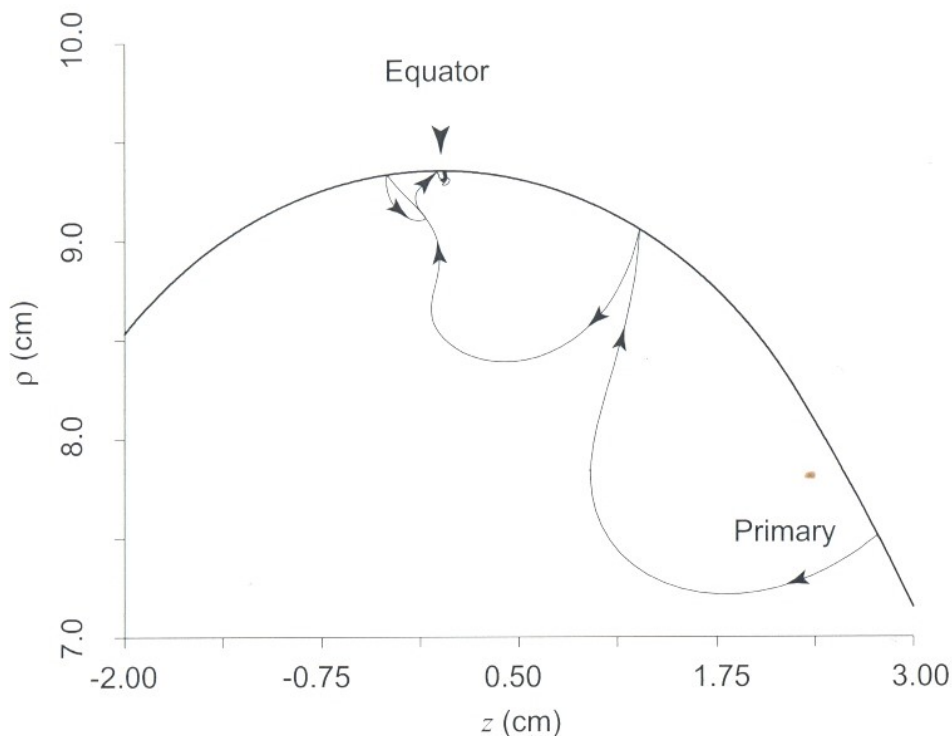


Figure 2-10: Electron trajectories in an elliptical cavity [31]. The charges drift to the equator where multipacting is not possible.

Quenching

Thermal breakdown, or quenching, is a phenomenon that limits the achievable field below the theoretically expected critical magnetic field discussed above. Thermal breakdown originates at “defects” - regions of sub-millimeter-size that have RF losses substantially higher than the surface resistance of an ideal superconductor. It results in a sudden transition from the superconducting state to the normal conducting state with a sharp drop in the RF cavity unloaded quality factor.

In the DC case, supercurrents flow around defects. But at RF frequencies, the reactive part of the impedance causes the RF current to flow through the defect, producing Joule heating. When the temperature at the outside edge of the defect exceeds T_c , the superconducting region surrounding the defect becomes normal conducting, resulting in greatly increased power dissipation. As the normal conducting region grows, the power dissipation increases, resulting in a thermal instability as

sketched in Figure 2-11.

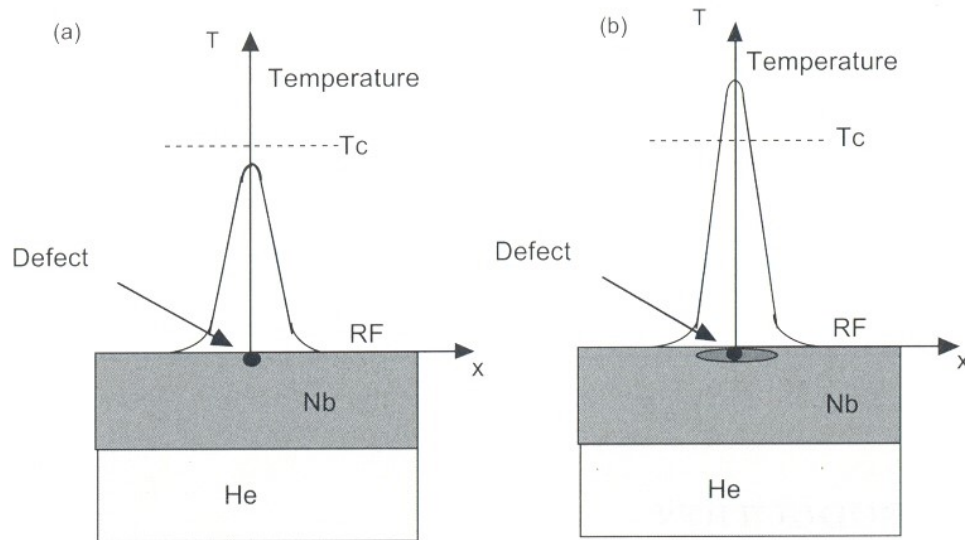


Figure 2-11: Quenching on the surface of a niobium cavity at the location of a defect [31]. (a) At low field, the temperature in the vicinity of the defect is higher than that in surrounding areas but lower than T_c . (b) As the field is raised, the temperature exceeds T_c , so that the niobium near the defect becomes normal conducting, and the power dissipation increases unstably.

During a cryogenic test, a quench produces characteristic traces of the saw tooth shape for the transmitted and reflected power, as shown in Figure 2-12. When an input RF pulse is turned on, the cavity fills and the reflected power decreases. The stored energy and the transmitted power increase until the quench field is reached. At this point, the power dissipation at the defect drives a large portion of the cavity surface normal. Eventually coupling to the input coupler is lost, and all the power is reflected. Once the field is sufficiently low and the cavity cools, the Q-factor restores to its original value and the cavity fills with RF power again. The entire process then repeats.

As opposed to a quench in a superconducting magnet, a quench in an SRF cavity does not involve a severe loss of energy (only from a few joules to a few tens of joules). As a result, a superconducting cavity can recover from quench within milliseconds.

One of the most effective ways to suppress quenching is to improve the purity of niobium. A quantity that characterizes purity of niobium is called the “residual

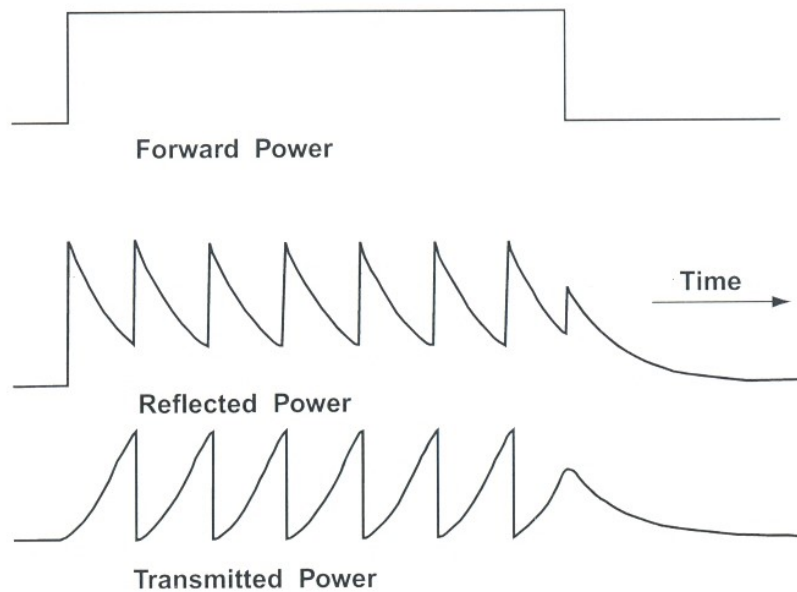


Figure 2-12: RF power levels for a cavity during quenching [31]. The power reflected from the cavity and the power transmitted through the cavity exhibit the saw tooth shape.

resistance ratio” (RRR) and is defined as the factor by which DC resistivity drops from its room-temperature value to its residual value. Various techniques to increase RRR are described in [31]. Commercially available niobium typically has RRR of 250 and higher.

Field emission

Electron field emission is a loss mechanism that occurs at high electric field levels limiting the accelerating gradient achieved by the superconducting RF cavities [79, 80]. In that way, field emission is fundamentally different from quenching, which is related to the surface magnetic field, as was discussed above.

The effect is caused by the emission of electrons from the regions of the high electric field on the cavity surface, called “emitters”. The emitted electrons travel in the RF fields of the cavity and impact the cavity’s surface (Figure 2-13). This leads to excessive heating and production of X-rays that can be seen if X-ray detectors are used during an experiment. Temperature mapping can also be used to locate the

source of emission and the trajectories of the emitted electrons.

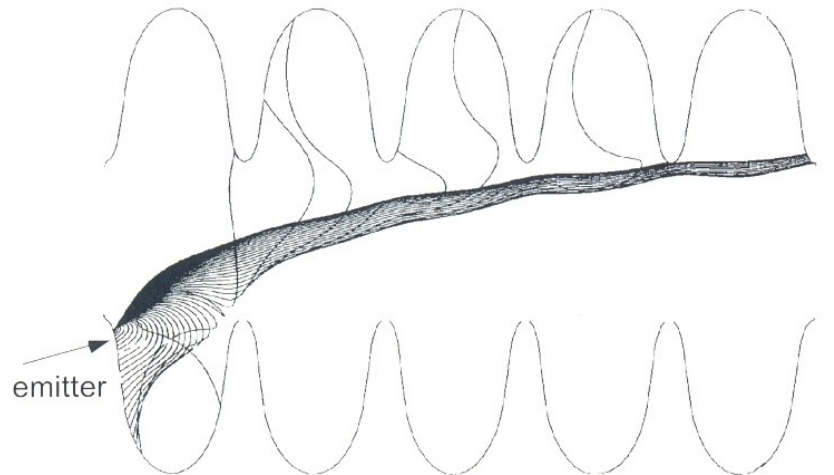


Figure 2-13: Calculated trajectories of emitted electrons in a 5-cell 1.5 GHz cavity [31].

The process of field emission is explained by the theory developed by Fowler and Nordheim [81]. The theory showed that in the presence of an electric field, electrons tunnel out of the metal into the vacuum because of their quantum wave-like nature. However, a comparison with the observed currents reveals that at a given emission is substantially higher than the theory predictions. Traditionally, the excess has been attributed to a “field enhancement factor”, which is believed to be related to the physical properties of the emitter.

The increase in power dissipation due to bombarding electrons leads to an exponential drop in the cavity Q-factor, hence limiting the achievable gradient. Occasionally, the active field emitters are processed (eliminated) and the gradient will be recovered. Otherwise, a higher gradient cannot be achieved unless the input RF power is increased. Frequently, field emission is observed in SRF cavities at high RF fields limiting the peak electric fields achieved below 40 MV/m. Improved techniques followed in maintaining clean conditions during cavity surface processing and assembly have facilitated in achieving higher peak electric fields far above 40 MV/m.

2.4 Summary

In the first section of this Chapter, we presented the theory of wakefields and higher order modes (HOMs). The main result of the section is the introduction of two ways to mathematically characterize the “dangerousness” of HOMs, i.e. the strength of their negative impact on a particle beam. The first way is to calculate the wake impedance $Z(\omega)$, and the second way is to calculate the deflecting voltages $V_{\perp n}$. The two ways will be explored in the design of the cavity (Chapter 3) through wakefield simulations and eigenmode simulations, respectively.

In the second section of this Chapter, we briefly described the theory of two-dimensional metal PBG structures. The main result of the section is summarized in the plot of the global band gaps (Figure 2-6) which describes the properties of a PBG structure with respect to a parameter a/b of the photonic lattice. For a particular choice of the parameter, the plot of the global band gaps reduces to a dispersion diagram shown in Figure 2-5. Figures 2-6 and 2-5 will be used in Chapter 3 of this thesis to justify the choice of parameters of the PBG lattice.

In the third part of this Chapter, we presented a short summary of radio-frequency superconductivity. The main results are the estimate of the surface resistance of niobium (Equation (2.25)) and the description of limits of SRF cavity performance. Both of these concepts are used in the experimental part of this thesis (Chapter 6).

Chapter 3

Design and simulations

SRF cavities with PBG cells can be useful for particle accelerators that require strong higher order mode (HOM) damping. A multi-cell cavity is needed to achieve a high “real-estate gradient” (see Glossary). In this Chapter, we describe the design of the five-cell niobium cavity with an incorporated PBG cell in the middle. First, the dimensions of the cavity are chosen and its accelerating properties are calculated. Second, the HOM spectrum is analyzed in the cavity with the dimensions assigned in the first step. The dimensions of the cavity are adjusted to achieve the desired HOM damping properties.

3.1 Photonic band gap lattice

The main idea of forming an RF cavity by removing a rod from a PBG lattice was discussed in Chapter 1. In this section, we discuss the features of the PBG lattice that can be chosen based on relatively straightforward 2D simulations in the plane transverse to the beam path. They include the choice of the lattice parameter a/b , the choice of the number of PBG lattice rows, the shapes of the rods, and possible modifications to the lattice (see Appendix A and additional files in Supplemental Materials [1]). However, the final optimization of the geometry must be done using a 3D simulation that includes all five cells, and will be described in further sections of this Chapter.

3.1.1 Choice of the lattice parameter

As was discussed in Chapter 2, properties of a triangular PBG lattice depend only on one parameter – the ratio of the rods radius a to the distance between centers of the rods b . The parameter a/b is chosen based on the global band diagrams (Figure 2-6). A choice of a/b imposes a vertical line in Figure 2-6 that slices through the regions of “propagation” and “no propagation”.

An example of the dispersion diagram in an infinite photonic crystal for $a/b = 0.15$ was shown in Figure 2-5. At this ratio of a/b , only one band gap exists for the TM polarization and no band gaps exist for the TE polarization. To apply this dispersion diagram to the resonator formed by a single removed rod, we added dashed straight lines to show the frequencies of the monopole and the dipole modes in the resonator (see Figure 3-1). An intersection of a dashed line with a band means that the corresponding resonator mode can couple to a wave propagating in the PBG lattice (see Chapter 2).

As shown in Figure 3-1, the dashed line corresponding to the frequency of the monopole mode does not intersect any TM bands and therefore is confined. The dipole mode has its frequency outside of the band gap and corresponds to the dashed line that intersects the bands. Hence, the dipole mode is allowed to leak out to the periphery of the PBG structure by coupling to the Bloch waves in the lattice. HOMs of a higher order (quadrupole, etc.) have frequencies greater than that of the lowest dipole mode, thus, they propagate through the structure and can be damped (both the TM and the TE polarizations).

The choice of $a/b = 0.15$ therefore satisfies the requirements to the PBG lattice. The first traveling wave copper PBG structure tested at MIT [50] utilized an a/b of 0.15. All of the single SRF PBG cells tested at LANL [63, 64], also utilized $a/b = 0.15$. For the 5-cell cavity with a PBG cell, we therefore chose the parameter a/b to be equal 0.15.

The band diagrams in Figure 3-1 were plotted for $k_z = 0$ (zero variation along the axis of the rods). In the real three-dimensional structure, we have to account for a

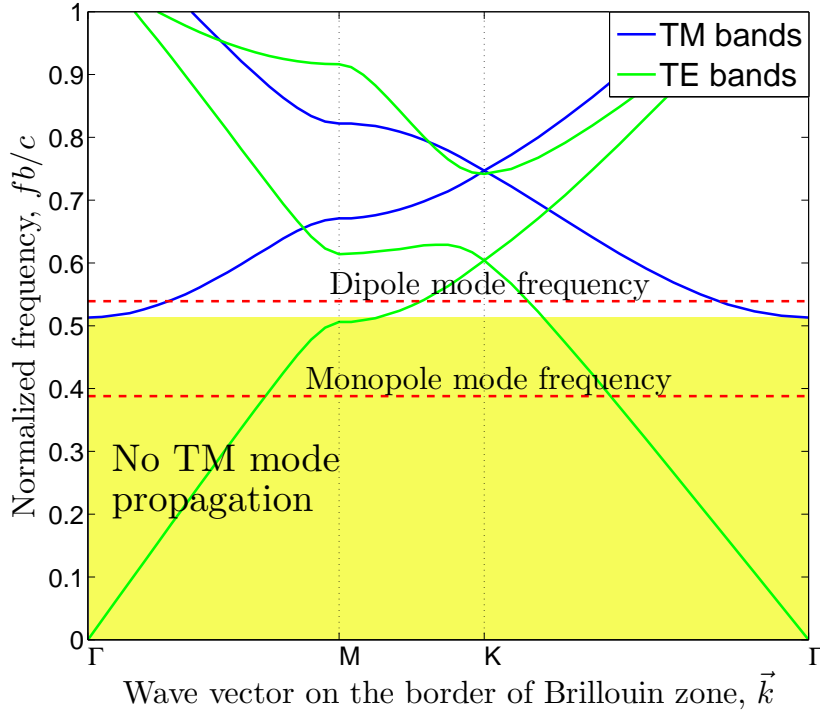


Figure 3-1: Frequency of eigenmode solutions in an infinite photonic crystal as a function of wave vector in the plane of the crystal. The crystal has a triangular lattice of metal rods with a ratio of the rod radius, a , to the spacing between the rods, b , equal to 0.15. Frequencies are shown for the monopole and the dipole modes with dashed straight lines in a resonator formed by a single removed rod.

non-zero k_z in the central region of the cell (see the π -mode below). The adjustment for the non-zero k_z means that the monopole mode is deeper in the band gap, as was discussed in see Chapter 2. To make sure that HOMs with $k_z \neq 0$ do not enter the gap, their Q-factors should be carefully simulated using 3D simulations.

3.1.2 Truncation of the photonic band gap structure

Once the type of the PBG lattice is chosen, we must choose where the lattice should be truncated. We wish to use as many layers of rods as possible for the best confinement of the accelerating mode (layers are shown in white dashed lines in Figure 3-2). However, for a cavity operating at the frequency of 2.1 GHz, size limitations practically allow only a few layers. Otherwise, the structure becomes too big, hard to

fabricate, and unfit for any realistic accelerator beamline.

Early ideas for a multi-cell SRF PBG structure involved a design with three layers of PBG rods, open in the transverse plane (Figure 3-2). However, it was quickly realized that due to the constraint of only having a few layers of PBG rods, the designed structure must be “closed” in the transverse plane, as shown in Figure 3-3. This is a fundamental difference between room-temperature PBG cavities and the designed SRF PBG cavity.

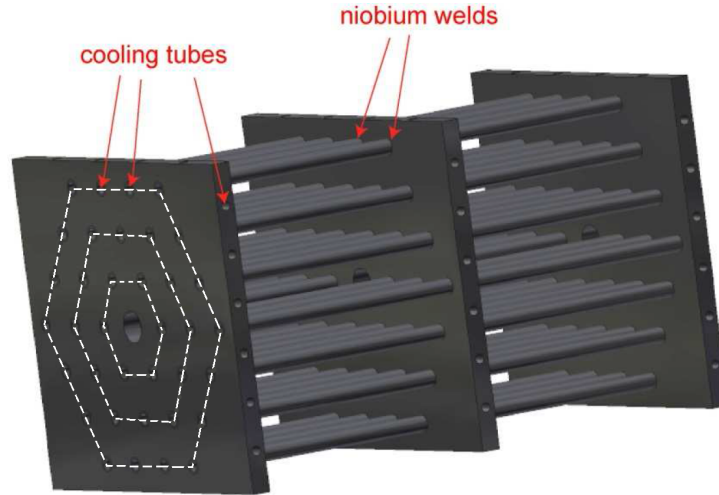


Figure 3-2: An early idea of an open SRF PBG structure with three layers of rods (shown with white dashed lines). Cooling is done through tubes inside the PBG rods and the walls.

The main reason to make the cavity closed is to provide a high enough diffractive Q-factor [63]. The diffractive Q-factor accounts for the losses related to the radiation from the structure in the transverse direction:

$$Q = \frac{\omega U}{P_{diff}}, \quad (3.1)$$

where ω is the angular frequency of the mode, U is the electromagnetic energy stored in the mode, and P_{diff} is the diffractive power loss. The diffractive losses can limit the total Q-factor to a relatively low value of $Q = 1.2 \times 10^5$, as was measured for the cavity from [62] (see Chapter 1). Although diffractive losses in SRF cavities are not dissipated in liquid helium and do not require an additional refrigerator power,

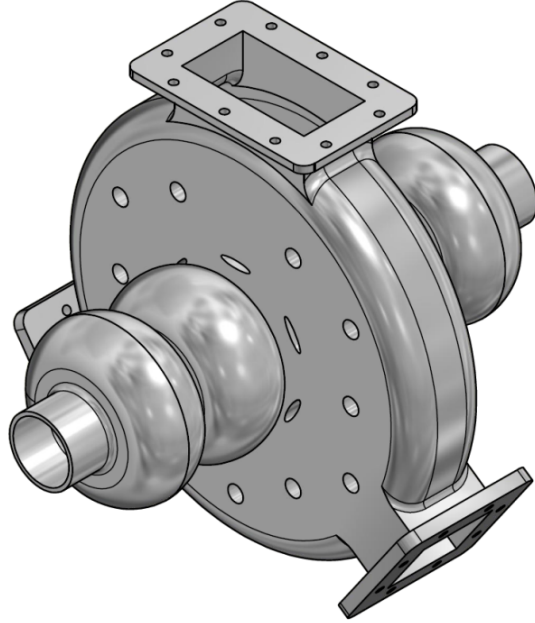


Figure 3-3: A drawing of the 5-cell SRF cavity with a PBG cell “closed” in the transverse plane with a metal wall. The entire structure is made of pure niobium

they can still constitute a significant part of RF power loss, and have to be minimized. Keeping the PBG cell “closed” solves this problem.

Another advantage of a closed cavity is the fact that the entire field of SRF technology is developed for cavities that can be immersed in a single helium bath. An open structure would require a more sophisticated cooling scheme, ensuring that helium does not fill the inside of the cavity. Even a simple cryogenic test without a particle beam would require a complex cooling structure to allow helium flow in the pipes instead of using a helium tank.

It was therefore decided to make the SRF PBG cell closed in the transverse plane by a niobium wall. HOM damping in this design is done through HOM waveguide couplers attached to the enclosing wall. The accelerating mode should have a frequency below the cut-off of the HOM waveguides. The mode is therefore confined by a combination of layers of the PBG lattice and exponential decay inside the HOM waveguides.

It was found by simulations that for such a configuration, two layers of PBG lattice is sufficient to confine the accelerating mode well enough (see Appendix A and

additional files in Supplemental Materials [1]). A schematic of the 2-layer PBG cell is shown in Figure 3-4. The cell has round and elliptical rods that will be introduced later in this section. The 2-layer configuration to a sufficiently high degree still has the frequency selective properties of the infinite photonic crystal but is much easier to fabricate than a 3-layer structure.

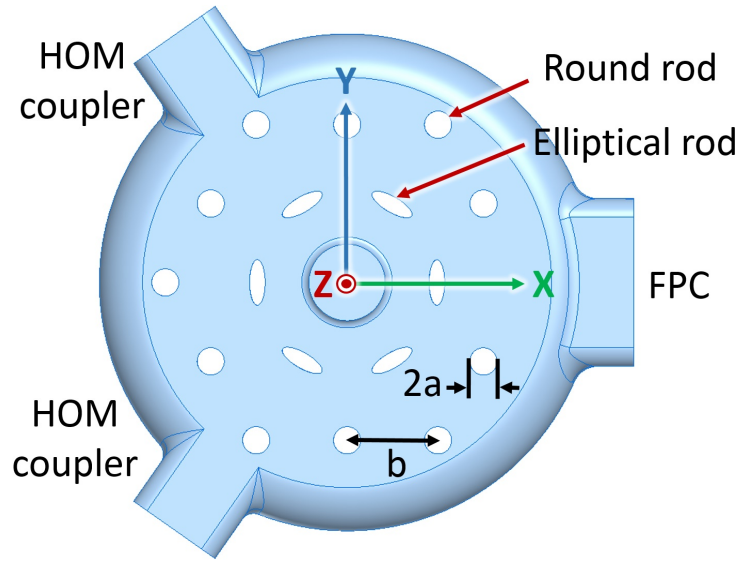


Figure 3-4: PBG cell as seen from the Z axis pointing along the beam trajectory. The vacuum region is shown in blue.

3.1.3 Optimization of the photonic band gap lattice

The translational symmetry of the perfect triangular lattice is responsible for the frequency selective property of PBG structures, as was discussed in Chapter 2. One might therefore assume that breaking the perfect triangular lattice can negatively impact HOM damping properties of the structure. However, it turns out that for a particular HOM, damping can be optimized by slightly displacing the rods from the vertices of the triangular lattice. In this section, we consider the possibility of altering the lattice in a metal triangular PBG structure.

The idea of displacing PBG rods from vertices of the triangular lattice was first explored by Bauer et al [53]. A dielectric PBG structure was optimized using numerical simulations described in [53] in order to improve confinement of the operating

monopole mode. The optimization had a constraint of keeping the 6-fold rotational symmetry of the original triangular lattice. During the process of optimization, some rods were displaced quite far from their original positions, merging other rods. Diffractive Q factor of the accelerating mode was improved by about two orders of magnitude. The monopole mode in the optimized dielectric structure from [53] is shown in Figure 3-5.

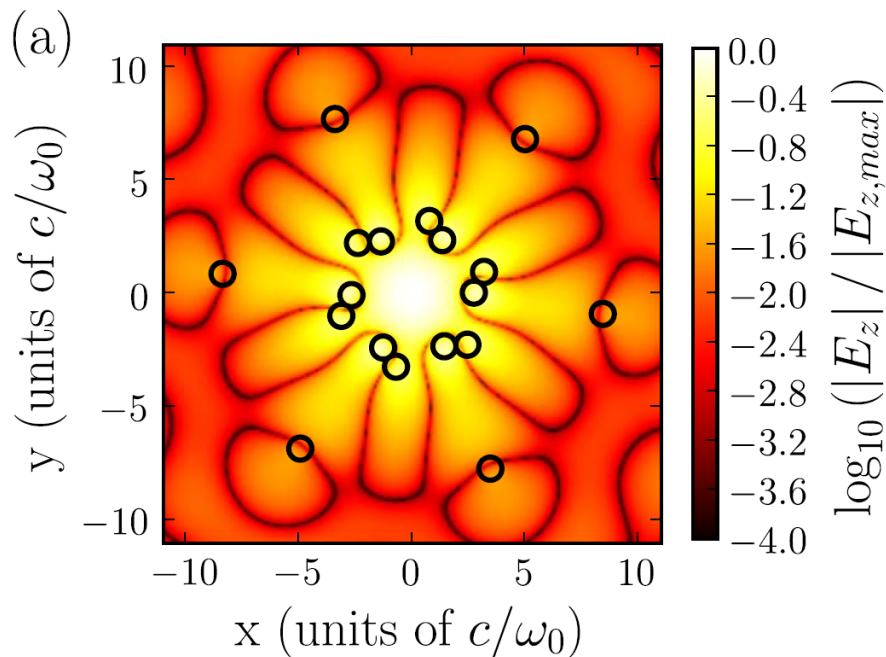


Figure 3-5: Optimized dielectric PBG cavity from [53]. Color is showing normalized electric field of the confined mode.

We first tried the same approach for a metal PBG structure, however, no major improvement in the confinement of the operating mode was observed. Therefore, another approach was used. We attempted to improve HOM damping (decrease diffractive Q-factor of the first dipole HOM Q^{dip}) while keeping the Q-factor of the operating monopole mode Q^{mon} constant. Simulations were carried out in the eigenmode solver of the Ansys HFSS [71] (see Appendix A and additional files in Supplemental Materials [1]). The goal function (i.e. the maximized quantity) was defined based on the Q-factor of the first dipole mode TM_{11} , and the steepest descent method was employed with the constraint $Q^{mon} \geq Q_0^{mon}$. The requirement to keep

Table 3.1: Comparison between diffractive Q-factors for the first monopole and the first dipole modes in the original and the optimized geometry

	TM ₀₁ -like mode	TM ₁₁ -like mode
Original geometry, black circles in Figure 3-6	3150	46
Optimized geometry, red circles in Figure 3-6	3220	10.7

the 6-fold rotational symmetry reduced the number of rods in the optimization to only three.

We found that unlike in the case of the dielectric PBG structure from [53], relatively small displacements of the rods from their original positions resulted in a dramatic improvement of damping of the first dipole HOM. The optimized geometry is compared to the original in Figure 3-6. Without a significant change in Q^{mon} , Q^{dip} was reduced by a factor of four, as summarized in Table 3.1. The monopole and the dipole modes in the original and the optimized geometries are shown in Figure 3-7.

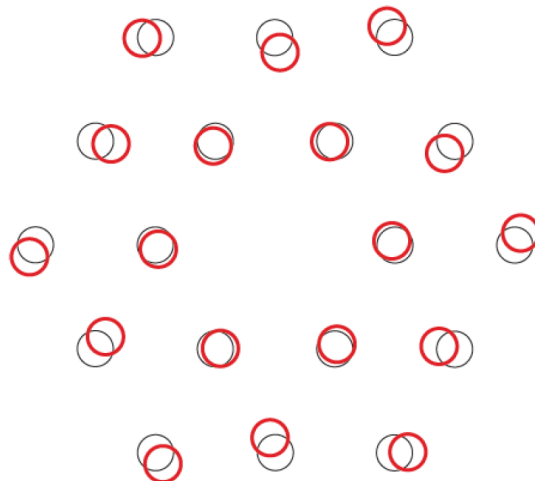


Figure 3-6: Initial and optimized positions of the rods in the metal PBG structure (black and red circles, respectively). The scale is arbitrary, the obtained results apply to a structure of any size.

An attempt was made to apply this optimization for the case of multiple HOMs. Unfortunately, optimizing a single HOM typically makes damping of other modes worse. Thus, the factor of four of improvements in HOM damping do not seem to be

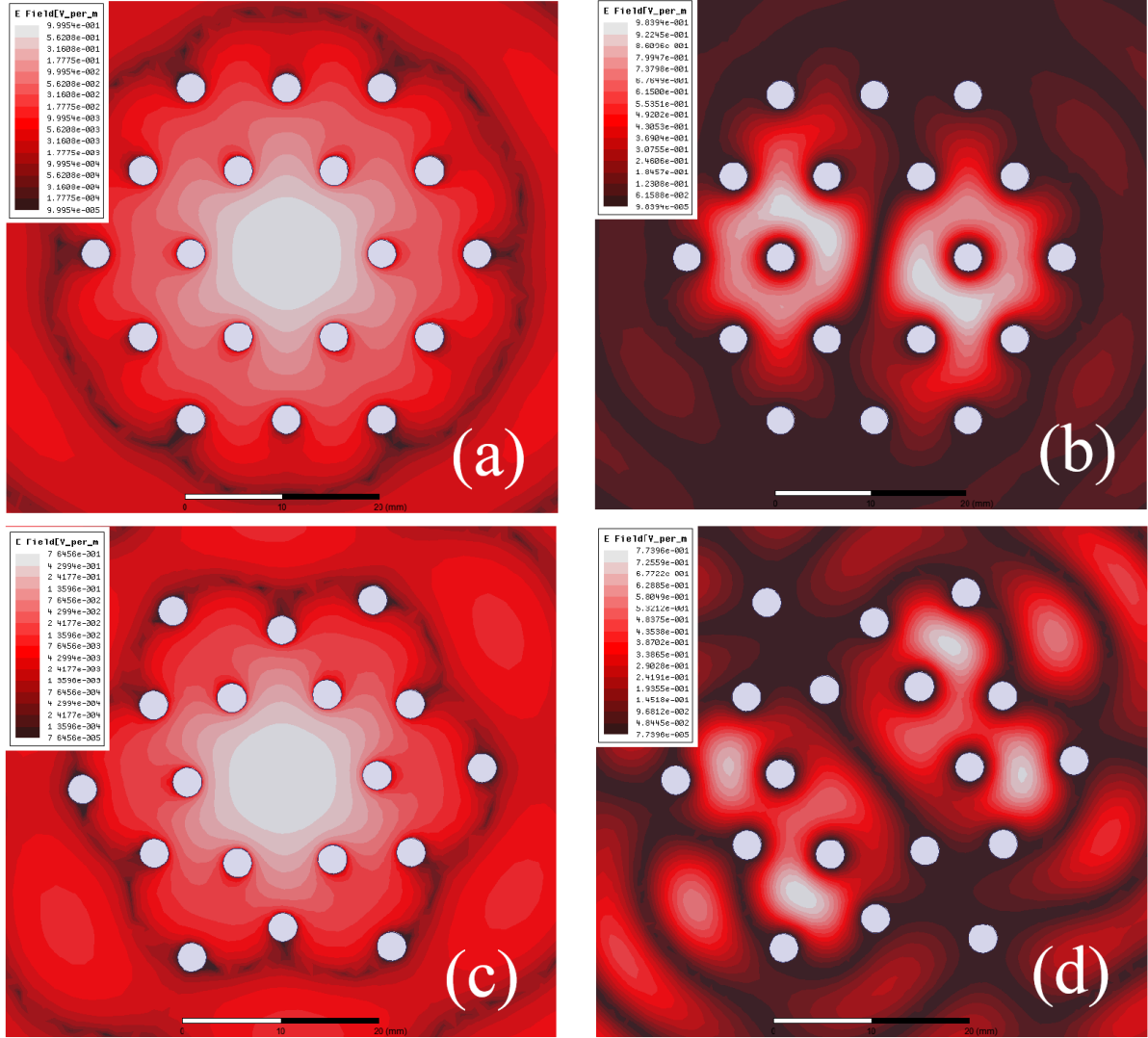


Figure 3-7: (a) Regular metal triangular lattice, monopole mode, $Q=3150$. (b) Regular metal triangular lattice, dipole mode, $Q=46$. (c) Optimized metal triangular lattice, monopole mode, $Q=3220$. (d) Optimized metal triangular lattice, dipole mode, $Q=10.7$. Simulation setups are described in Appendix A and additional files are provided in Supplemental Materials [1].

feasible for the case of multiple modes. A more complicated goal function is needed to assign weights to HOMs with higher impedance. Also, the 3-dimensional nature of the modes in the real structure makes the simulations more complex and time-consuming. Hence, we decided to keep the perfect triangular lattice for the design presented in this thesis. The option of breaking the triangular lattice in metal PBG structures in order to improve HOM damping remains open and can be explored in

future work.

3.1.4 Shape of the photonic band gap rods

When compared to more traditional shapes for an accelerating cavity, a PBG cell has certain disadvantages. In a PBG cell, the ratio of the peak surface magnetic field to the accelerating gradient is higher than in a cavity of the “pillbox” shape typical for room-temperature accelerators, or an elliptical cavity typical for superconducting accelerators. The peak surface magnetic field is reached on the surface of the first layer of the PBG rods.

In SRF cavities, the surface magnetic field increases the probability of quenching and hence the probability of a loss of coupling to the operating mode (see Chapter 2). For room-temperature accelerators, high surface magnetic field results in high Ohmic heating on the surface of the PBG rods and operational fatigue.

This problem was first addressed in [82, 83, 84]. The proposed solution was to alter the shapes of the first row of PBG rods to reduce the surface curvature at the high field region. This idea led to an elliptical shape of the first 6 rods, as can be seen in Figure 3-8. The authors of [82] stated that the chosen ellipticity of 1.5 is sufficient to reduce heating on the inner row of rods significantly.

This idea was further developed by Simakov et al. [85]. The authors of [85] found the optimal value of ellipticity that minimizes the peak magnetic field on the surface of the rods. The optimization was conducted with a requirement to preserve the HOM damping properties and the confinement of the accelerating mode in the PBG structure. The study focused specifically on superconducting PBG cells with two layers of PBG rods.

The authors of [85] analyzed three different ways to optimize the geometry and found that making the first row of the rods elliptical and shifting it slightly towards the center satisfies both requirements. Shifting the rods compensates for the small change in frequency of the accelerating mode due to the change in the rods’ minor radius. Satisfactory values of the major rod radius, the minor rod radius, and the shift towards the center were found to be $0.25 b$, $0.0865 b$, and $0.0165 b$, respectively

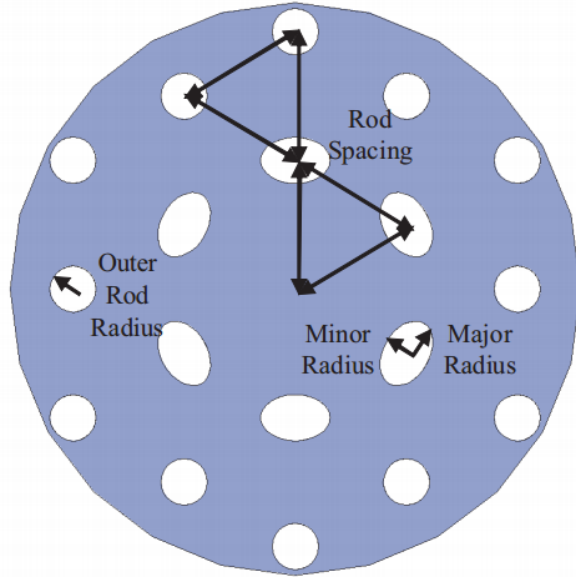


Figure 3-8: Elliptical rod PBG structure for breakdown testing at SLAC [82].

(b is the spacing between the rods). The original and the optimized geometries are shown in Figure 3-9.

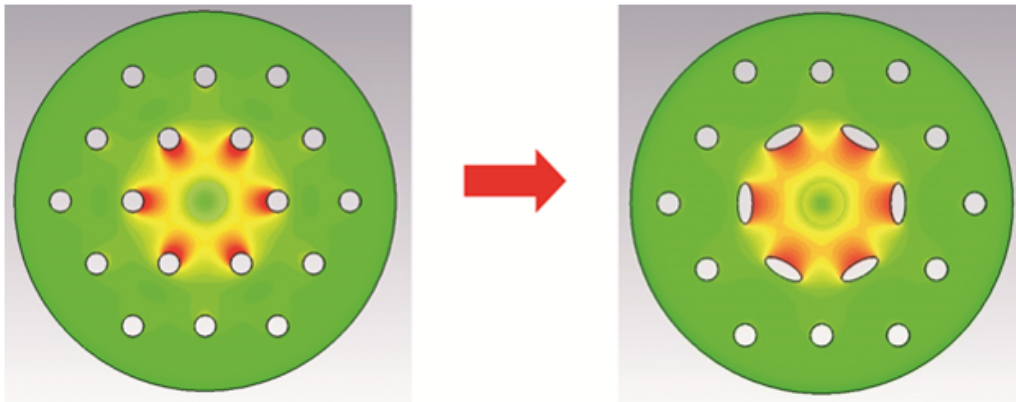


Figure 3-9: Change in the shape of the inner rods of the PBG cavity to reduce peak surface magnetic fields [85].

Single-cell PBG cavities were made of niobium for both the original design shown in the left part of Figure 3-9 and the optimized design shown in the right part of Figure 3-9. Two single cells of each design were tested at cryogenic temperatures. The optimized geometry performed better, showing on average 30% higher maximum achieved accelerating gradient [64]. The tests proved the advantage of altering the

shape of the first layer of PBG rods.

For the design of the 5-cell cavity with a PBG cell, we decided to take advantage of the optimized geometry from [85]. The major and minor semi axis of the elliptical rods were therefore chosen to be $0.25 b$ and $0.0865 b$, respectively. The shift towards the center was adjusted to give the right frequency for the exact geometry of the cell, which was slightly different from the design from [85]. The value of $0.0122 b$ was chosen for the shift.

3.2 Design of the photonic band gap cell

After the configuration of the PBG lattice had been defined, we proceeded with the design of the PBG cell itself. In order to form a cell, the lattice needed to be incorporated inside a cylindrical shell and couplers or ferrite absorbers needed to be placed at the periphery of the shell for HOM damping. The geometry of the cell is schematically shown in Figure 3-10.

Putting absorbers inside the superconducting cavity has certain disadvantages such as an increased power dissipation at the cryogenic temperature and possible problems with outgassing from absorber's material. We, therefore, decided to use external couplers in order to dissipate power in RF loads outside of the superconducting region. Rectangular waveguides were chosen as external HOM couplers, similar to a JLAB's 5-cell cavity from [44], designed for a high-current application. Another possible solution was to use coaxial antennas, such as in the TESLA 9-cell cavity [65]. The advantage of rectangular waveguides over coaxial antennas is their simplicity and better cooling. The latter is especially important for high-current accelerators. For comparison, loop-type HOM couplers, which are adopted for the TESLA cavity, have a heating problem for the CW operations [86].

Similar to the HOM couplers, the fundamental power coupler (FPC) was attached to the periphery of the PBG cell (the upper waveguide in Figure 3-10). The same approach was previously implemented for the room-temperature MIT structure [73]. Besides feeding power at the frequency of the accelerating mode into the cavity, the

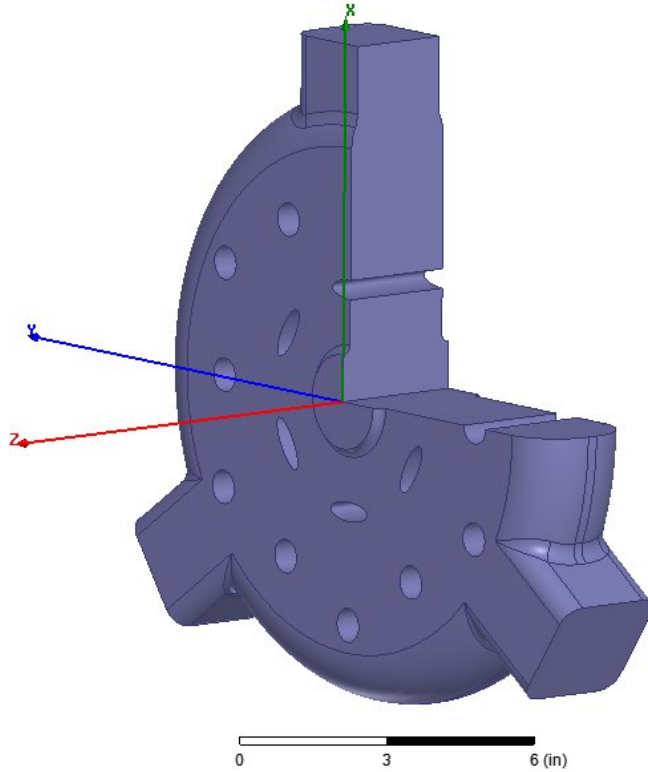


Figure 3-10: The vacuum region enclosed by the PBG cell. One quarter of the cell is cut out to show the structure. The beam goes along the z -axis.

FPC can also serve as an additional HOM coupler, assuming that a broadband RF window is used in the FPC waveguide as well as the HOM waveguides. The FPC has dimensions of a standard waveguide size WR430, as shown in Figure 3-11. The corners of the waveguide are rounded, as was needed for the fabrication process (see Chapter 4). To feed RF power into the cavity, the lowest frequency waveguide mode TE_{01} is employed. As can be seen in Figure 3-11, the PBG rod located closest to the FPC was removed in order to provide stronger coupling to the FPC (see the next section).

We chose to use two HOM waveguide couplers in addition to the FPC. Two is the lowest number of couplers to provide reasonable damping to both the dipole and the quadrupole modes. If only one HOM coupler was used, we would need to position it at the right angle to the FPC to obtain efficient damping of the two polarizations of the dipole mode. However, such configuration fails to damp certain quadrupole

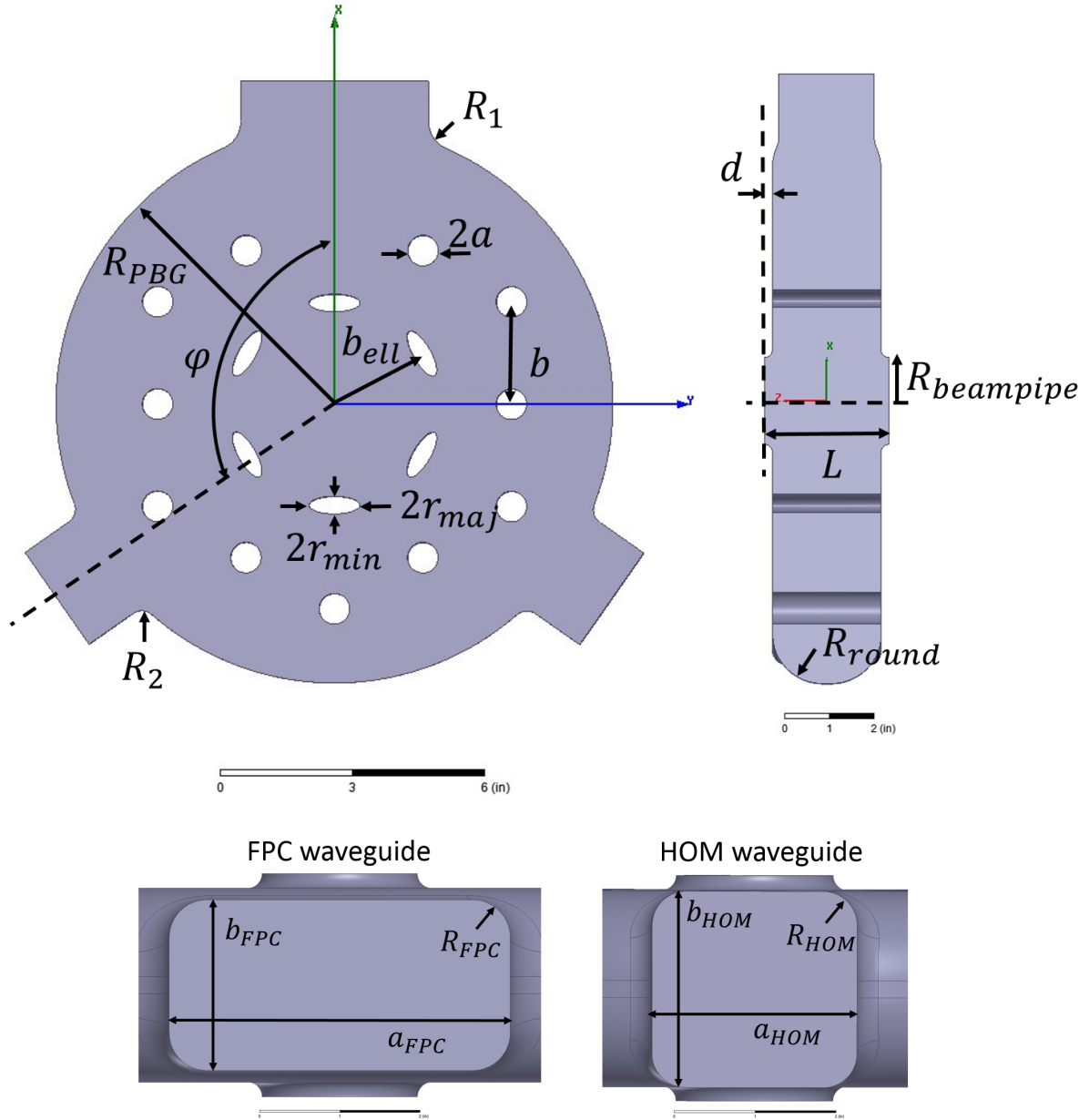


Figure 3-11: Main dimensions of the PBG cell (top) and dimensions of the waveguides attached to the cell (bottom). The vacuum region is shown in blue. The pictures are taken from HFSS eigenmode simulations provided in Supplemental Materials [2].

modes with zero fields at the angular positions of the waveguides. Using more than two HOM waveguides in addition to the FPC can provide better HOM damping, but makes the structure more complicated and harder to fabricate.

Customized dimensions were chosen for the two HOM waveguides in order to maximize HOM damping. The dimension along the z axis was chosen equal to the

distance between the walls of the cell so that the waveguide walls are flush against the walls of the cavity. This length in the z direction was chosen to lower the cutoff frequency for TE modes polarized the direction that is perpendicular to the z -axis. The other dimension (along the z -axis) was a subject of optimization and was chosen to maximize damping of the ten most harmful HOMs (see Section 3.5). The corners of the HOM waveguides were rounded similar to the FPC to facilitate the fabrication process (see Chapter 4).

The total length of the PBG cell (parameter L in Figure 3-11) was chosen to satisfy the resonance condition between the accelerating mode and the ultrarelativistic beam of electrons ($v \approx c$). For more efficient coupling between the mode and the beam, the accelerating mode must have the phase advance of $\phi_{cell} = \pi$ over the length of one cell, as will be discussed below. The resonance condition dictates the time of passage of one cell L/c to be equal to the time it takes the phase of the accelerating mode to advance by ϕ . Hence

$$L = \frac{c \phi_{cell}}{f 2\pi}, \quad (3.2)$$

where f is the frequency of the accelerating mode equal to 2.1 GHz.

Following a standard practice for both room-temperature and superconducting accelerating cavities, the iris of the PBG cell was rounded to avoid field enhancement in the region. Since the total length L is fixed, a change in the iris rounding radius (d in Figure 3-11) causes a change in the distance between the walls of the PBG cell, and affects the HOM damping properties. The rounding radius can, therefore, be regarded as another parameter that needs to be optimized for better HOM damping. Final dimensions of the PBG cell were chosen based on optimization of the HOM damping in the 5-cell cavity with the incorporated PBG cell (see the next section) and are summarized in Table 3.2.

3.3 Design of the elliptical cells

Elliptical cells are traditionally used in SRF cavities. Figure 1-4 shows an example of a multi-cell accelerating cavity consisting of elliptical cells. One reason to deviate from

Table 3.2: Final dimensions of the PBG cell, shown in Figure 3-11.

Inner radius of the PBG cell, R_{PBG}	6.38 in
Angle between the FPC and the HOM waveguides, ϕ	125°
Distance between the centers of the elliptical PBG rods, b_{ell}	2.311 in
Distance between the centers of the round PBG rods, b	2.34 in
Radius of the round PBG rods, a	0.351 in
Minor semi-axis of the elliptical PBG rods, r_{min}	0.202 in
Major semi-axis of the elliptical PBG rods, r_{maj}	0.585 in
Rounding radius of the FPC-cavity joint, R_1	0.675 in
Rounding radius of the HOM waveguide-cavity joint, R_2	0.35 in
Rounding radius of the cavity-beam-pipe joint, d	0.183 in
Total length of the PBG cell, L	2.812 in
Radius of the beam-pipe, $R_{beam-pipe}$	0.982 in
Rounding radius of the edge of the PBG cell, R_{round}	1.115 in
Height of the FPC waveguide, b_{FPC}	2.15 in
Width of the FPC waveguide, a_{FPC}	4.3 in
Rounding radius of the FPC waveguide, R_{FPC}	0.475 in
Height of the HOM waveguides, a_{HOM}	2.558 in
Width of the HOM waveguides, b_{HOM}	2.446 in
Rounding radius of the HOM waveguides, R_{HOM}	0.423 in

the simplest cylindrical “pillbox” shape is to mitigate the negative multipacting effect, as was discussed in Chapter 2. Another reason has to do with the process of chemical treatment of the inside surface of SRF cavities [31]. Geometries of different elliptical cells can be divided into several types. Among them is the so-called “low-loss” shape, optimized to minimize the losses due to RF currents in the cavity walls.

The four elliptical cells in the five-cell cavity were chosen to be of the “low loss” shape. The vacuum region enclosed by the cell is shown in Figure 3-12. The “low-loss” shape was originally developed for the JLAB’s highly damped five-cell module at 748.5 MHz described in [44]. The structure was also designed for a high-current application and successfully tested at cryogenic temperatures [87, 88, 89, 90, 91]. The dimensions of elliptical cells from the JLAB’s structure were scaled to the frequency of 2.1 GHz. and are shown in Figure 3-13.

Following the design from [44], the elliptical cells at the ends of the 5-cell cavity were trimmed at the equator to ensure that the peaks of the accelerating gradient are equal in all elliptical cells. If the end elliptical cells were of the same shape as

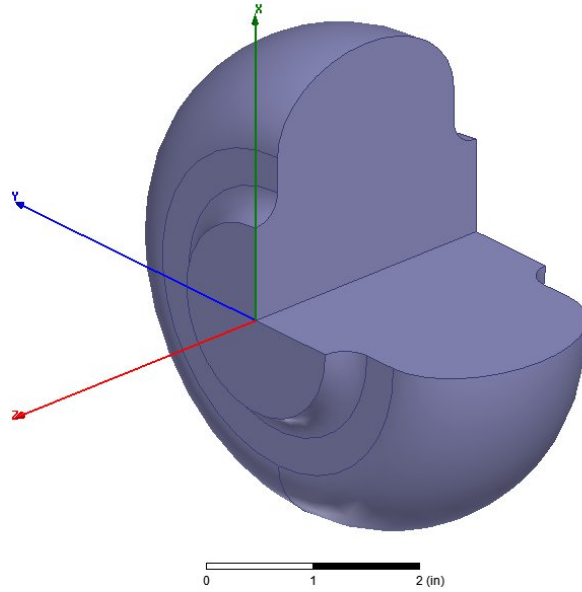


Figure 3-12: The vacuum region enclosed by a cell of the elliptical “low-loss” shape. One quarter of the cell is cut out to show the structure. The beam goes along the z -axis. The picture is taken from HFSS eigenmode simulations provided in Supplemental Materials [2].

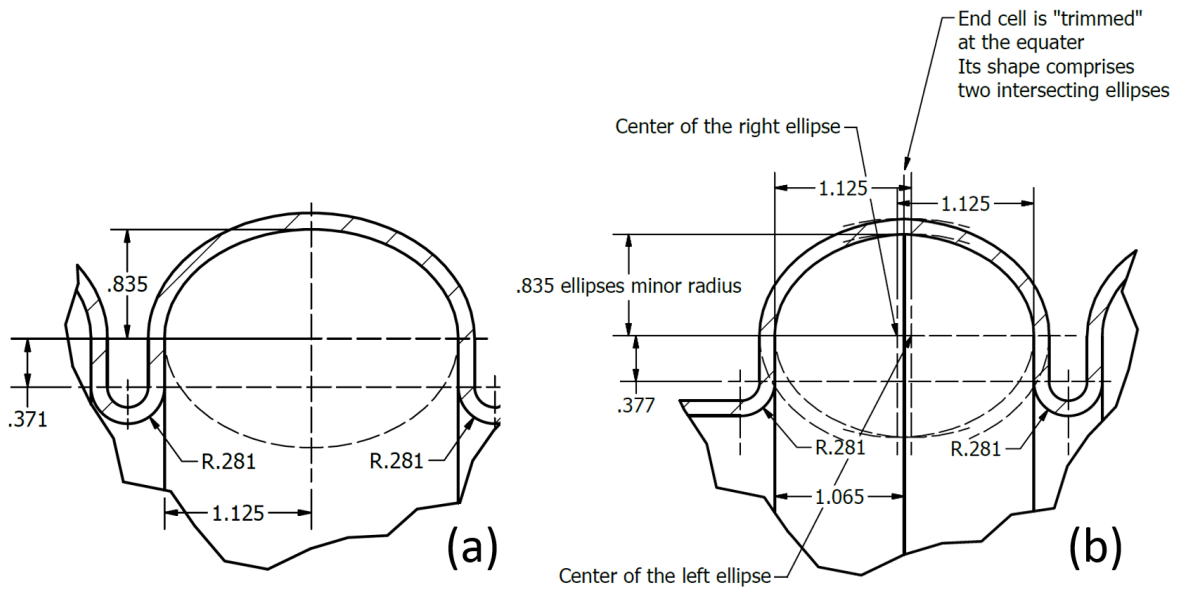


Figure 3-13: The dimensions of the elliptical cells of the “low-loss” shape [44], scaled to the frequency of 2.1 GHz. (a) an elliptical cell not located at the end of the 5-cell cavity. (b) a “trimmed” elliptical cell at the end of the 5-cell cavity.

the other cells, the gradient in them would be slightly different due to the different boundary condition. Therefore, the two end cells were designed shorter by about

2.1% of the fundamental wavelength than the other elliptical cells. The dimensions of the trimmed cells are shown in Figure 3-13, (b).

3.4 Design of the five-cell cavity

One important parameter of a multi-cell accelerating cavity is the phase advance of the accelerating mode over the length of one cell. In a 5-cell cavity, modes with phase advances of $\pi/5$, $2\pi/5$, $3\pi/5$, $4\pi/5$, and π are possible [31]. The π -mode is a natural choice for accelerating cavities operating in the standing-wave regime due to its high shunt impedance. Multi-cell superconducting cavities normally operate in the standing wave regime, hence, the π -mode is traditionally used for acceleration.

A sketch of the electric field profile in the π -mode is shown in Figure 3-14. The on-axis electric field flips direction over the time it takes a bunch to travel to between two cells. Thus, the bunch is being continuously accelerated. This resonance condition is satisfied if the length of each cell is chosen appropriately (Equation (3.2)).

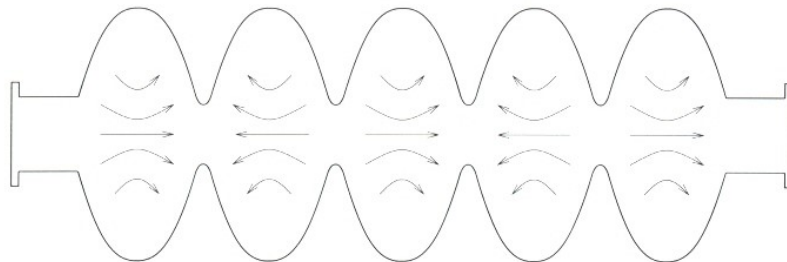


Figure 3-14: Sketch of the electric field lines of the π -mode of a 5-cell accelerating cavity [31].

In a 5-cell cavity of identical elliptical cells, each cell provides an equal amount of acceleration. However, replacing one of the elliptical cells with a PBG cell introduces some difficulties. For the same accelerating gradient, the surface magnetic field in a PBG cell is significantly higher than in a conventional cell due to the more sophisticated geometry. Using elliptically shaped rods in the first PBG layer only partially solves the problem.

If the five-cell cavity was designed to have a flat field profile, performance of the entire accelerator would be limited by the single PBG cell due to the higher probability of quench. Our goal was to design a cavity with equal probability of quench in every cell. This can be achieved by lowering the accelerating gradient (and so the surface magnetic field) in the PBG cell in such a way that the maximum values of the surface magnetic field are equal in each of five cells. Eigenmode simulations showed that lowering the accelerating gradient in the PBG cell to 60% of its value in the other cells ensures that the surface magnetic field is the same in every cell (see Supplemental Materials [2]).

An accelerating cavity can be viewed as a system of five connected oscillators with amplitudes of oscillations dependent on the resonant frequencies of the oscillators. By detuning the frequencies of the cells we can get the desired field profile with the amplitude of the electric field oscillations lowered in the PBG cell.

Achieving the desired accelerating gradient profile by randomly detuning different cavities is an impractical approach to solving the problem. Utilizing this approach would force us to explore all values of the 3-dimensional detuning vector $\Delta f = (\Delta f_1, \Delta f_2, \Delta f_3)$, where Δf_i is a frequency shift of the i -th cell (symmetry condition reduces the 5-dimensional detuning vector to three dimensions). While exploring different values of Δf , we have to make sure that the module of 5 cavities still matches the boundary conditions imposed by the beam pipe.

To simplify the process of tuning the cells to achieve the desired field profile, we used a circuit model for the accelerating module. It is commonly used to make the gradient profile flat by deforming cavities after fabrication [31]. For our design, however, we will use it for a different reason – to make the gradient profile intentionally not-flat, with the field amplitude in the PBG cell lowered to 60% of the maximum level.

3.4.1 Circuit model

In the circuit model, a set of cavities operating in the π -mode is represented by coupled LC-circuits shown in Figure 3-15. Each circuit includes a capacitance C_i and

an inductance L . The circuits are capacitively-coupled and the coupling strength is related to a capacitance C_k . The chain ends with capacitances C_b on both sides, representing the beam-pipe boundary condition. A current in each circuit represents the accelerating voltage (or accelerating gradient) in a corresponding cavity [31]. For our purposes, the desired dimensionless normalized accelerating voltages for the five cells were $V_{1,5} = 1$, $V_{2,4} = -1$, $V_3 = 0.6$.

We let the initial (or unperturbed) cell have a capacitance C_0 and an inductance L and assumed that its frequency of the π -mode $f_{\pi 0}$ is equal to the desired frequency (2.1 GHz). The frequency is adjusted by varying the radius of the cell or by slightly changing its length (so that the resonance condition 3.2 still applies). We used eigenmode simulations with periodic boundary conditions to relate a change in geometry to a change in frequency (see Supplemental Materials [3]). We then assumed that the frequencies of the cells are different from the desired frequency ($f_{\pi i} \neq f_{\pi 0}$) and instead correspond to different capacitances in the circuit model ($C_i \neq C_0$).

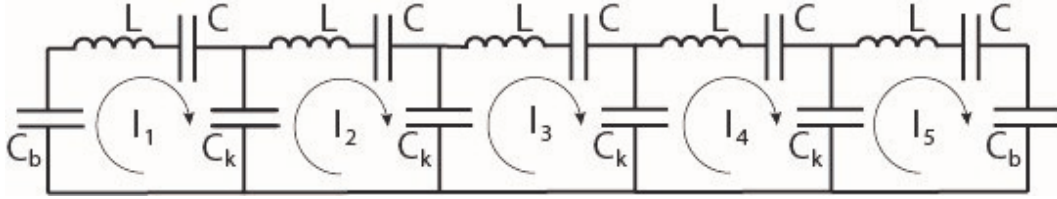


Figure 3-15: A circuit model representing the 5-cell accelerating cavity.

Using expressions for impedances of a capacitor and an inductor $1/(i\omega C)$ and $i\omega L$ respectively, we then wrote out Kirchhoff's equations for each circuit

$$\begin{aligned} \left(\frac{1}{i\omega C_b} + i\omega L \right) I_1 + \frac{1}{i\omega C_1} I_1 + \frac{1}{i\omega C_k} (I_1 - I_2) &= 0, \\ &\dots \\ \frac{1}{i\omega C_k} (I_i - I_{i-1}) + \left(\frac{1}{i\omega C_i} + i\omega L \right) I_i + \frac{1}{i\omega C_k} (I_i - I_{i+1}) &= 0, \text{ for } i = 2..4, \\ &\dots \\ \frac{1}{i\omega C_k} (I_5 - I_4) + \left(\frac{1}{i\omega C_5} + i\omega L \right) I_5 + \frac{1}{i\omega C_b} I_5 &= 0. \end{aligned}$$

We then defined the cell-to-cell coupling coefficient $k = C_0/C_k$ and the beam-pipe coefficient $\gamma = C_0/C_b$ and used the cell accelerating voltages V_i instead of the circuit currents I_i to rewrite the Equation (3.4.1) as a 5-dimensional eigenvector problem

$$\begin{bmatrix} C_0/C_1 + k + \gamma & -k & 0 & 0 & 0 \\ -k & C_0/C_2 + 2k & -k & 0 & 0 \\ 0 & -k & C_0/C_3 + 2k & -k & 0 \\ 0 & 0 & -k & C_0/C_4 + 2k & -k \\ 0 & 0 & 0 & -k & C_0/C_5 + k + \gamma \end{bmatrix} \begin{bmatrix} V_1 \\ V_2 \\ V_3 \\ V_4 \\ V_5 \end{bmatrix} = \left(\frac{f}{1/(2\pi\sqrt{LC_0})} \right)^2 \begin{bmatrix} V_1 \\ V_2 \\ V_3 \\ V_4 \\ V_5 \end{bmatrix},$$

where $i = 2..4$ and $f = \omega/2\pi$.

This equation is valid for the unperturbed case as well. By plugging values $C_i = C_0$ and $V_i = (-1)^{i+1}$ for the flat field profile of the π -mode, we get $\gamma = 2k$ and

$$f_{\pi 0} = \left(\frac{1}{2\pi\sqrt{LC_0}} \right) \sqrt{1 + 4k}. \quad (3.3)$$

Analogously, we get the following relation between a circuit frequency $f_{\pi i}$ and its capacitance C_i

$$f_{\pi i} = \left(\frac{1}{2\pi\sqrt{LC_i}} \right) \sqrt{1 + 4k}. \quad (3.4)$$

Thus, using Equation (3.4), we substituted C_0/C_i in the Equation (3.4.1) with the following easily computed values: $(f_{\pi i}/f_{\pi 0})^2$.

Next, we reversed the eigenvector problem to find elements of the matrix in the left side of Equation (3.4.1) for a given eigenvector \mathbf{V} . We also required the frequency

of the oscillations f to be equal to the designed value $f_{\pi 0}$. The solution is:

$$\begin{bmatrix} x_1 \\ x_2 \\ x_3 \\ x_4 \\ x_5 \end{bmatrix} = \begin{bmatrix} V_1 & 0 & 0 & 0 & 0 \\ 0 & V_2 & 0 & 0 & 0 \\ 0 & 0 & V_3 & 0 & 0 \\ 0 & 0 & 0 & V_4 & 0 \\ 0 & 0 & 0 & 0 & V_5 \end{bmatrix}^{-1} \begin{bmatrix} 1 & 1 & 0 & 0 & 0 \\ 1 & 2 & 1 & 0 & 0 \\ 0 & 1 & 2 & 1 & 0 \\ 0 & 0 & 1 & 2 & 1 \\ 0 & 0 & 0 & 1 & 1 \end{bmatrix} \begin{bmatrix} V_1 \\ V_2 \\ V_3 \\ V_4 \\ V_5 \end{bmatrix}, \quad (3.5)$$

where $i = 2..4$ and detuning values $x_i = [(f_{\pi i}/f_{\pi 0})^2 - 1]/k$ say how much the i -th cavity should be detuned.

The cell-to-cell coupling coefficient k depends on a particular geometry of the cells. It needs to be computed by running an eigenmode simulation that takes into account the exact shape of the cells (see Supplemental Materials [3]). In order to increase the accuracy and reduce the simulation time, we chose to run an auxiliary simulation with only two half-cells coupled together. The circuit model for such arrangement consists of two adjacent LC-circuits coupled capacitively to each other, similar to the circuits shown in Figure 3-15. We then slightly detuned one of the cells by changing its radius, which results in an un-even gradient profile with the coupled cells having different accelerating voltages $V_1 \neq V_2$. The voltages were then plugged in the corresponding Kirchoff's written out for the two-cell chain:

$$\begin{aligned} \frac{2}{i\omega C_k}(I_1 - I_2) + i\omega L I_1 + \frac{1}{i\omega C_1} I_1 &= 0 \\ \frac{2}{i\omega C_k}(I_2 - I_1) + i\omega L I_2 + \frac{1}{i\omega C_2} I_2 &= 0 \end{aligned}$$

to yield the value of the cell-to-cell coupling coefficient $k = 0.0145$. Values of k of a few hundredths are typical for multi-cell SRF cavities.

3.4.2 Incorporating the photonic band gap cell into the five-cell cavity

In the circuit model described above, we did not differentiate between elliptical cells and the PBG cell. We now take into account the fact that the geometry of the PBG cell is different from the elliptical cells. To apply to circuit model to the 5-cell cavity with the PBG cell, we introduce an adjustment factor for the PBG cell. The adjustment accounts for the fact that the accelerating field in the center of the PBG cell for a given field at the iris is slightly lower than that in an elliptical cell. Using HFSS eigenmode simulations, the adjustment factor α was found to be 0.845 (see Supplemental Materials [3]). This implies that for the desired profile of the normalized accelerating voltage $V_{1,5} = 1$, $V_{2,4} = -1$, $V_3 = 0.6$ we need to plug in the values $V_{1,5} = 1$, $V_{2,4} = -1$, $V_3 = 0.6/\alpha$ into the Equation (3.5). Frequency detunings from Equation (3.5) were then converted into a change in geometry of the elliptical cells and the PBG cell. The resulting accelerating gradient profile for the designed cavity is shown in Figure 3-16.

The cavity was planned to be tested at LANL with a CW beam current of 100 mA and a bunch repetition frequency of 100 MHz. This high beam current demanded relatively strong coupling to the accelerating mode, characterized by a low external Q-factor of the mode Q_{ext} . The optimal Q_{ext} was calculated to ensure that no RF power is reflected from the cavity back to the generator in the presence of the electron beam. To estimate the optimal Q_{ext} , we use the following formula derived using equations from [31]:

$$Q_{ext} = \frac{P_g}{I^2 \left(\frac{R}{Q}\right)}. \quad (3.6)$$

Here P_g is the power of the RF generator, I is the beam current and $\left(\frac{R}{Q}\right)$ is the parameter that quantifies how well the accelerating mode is coupled to the electron beam (see the section below). The value of $\left(\frac{R}{Q}\right)$ for the optimized geometry is 515 Ω . The planned generator power was 2 MW, supplied by a klystron. Plugging these numbers together with the value of the beam current of 100 mA gave us the value of

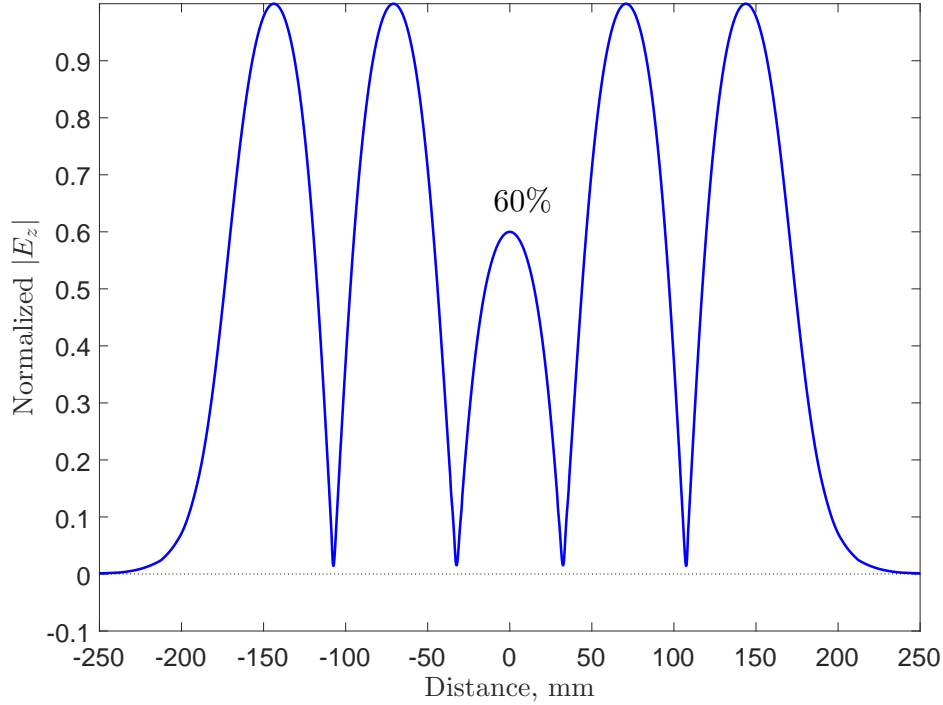


Figure 3-16: Design accelerating gradient profile, compared to the profile measured in the welded cavity using the bead-pulling method. The field in the center cell is intentionally lowered to ensure equal peak surface magnetic field in every cell.

the optimal $Q_{ext} = 3.9 \times 10^4$.

To provide such strong coupling to the accelerating mode, the PBG rod located closest to the FPC was removed, as can be seen in Figure 3-11. This approach was used earlier for the MIT traveling wave PBG structure [73]. Removing the rod in the SRF 5-cell cavity resulted in $Q_{ext} = 2 \times 10^4$. This rather strong coupling can be adjusted towards higher Q_{ext} with a waveguide stub, and gives us the flexibility to operate the structure in a wider range of power and beam current.

The geometry of the PBG cell was optimized to achieve better HOM damping in the 5-cell cavity. The optimization process consisted of choosing the parameters of the PBG cell such as the rounding radius of the iris, dimensions and angular positions of the waveguides. The design cell was incorporated in the 5-cell cavity, as described in the next section. The chosen parameters were then adjusted to achieve the best HOM damping in the 5-cell cavity. The ten most dangerous HOMs were identified,

and their Q-factors were calculated for a combination of the listed parameters (see Appendix A and additional files in Supplemental Materials [4]). In the process of optimization, a MATLAB code (see Supplemental Materials [5]) was used to generate a set of parameters that was sent to the eigenmode solver of the Ansys HFSS [71]. Q-factors of the HOMs were obtained and sent back to the MATLAB code. A “steepest descent” method was used to optimize the geometry. Final dimensions of the PBG cell are listed in Table 3.2.

3.4.3 Accelerating properties of the five-cell cavity with a photonic band gap cell

Table 3.3 compares the main accelerating properties of the 5-cell PBG cavity to the 5-cell cavity with only elliptical cells [44]. The first compared quantity $\frac{R}{Q}$ is defined for the monopole modes as the following ratio

$$\left(\frac{R}{Q}\right) = \frac{V_{\parallel}^2}{\omega U}, \quad (3.7)$$

where V_{\parallel} is the effective longitudinal voltage defined earlier in Equation (2.5), $\omega = 2\pi f$ is the angular frequency of the mode and U is the total energy stored in the electromagnetic fields of the mode. The letter R in the ratio $\frac{R}{Q}$ refers to shunt impedance - a quantity that characterizes the losses in a cavity, and the letter Q refers to the unloaded Q-factor. The quantity $\frac{R}{Q}$, however, is more fundamental than shunt impedance itself, and is used to assess accelerating properties of RF cavities. Higher $\frac{R}{Q}$ means that more acceleration can be achieved for the same RF energy, and maximizing $\frac{R}{Q}$ is one of the major priorities of any accelerator design. As can be seen in Table 3.3, $\frac{R}{Q}$ of the designed 5-cell cavity is only slightly lower than that of the cavity from [44].

The second compared quantity, the geometry constant G , is defined in [31] as

$$G = \frac{\omega\mu_0 \int_V |H|^2 dv}{\int_S |H|^2 ds}, \quad (3.8)$$

Table 3.3: Accelerating properties of the 5-cell cavity with a PBG cell compared to the accelerating properties of the cavity with 5 elliptical “low-loss” cells from [44]. The values for the PBG cavity were obtained using eigenmode simulations provided in Supplemental Materials [2].

	5-cell cavity with a PBG cell	JLAB’s 5 elliptical cells cavity
Frequency f_0	2100 MHz	748.5 MHz
$\left(\frac{R}{Q}\right) \frac{R}{Q}$	515 Ω	525 Ω
Geometry constant G	265 Ω	276 Ω
Peak surface electric field ratio E_{peak}/E_{acc}	2.65	2.50
Peak surface magnetic field ratio B_{peak}/E_{acc}	4.48 $\frac{mT}{MV}$	4.27 $\frac{mT}{MV}$

where $|H|$ is the magnitude of the magnetic field. For a given surface resistance R_s , G defines the unloaded Q-factor of the cavity

$$Q_0 = G/R_s. \quad (3.9)$$

The geometry constant for the designed cavity is nearly the same as for the 5-cell elliptical cavity, as can be seen in Table 3.3.

From Table 3.3 we can conclude that the main accelerating parameters of the designed 5-cell PBG cavity are only slightly worse than those of the design with elliptical cells only. Although a single PBG cell by itself has the ratio of the surface magnetic field to the accelerating gradient about twice higher than the elliptical cells have [92], corresponding ratio for the designed 5-cell cavity is close to the value for the “low-loss” geometry because of the uneven gradient profile 3-16. Indeed, the difference in the peak surface magnetic field is within a few percent, as shown in Table 3.3.

The designed 5-cell cavity has two advantages to compensate for the slight decrease in accelerating properties. The first advantage is the efficient HOM damping (see the next Section). The second advantage is the increased real estate gradient, defined as the total amount of acceleration divided by the total length of the accelerator.

The second advantage comes from the fact that, unlike traditional multi-cell SRF

cavities [44, 65], the 5-cell cavity with a PBG cell does not need waveguides on the beam-pipe sections of the cavity. Attaching couplers straight to accelerating cells is not desirable in the traditional designs due to the azimuthal asymmetry that couplers introduce in the accelerating mode, and due to the increased surface fields at the region where the couplers are attached. The PBG cell eliminates both problems. Indeed, regardless of the number of waveguides the accelerating mode in the PBG cell has a six-fold azimuthal symmetry, and the fields at the location of the waveguides are reduced by the PBG lattice. The real estate gradient can, therefore, be as much as 10% higher. The exact number depends on the cavity packing factor.

3.5 Simulations of higher order modes

Simulations presented in this section were used to optimize positions and dimensions of the HOM couplers and the FPC for the strongest HOM damping. A MATLAB routine was used together with the Ansys HFSS [71] simulations to tune individual parameters such as positions and dimensions of the coupler waveguides and outside dimensions of the PBG cell (see Appendix A and additional files in Supplemental Materials [4] and Supplemental Materials [5]). Simulation data presented below applies to the final optimized geometry.

We studied HOMs paying particular attention to the monopole and the dipole modes with frequencies below the corresponding beam pipe's cutoffs. Modes with higher order angular variation were not considered because their transverse impact on the beam was smaller. Modes with frequencies above the beam pipe's cutoff were considered less dangerous as they propagated through the beam pipe and did not build up in the cavity.

To classify HOMs in the cavity, we used two symmetry planes: XY and XZ . Here Z is the axis along the beam line and the X axis is parallel to the FPC waveguide, as shown in Figure 3-4. All the dipole modes can be classified as either X -modes (\mathbf{E} field is in the XZ plane) or Y -modes (\mathbf{E} field is perpendicular to the XZ plane).

We used two different approaches to studying HOMs. First, wakefield simulations

were performed to identify the most dangerous dipole modes and compute the corresponding deflecting voltages induced by a single bunch. Next, eigenmode simulations were used to verify the results obtained from the wakefield simulations and to calculate the external Q-factors for the modes. The monopole modes were also studied in the eigenmode approach. The wakefield and the eigenmode simulations are described in Appendix A and the corresponding files are provided in Supplemental Materials [6] and Supplemental Materials [4].

3.5.1 Wakefield solver

CST Particle Studio [70] was used to analyze the dipole HOMs in the designed five-cell cavity. In particular, the wakefield solver was employed to simulate interactions of the HOMs with the electron beam in the designed five-cell cavity (see Appendix A and additional files in Supplemental Materials [6]). The wakefield solver computes the fields excited in the structure by a source charge and simulates how the fields can affect a test charge entering the cavity some time after the source charge.

We calculated the effective deflecting voltages $V_{\perp n}$ defined in Equation (2.6). The deflecting voltages describe how the n -th dipole mode affects the test charge travelling offset from the axis. In order to find the deflecting voltages, we first computed the transverse wake potential $\mathbf{w}_{\perp}(\mathbf{r}, \mathbf{r}_1, s)$ and the transverse wake impedance $\mathbf{Z}_{\perp}(\mathbf{r}, \mathbf{r}_1, \omega)$, defined in Equations 2.2 and 2.4, respectively. Here \mathbf{r} is the transverse displacement of the source charge, \mathbf{r}_1 is the transverse displacement of the test charge, and s is the distance between the charges. The wakefield simulations were performed for the cases $\mathbf{r} = \mathbf{r}_1 = x\hat{x}$ and $\mathbf{r} = \mathbf{r}_1 = x\hat{y}$. The calculated transverse wake impedance Z_{\perp} for both cases (X or Y displacement) is shown in Figure 3-17.

As was demonstrated in Chapter 2, the deflecting voltage for a dipole mode is proportional to the integrated area under the corresponding peak of the transverse wake impedance. Since we are only interested in the deflecting voltages, the energy decay time can be chosen independently as it only affects the width of a peak, but not the area. As long as the wake impedance peaks do not overlap, we can save computational time by decreasing the energy decay time and widening the peaks.

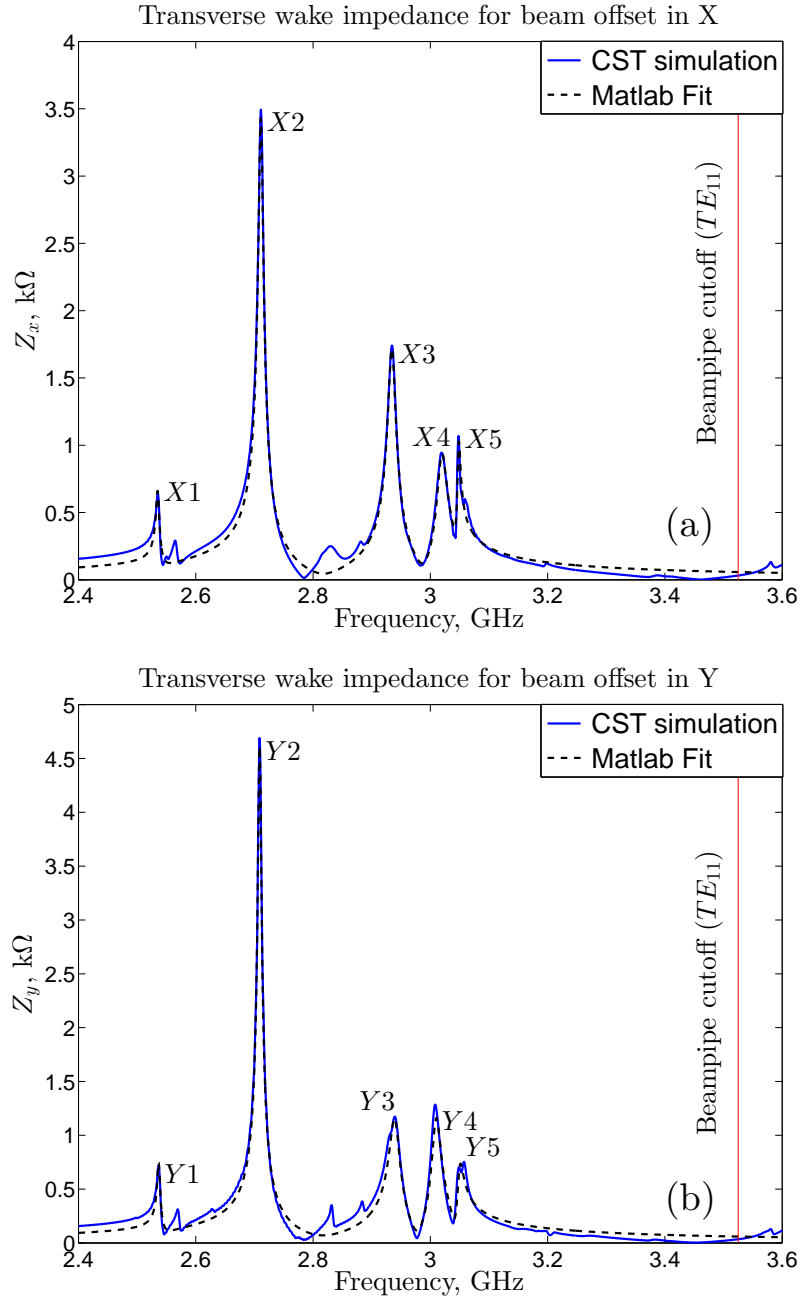


Figure 3-17: Transverse impedance calculated by CST Particle Studio for the electron beam displaced in X direction (a) and Y direction (b). 10 most dangerous modes correspond to the biggest peaks in impedance. Analytical shapes for the peaks were fitted using a MATLAB algorithm presented in Supplemental Materials [7]. Input data for the Figure is provided in Supplemental Materials [6].

For that reason, a lossy material was used for the cavity walls in addition to the waveguide ports (see Appendix A).

In Figure 3-17, 10 peaks can be seen in wake simulations that correspond to the 10 most dangerous dipole modes with the highest V_{\perp} . These modes were labeled as $X_1 - X_5$ and $Y_1 - Y_5$ and were used for the cavity optimization. To calculate the deflecting voltages, we fitted the known analytical shapes for wake impedance peaks (see Chapter 2) with variable complex phases (the fitting algorithm is described in Supplemental Materials [7]). The amplitude and phase of each analytical peak were adjusted so that the analytical curve for the wake impedance matches the simulation very closely (Figure 3-17). The calculated voltages, normalized over the source charge q and the offset ρ , are listed in the last column of Table 3.4.

3.5.2 Eigenmode solver

We simulated HOMs with the eigenmode solver of the Ansys HFSS (see Appendix A and additional files in Supplemental Materials [4]). Similar to the wakefield approach, the eigenmode approach can be used to calculate voltages induced by a single bunch, defined in Equations 2.5 and 2.6. The voltages can be related to the shunt impedances of the modes [31]:

$$\frac{|V_{||n}|}{q} = \pi f_n \left(\frac{R}{Q} \right)_n \quad (3.10)$$

for the n -th monopole mode, and

$$\frac{|V_{\perp n}|}{q\rho} = \frac{2\pi^2 f_n^2}{c} \left(\frac{R}{Q} \right)_n^d \quad (3.11)$$

for the n -th dipole mode. Here f_n is the frequency of the mode, q is the charge of the exciting bunch, ρ is the offset from the axis, $(R/Q)_n$ is the shunt impedance of a monopole mode and $(R/Q)_n^d$ is the shunt impedance of a dipole mode. Both monopole and dipole shunt impedances are measured in Ohms in agreement with [31].

For each HOM, an eigenmode simulation was set up to calculate the shunt impedance and the external Q-factor. The complex geometry of the PBG cell supports a large number of unimportant modes trapped in the lattice of rods with very small fields at the center of the cell. While not interacting strongly with the beam, those modes

can unnecessarily increase computational time. For that reason, only modes with $R/Q > 1\Omega$ (for both monopoles and dipoles) were studied in details.

Table 3.4: Simulation results for the dipole modes with $(R/Q)^d > 1\Omega$.

f , GHz	Q_{ext}	$(R/Q)^d, \Omega$	$ V_{\perp} /(q\rho)$, V/(nC mm) (eigenmode)	$ V_{\perp} /(q\rho)$, V/(nC mm) (wakefield)
X-modes				
2.538 (X_1)	2.7×10^3	7.7	3.2	3.2
2.567	1.5×10^3	3.6	1.6	
2.713 (X_2)	7.5×10^2	58.4	28.3	29.4
2.713	1.3×10^2	9.3	4.5	
2.831	1.0×10^2	8.5	4.5	
2.884	6.8×10^2	1.1	0.6	
2.936 (X_3)	3.0×10^2	42.1	23.8	22.7
2.962	1.8×10^2	2.1	1.2	
3.020 (X_4)	2.0×10^2	27.6	16.6	15.0
3.047 (X_5)	1.6×10^4	5.7	3.5	4.1
3.060	4.8×10^2	2.4	1.5	
Y-modes				
2.539 (Y_1)	2.7×10^3	8.8	3.7	3.3
2.571	2.7×10^4	3.0	1.3	
2.710	5.4×10^2	8.9	4.3	
2.711 (Y_2)	9.4×10^2	57.7	27.9	29.2
2.825	3.7×10^1	7.2	3.8	
2.887	5.4×10^3	1.3	0.7	
2.940 (Y_3)	2.6×10^2	35.3	20.1	20.1
2.995	1.4×10^2	3.0	1.7	
3.014 (Y_4)	1.9×10^2	26.6	15.9	17.7
3.048 (Y_5)	2.2×10^3	5.8	3.6	6.1
3.059	7.3×10^2	3.4	2.1	

In order to calculate a dipole mode's shunt impedance $(R/Q)^d$, the beam trajectory was shifted off-axis in either the X or the Y direction by a distance equal to one beam pipe's radius. To calculate the external quality factors, all three waveguides were covered with a PML. The calculated shunt impedances and Q_{ext} for the dipole and the monopole modes (with shunt impedance exceeding 1Ω) are presented on Figure 3-18 and Tables 3.4 and 3.5. Tables 3.4 and 3.5 also list the estimated voltages induced by a single bunch and compare them to the voltages obtained in the wakefield simulations for the 10 dangerous modes. Good agreement between the two

Table 3.5: Simulation results for the monopole modes with $R/Q > 1\Omega$.

Freq, GHz	Q_{ext}	$R/Q, \Omega$	$ V_{ n} /q, \text{V/nC}$
2.025 ($\pi/5$)	3.4×10^3	10.9	69.3
2.071 ($3\pi/5$)	1.1×10^4	1.9	12.7
2.100 (π)	2.0×10^4	515	3400
3.198	3.2×10^3	35.7	359.1
3.663	1.7×10^5	12.5	143.5
3.668	1.0×10^4	36.6	421.6
3.813	3.8×10^5	64.5	773.1
3.814	8.6×10^3	18.2	217.8
4.540	1.1×10^3	1.5	20.9

independent approaches shows the reliability of the obtained results.

We were particularly interested in the Q_{ext} for the dipole modes as they are the major cause of the beam break-up (BBU) instability. As can be seen in Table 3.4, most of the dipole modes have Q_{ext} in the range of $10^2 - 10^3$. Only two modes ($f = 3.047$ GHz and $f = 2.571$ GHz) with relatively low shunt impedances of 5.7Ω and 3.0Ω have higher Q_{ext} , 1.6×10^4 and 2.7×10^4 , respectively. This can be explained by the fact that the longitudinal component of the electric field E_z for these two modes is going through zero in the middle of the PBG cell. Although some asymmetry due to fabrication errors should lower the Q_{ext} for such modes, asymmetrical tuning could be used to bring Q_{ext} even lower, if necessary.

The BBU figure of merit $(R/Q)_n Q_n f_n$ is plotted in Figure 3-19 for the PBG cavity, as well as for the 9-cell TESLA cavity which employs coaxial HOM couplers [41, 65]. Loaded Q factors were substituted with the calculated values of Q_{ext} for all of the plotted modes due to negligible losses in superconducting walls. It can be seen that the highest value of $(R/Q)_n Q_n f_n$ for the dipole modes below a beam pipe cutoff is much lower for the PBG cavity than for the TESLA cavity. This means that the PBG cavity has the potential to support much higher beam currents due to improved HOM damping.

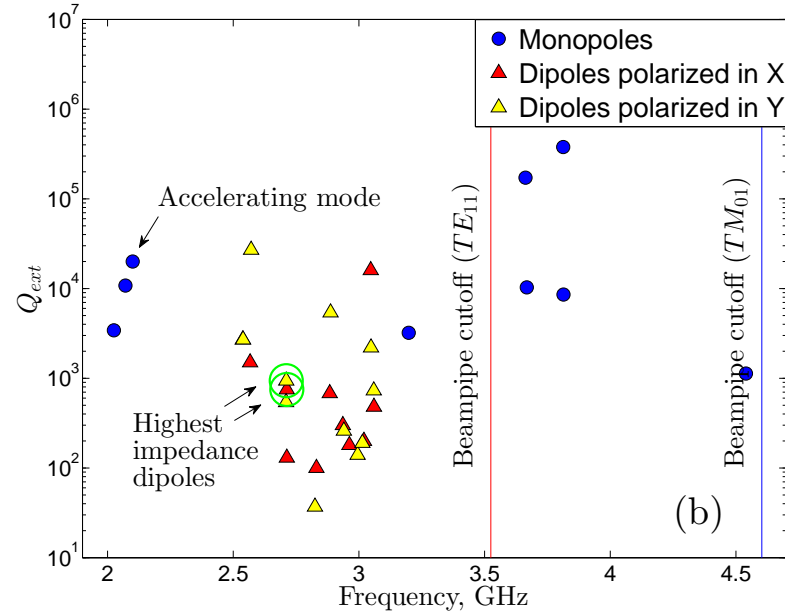
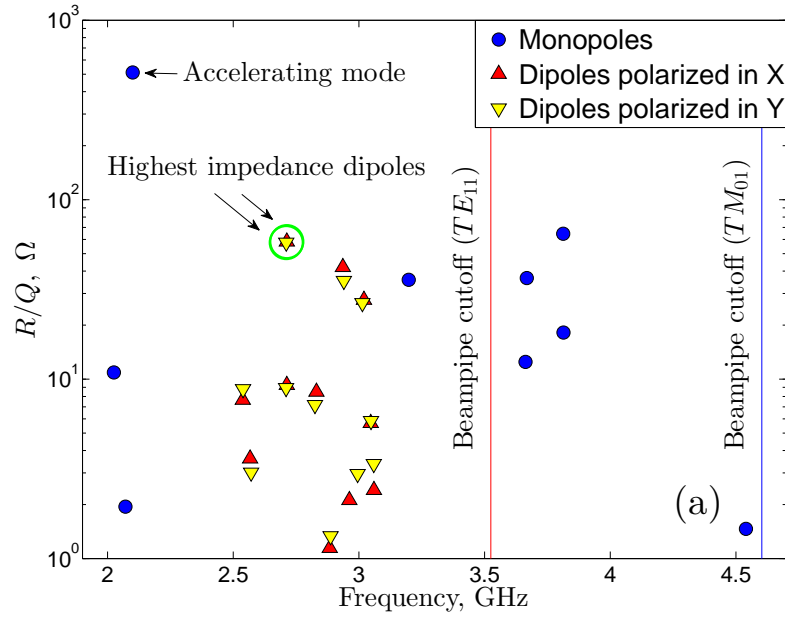


Figure 3-18: Shunt impedances (a) and external Q factors (b) for monopoles and dipoles in the 5-cell PBG cavity obtained in HFSS eigenmode simulations described in Appendix A and Supplemental Materials [4]. Only modes with $R/Q \geq 1\Omega$ are shown. Input data for the Figure is provided in Tables 3.4 and 3.5.

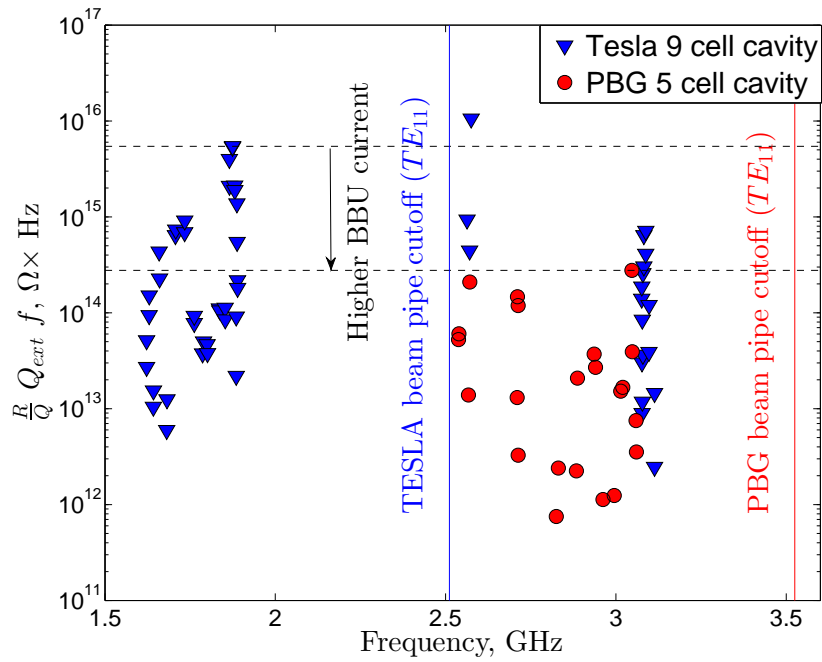


Figure 3-19: BBU figure of merit $(R/Q)Q_{ext}f$ for the dipole modes for two different cavities: the 9-cell TESLA and the 5-cell PBG. Dipole shunt impedance is in units of Ohms. Simulation data for the TESLA cavity is from Ref [41, 65]. Simulation data for the PBG cavity is taken from Tables 3.4 and 3.5.

Chapter 4

Fabrication and tuning of the niobium five-cell cavity

This Chapter describes fabrication and tuning of the five-cell cavity with the PBG coupler cell. SRF cavities are traditionally fabricated of high purity niobium, which is a highly workable superconducting metal.

Often, prior to fabrication of a niobium SRF cavity, its copper prototype is made (see, for example, [44]). Following this practice, we decided to fabricate a copper prototype of the designed cavity for two reasons. The first reason is to demonstrate the novel fabrication and tuning required for the multi-cell structure with the PBG coupling cell. The fabrication and tuning process used for the copper prototype was later almost exactly repeated for the niobium cavity, with the dices and the tools reused. The second reason to have the copper prototype is to analyze HOM damping in the copper cavity by measuring external quality factors Q_{ext} for the most dangerous HOMs. The HOM measurements are described in Chapter 5.

Since the fabrication process was mostly the same for the copper prototype and the niobium cavity, the steps are described for the niobium cavity only. Where the fabrication steps were different, the procedure used for the copper prototype is described separately. Photographs of the fabrication steps feature both cavities.

The process of manufacturing the cavity consisted of two steps. First, the parts of the cavity were fabricated and welded using electron beam welding. The parts of

the five-cell cavity are shown schematically in Figure 4-1. Then, the cavity needed to be tuned to have the desired frequency close to 2.1 GHz and the desired accelerating gradient profile (shown in Figure 3-16). The tuning process is described below and consisted of trimming the half-cells at the equator, as shown in Figure 4-1 (right).

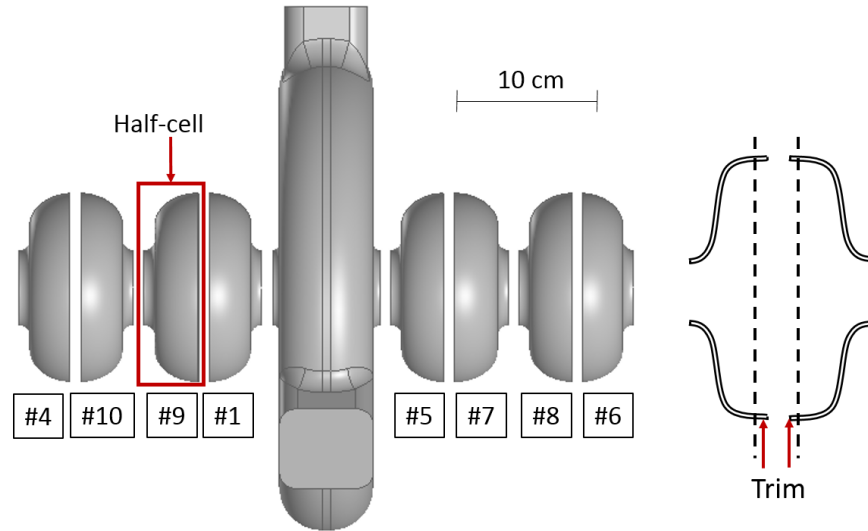


Figure 4-1: Parts of the 5-cell cavity before trim-tuning. All of the elliptical half-cells are trimmed at the equator, where an additional 0.1 inch of material was left on each side for tuning.

4.1 Fabrication of the cavity components

To fabricate the elliptical cells, we followed procedures used at Niowave Inc. for fabrication of conventional multi-cell SRF cavities. The halves of the elliptical cells (half-cells) were fabricated separately. The half-cells were stamped from sheets of high purity niobium with $RRR \geq 250$. As shown in Figure 4-1, a total of eight half-cells were needed for the cavity. In order to have two spares, ten half-cells were fabricated and numbered from 1 to 10.

Each elliptical half-cell was machined with an extra 0.1 inch of material at the equator to allow for future trim-tuning. The neighboring half-cells 7 and 8, as well as 9 and 10, were welded together at the irises prior to tuning to minimize the effect

of weld shrinkage on the gradient profile. Welded half-cells formed “dumbbells”, as shown in Figure 4-2.



Figure 4-2: Two “dumbbells” used on the opposite sides of the five-cell cavity. Each dumbbells formed by two halves of the elliptical cells welded together at the irises.

The two walls of the PBG cell were stamped from niobium sheets ($RRR \geq 250$) similar to the elliptical cells. The stamping process required all edges of the walls to be rounded, hence the design was adjusted to facilitate the fabrication process. The two walls were welded together at the equator and the holes were made in the walls to fit the PBG rods. The rods were fabricated separately from ingot niobium. The rods were fitted in the holes, and electron-beam welded to the walls of the PBG cell. Finally, waveguide flanges were machined and welded to the cell. Photographs of the PBG cell between the described steps are shown in Figure 4-3.

4.2 Tuning and assembling the cavity

Tuning and assembling of the cavity were done in parallel. The goal of the tuning was to make the frequency close to 2.1 GHz and, more importantly, to make the accelerating gradient profile close to the designed profile (Figure 3-16). For the purposes of the planned cryogenic tests it was not necessary to tune the cavity to exactly 2.100 GHz, therefore, the center (PBG) cell was not tuned. Nevertheless, the frequency of the cavity under vacuum and at the cryogenic temperature was 2.1062 GHz measured

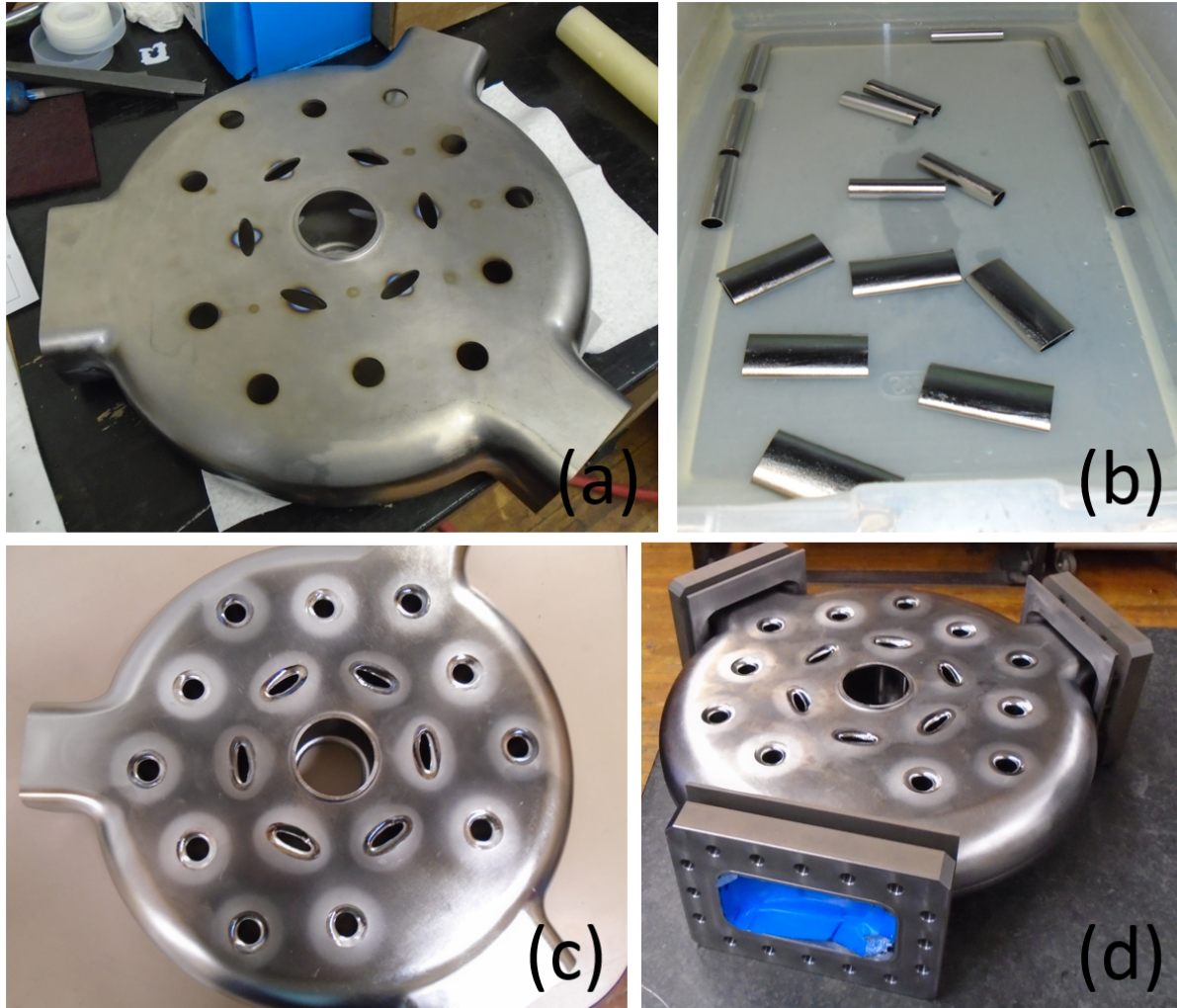


Figure 4-3: (a) Holes for the PBG rods were made in the walls of the PBG cell. (b) The PBG rods were cleaned in ultra-pure water. (c) The rods were welded to the walls of the cell. (d) Waveguide flanges were made and welded to the cell.

in high-gradient tests (see Chapter 6), within 0.5% of the design.

It has to be noted, however, that in a multi-cavity linac all the structures must be tuned to the same frequency. Therefore, a few different mechanisms of tuning have been proposed for the PBG cell, including pushing on the inside of the PBG rods. A cavity tuner which stresses and compresses the full cavity to tune the frequency of the structure will affect the field flatness because the elliptical cells will tune more easily than the center PBG cell. Nevertheless, such a scheme is expected to allow sufficient tuning to synchronize a multi-cavity linac with little cost in terms of field

flatness (see below).

To obtain the gradient profile shown in Figure 3-16, we used the circuit model described in Chapter 3. Since we did not plan to tune the PBG cell, the first step in using the model was to identify the frequency of the π -mode in the fabricated cell. To excite the π mode, we needed to have the appropriate boundary conditions on the borders between the cells (at the irises) on both sides of the PBG cell. The boundary condition for the π -mode requires the electric field at the iris to be perpendicular to the z -axis, as shown in Figure 3-14 (the “H-boundary”). To construct the “H-boundary”, the PBG cell was stacked with two elliptical half-cells and pressed with four long screws to provide a good electrical contact between the cells as shown in Figure 4-4. The half-cells were terminated with two metal plates so that the electric field is parallel to the z -axis in the center of the elliptical cells, matching the profile of the π -mode.

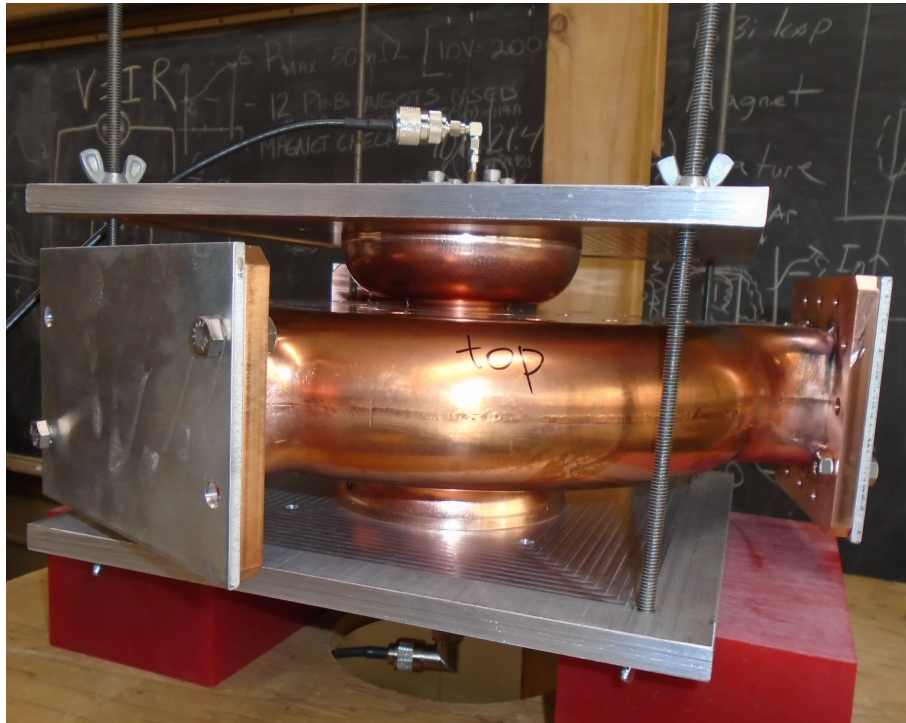


Figure 4-4: The PBG cell is stacked with two half-cells, terminated with metal plates to excite the π -mode (the copper structure is shown in the picture rather than the niobium structure due to the better photograph).

The π -mode was then excited in such 3-cell structure by two SMA antennas stick-

ing through the metal plates, as shown in Figures 4-4 and 4-5. The frequency of the π -mode in the 3-cell structure was measured with a network analyzer.

The accelerating gradient profile was measured using the bead-pull technique (described, for example, in [94]). The bead-pull setup consisted of a spherical metal bead 3.2 mm in diameter on a thin polyester thread, pulled by a stepper motor. The motor was controlled by a step-function generator to precisely map the location of the bead. Deviation of the phase of the mode was measured as the bead was traveling through the structure. The bead could be viewed as a small perturbation to the geometry. In such setup, the frequency shift caused by the perturbation is proportional to the square of the magnitude of the electric fields at the location of the bead. The accelerating gradient profile was reconstructed from the phase deviation of the π -mode. The initial gradient profile in an untuned 3-cell setup is shown in Figure 4-6.

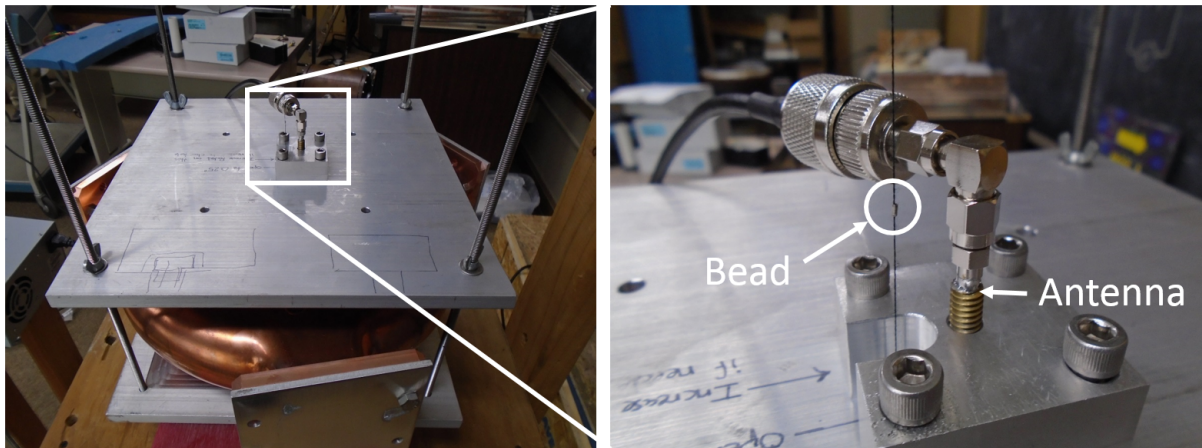


Figure 4-5: The bead-pull setup for the electric field measurement. The bead is being pulled by a string attached to a small motor. The copper structure is shown in the picture rather than the niobium structure due to the better photograph.

The accelerating gradient profile in the 3-cell setup gave us three voltages $V_{1,2,3}$ that could be plugged into the corresponding 3-cell circuit model. For the profile shown in Figure 4-6, the normalized voltages were 0.98, -0.83, 1, respectively. Unlike the 5-cell model from Figure 3-15, the 3-cell model does not have the beam-pipe boundaries at the end, and instead uses the “E-boundary” condition representing the metal plates at the two sides. An auxiliary bead-pull measurement was also done with just the two half-cells stacked together, without the PBG cell. This gave us

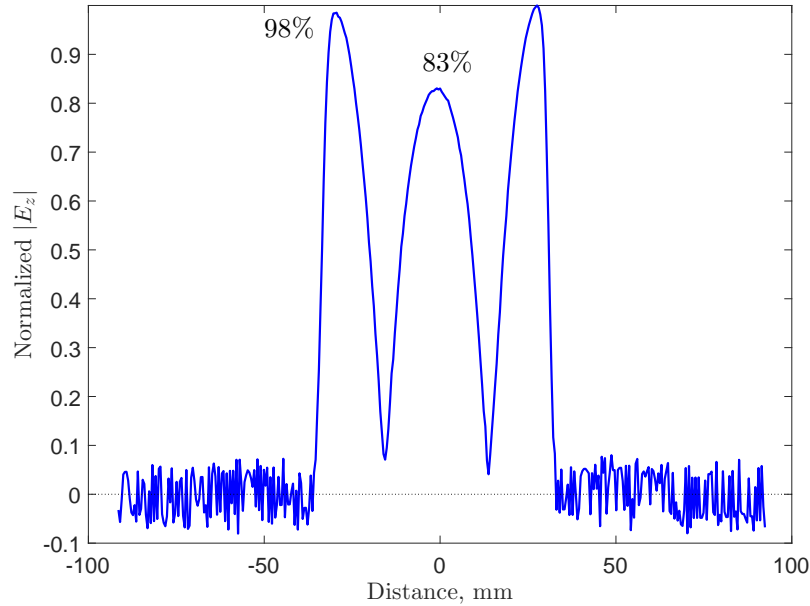


Figure 4-6: The initial gradient profile for the π -mode, excited in a 3-cell setup of untuned niobium cells from Figure 4-4.

enough information to obtain the eigenfrequency of the π mode in the PBG cell.

Once the eigenfrequency of the PBG cell was known, the desired frequency of the π -mode in the 5-cell assembly was calculated using the circuit model (Chapter 3) and a MATLAB code provided in Supplemental Materials [8]. We then continued with the procedure described in Chapter 3 and related the desired frequencies of the elliptical cells to the amounts of trimming. In that calculation, we accounted for the estimated future weld shrinkage due to the electron-beam welding (about 0.014 inch on each welded surface).

The cells were trimmed to the calculated amount in a few steps. Using the same bead-pull technique, the gradient profile was measured for the entire 5-cell assembly between the trimming steps to make sure that the gradient profile was getting closer to the design curve (Figure 3-16). The final trimming of the cells relative to the fabricated length (offset 0.1 inches from the design length) are listed in Table 4.1. The cells are listed in the order they were welded in the actual cavity (Figure 4-1).

As mentioned above, the process of fabrication and tuning discussed up to this point was applied to both the copper prototype and the niobium cavity. However,

Table 4.1: Amounts trimmed off the equators of the half-cells.

Half-cell number	Amounts trimmed off the equators of the half-cells, inches
4	159.5/1000
10	116.5/1000
9	71.5/1000
1	113.5/1000
PBG cell	not trimmed
5	113.5/1000
7	74.5/1000
8	119.5/1000
6	159.5/1000

the welding was done differently for the two structures.

Since the copper prototype cavity was not meant to be used in a cryogenic experiment, it was decided to not do expensive electron-beam welding for the cavity. Instead, an attempt was made to TIG-weld the cells of the copper cavity together. The attempt was not successful, leaving small air gaps between the cells. The gaps made it not possible for the electric currents to flow freely between the cells, hence, the HOM spectrum was changed. It was therefore decided to not use the copper cavity for HOM measurements, as was originally planned. The most important measurements described in Chapter 5 were made using the same niobium cavity that underwent the cryogenic testing.

For the niobium cavity, the cells were successfully electron-beam welded to form the complete five-cell structure, shown in Figure 4-7. The gradient profile after the final weld was within 5% of the design and no additional tuning was required. Nevertheless, the elliptical cells were squeezed a little in the longitudinal direction to even-out the profile. Squeezing was done with specially made aluminum plates. The final accelerating gradient profile is shown as a solid red line in Figure 4-8.

The niobium cavity's Q-factor measured at a room temperature was $Q_{300\text{ K}} = 7300$. Assuming the niobium bulk conductivity is equal to its theoretical value of $\sigma = 6.58 \times 10^6 \Omega^{-1} m^{-1}$ and using the Equation 3.9, we obtained the geometry constant $G = 259$ which is in good agreement with the predicted value of 265 (Table 3.3). The

agreement indicates that the geometry of the fabricated cavity was close to the design geometry.

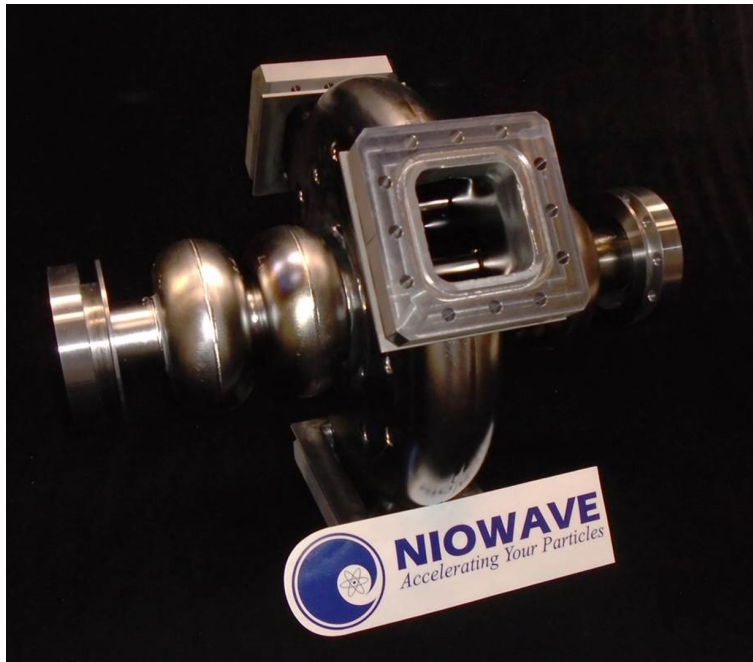


Figure 4-7: The niobium 5-cell cavity after all the parts were electron-beam welded.

4.3 Preparation to cryogenic tests

The niobium cavity underwent extra surface treatment to prepare for cryogenic tests. Surface preparation is typically done in SRF cavities to mitigate quenching at low RF power and to increase the unloaded Q-factor, as was discussed in Chapter 2. The cavity was chemically treated using buffered chemical polish (BCP) solution of HF, HNO₃, and H₃PO₄ in proportion 1:1:2. The solution was circulated inside the cavity for the time needed to remove 150 μm thick layer off the inner niobium surface, and then high-pressure rinsed with ultrapure water. The polishing setup at Niowave Inc. is shown in Figure 4-9.

In a typical "vertical" cryogenic test, an SRF cavity is lowered into a cryostat filled with liquid helium and tested at a superconducting temperature without an electron beam. A relatively low RF power (a few hundred Watts) is needed to achieve high

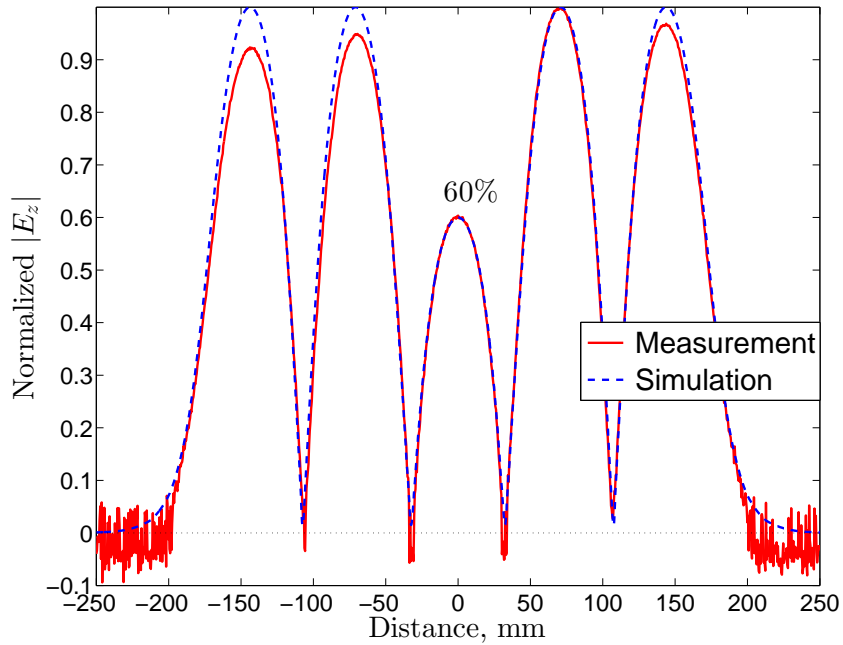


Figure 4-8: Accelerating gradient profile measured in the welded niobium cavity using the bead-pulling method, compared to the design profile. The field in the center cell is intentionally lowered to ensure equal peak surface magnetic field in every cell.

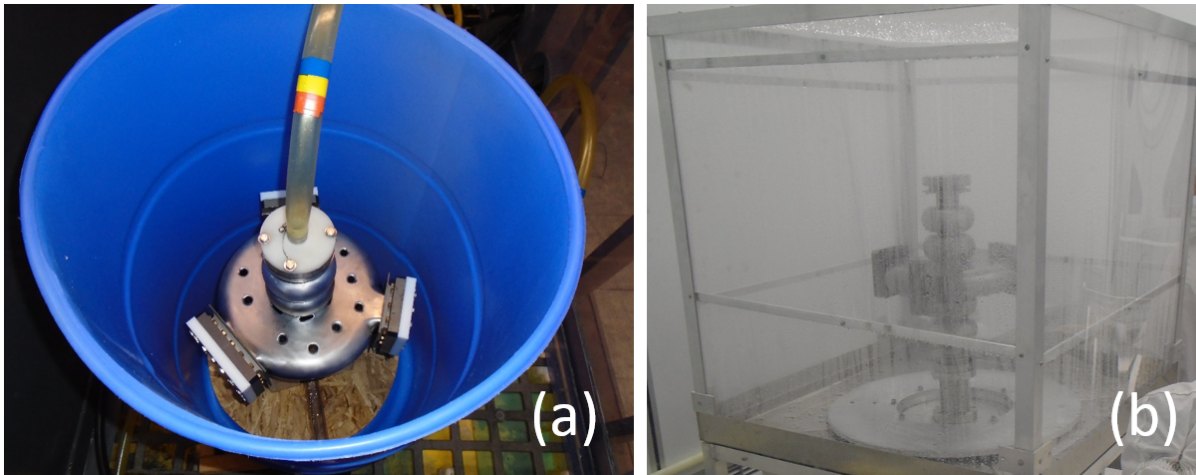


Figure 4-9: (a) The niobium cavity just before the buffered chemical polish treatment. The cavity is filled through the pipe with a mix of HF, HNO₃, and H₃PO₄. (b) The cavity is undergoing a high-pressure rinsing cycle after the chemical treatment.

fields in the cavity with no beam. For such test, the needed external Q-factor of the operating mode should be close to the cavity's unloaded Q to avoid unnecessary reflection back to the power generator. Therefore, a much weaker coupling is needed

in the experiment than is provided by the FPC. Hence, for the vertical testing the coupling to the mode was done via specially made antennas in the beam-pipe. The three waveguides needed to be covered with metal plates to prevent liquid helium from filling the cavity.

One way to cover the waveguide ports for a high gradient test is to use an indium gasket for both a vacuum and an RF seal (as in, for example, [95]). However, indium gaskets have the disadvantage of leaving residue on RF flanges. Therefore, a different idea was implemented with vacuum and RF seals provided by different parts of the joint; clamped niobium-to-niobium contact provides an RF seal, as in [96], and a “diamond” aluminum gasket provides a vacuum seal, as in [97]. The cross-section of the joint is shown in Figure 4-10.

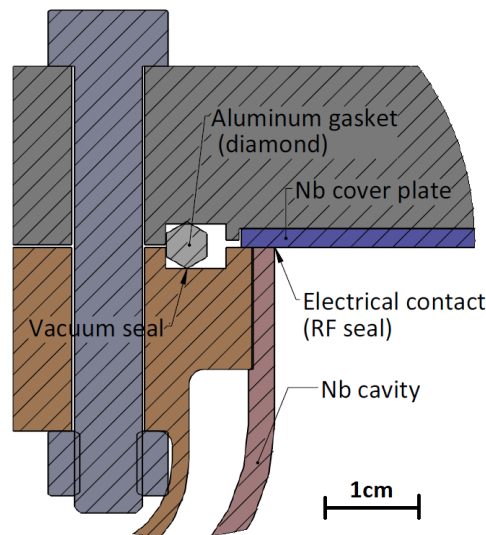


Figure 4-10: Structure of the FPC waveguide cover for the niobium cavity, made as preparation for cryogenic tests. Niobium-to-niobium contact provides an RF seal, while a “diamond” gasket provides a vacuum seal.

After a series of initial cryogenic tests (see Chapter 6), the cavity was also welded into a titanium helium vessel, shown in Figure 4-11 in gray. The helium vessel serves as a “bath” that is filled with liquid helium to keep the cavity at a superconducting temperature, as is schematically shown in Figure 1-5. The addition of the helium vessel brought the cavity a step closer towards an accelerator-ready cryomodule. The helium vessel also eliminated the need for a large helium tank used in the first cryo-

genic tests.

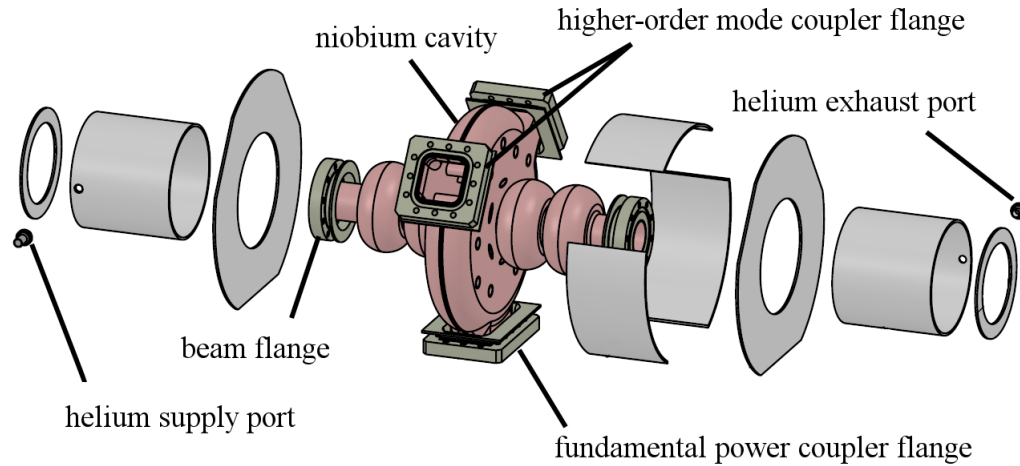


Figure 4-11: A schematic showing an addition of the helium vessel to the cavity.

We tested how much the cavity inside the helium vessel can be tuned by external compression or extension. The cavity in the helium vessel was pressed between two aluminum plates that could be tightened together, as shown in Figure 4-12. It was found that the frequency of the accelerating mode changes by 1.1 MHz per one mm of compression. Bead-pull measurement showed that a deformation by 1.8 mm only resulted in about 1% deviation from the original gradient profile. The cavity could, therefore, be tuned to a particular frequency by compressing or extending it by a few mm, without a significant degradation of the accelerating properties.

4.4 Fabrication of RF loads and sliding shorts

For HOM measurements that will be described next in Chapter 5, the waveguides of the 5-cell cavity had to be terminated with RF loads or sliding shorts. In order to simplify the process of fabrication of the RF loads, it was decided to taper out the HOM waveguides of custom dimensions to a standard waveguide size WR510. For the FPC waveguide, no taper was needed and the load was made of the standard waveguide WR430 size. The inner structure of the loads and the arrangement of the loads and the tapers are shown in Figure 4-13.

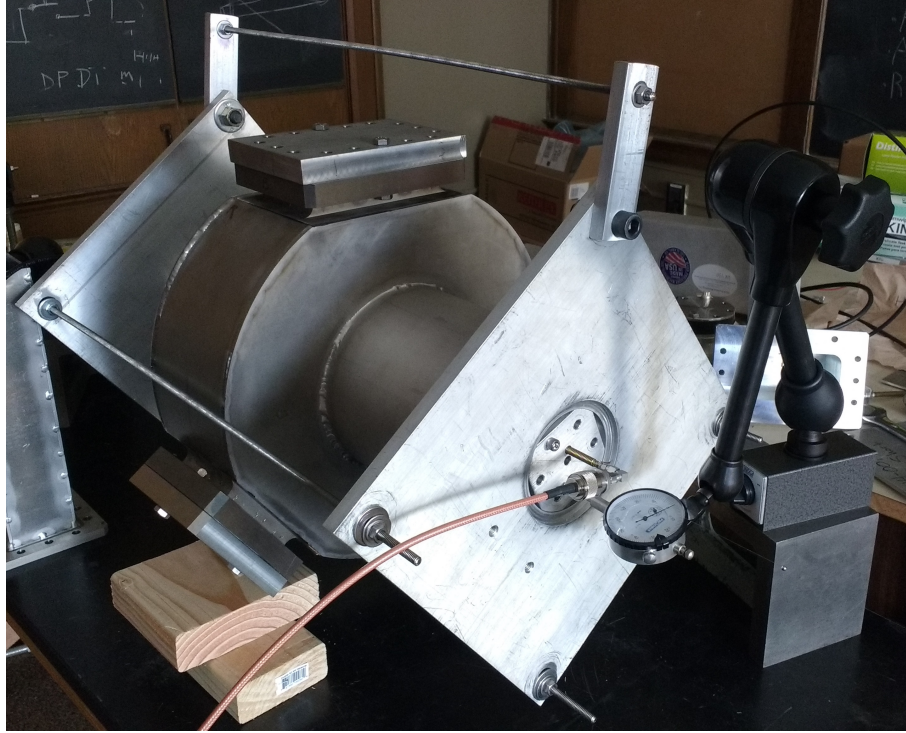


Figure 4-12: The mechanical setup for measuring the tuning capability of the niobium cavity in the helium vessel.

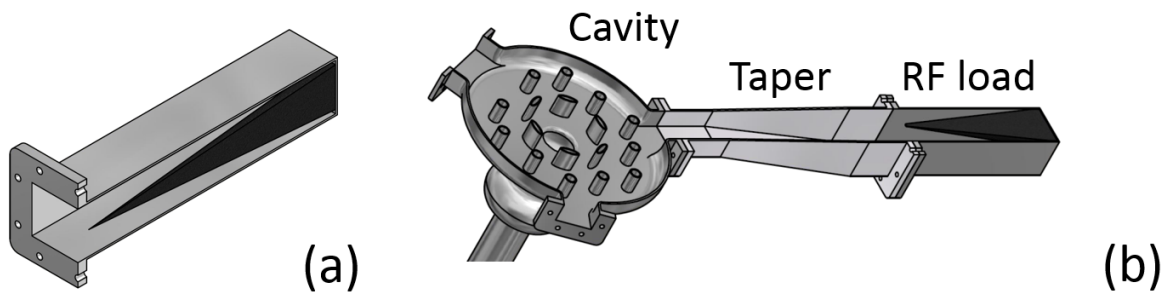


Figure 4-13: (a) Drawing of the RF load for the FPC. (b) A schematic showing the arrangement of RF loads and tapers.

Waveguide tapers and metal housings for the loads were manufactured from aluminum. The cones of absorbing material were fabricated by Emerson and Cuming. A particular kind of material called ECCOSORB was chosen for the cones based on its damping properties at the frequencies from 2 to 4 GHz. The cones were glued to the housings with epoxy glue.

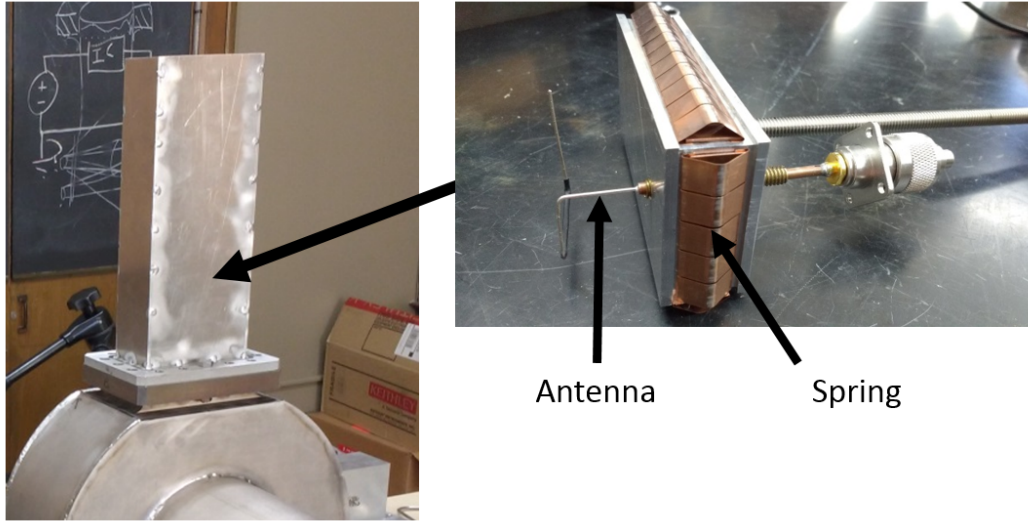


Figure 4-14: Sliding short for the FPC waveguide. An aluminum plate with a sliding spring is put inside a piece of WR430 waveguide. The antenna is inserted through a hole in the plate.

Sliding shorts for all three waveguides were made of aluminum. To make the shorts, plates with sliding springs were inserted into pieces of rectangular waveguides (Figure 4-14). Small holes were made in the sliding plates to fit custom-made antennas. The antennas were made from a piece of a coaxial line. The outer copper conductor was stripped off to allow mode excitation with the inner steel conductor that was bent in a special shape (see Figure 4-14) to provide a stronger coupling to the waveguide mode.

4.5 Summary

In this chapter, we described fabrication and tuning steps implemented for the niobium cavity and its copper prototype. The last step in the fabrication and tuning process is welding of the cavity. Welding of the copper prototype was unsuccessful, however, welding of the niobium cavity went as expected. After the welding, the niobium cavity underwent surface preparation necessary for the cryogenic tests described in Chapter 6. Finally, we briefly described the fabrication of auxiliary parts (RF loads and sliding shorts) used for the HOM measurements described in Chapter

5.

Chapter 5

Higher order mode damping measurements

The main goal of measurements described in this Chapter was to verify the results of HOM damping simulations obtained in Chapter 3. For that, a series of room-temperature tests were conducted using both the fabricated niobium cavity and its copper prototype. We measured the frequencies, the field profiles, and the external Q-factors of the monopole passband modes and the dipole HOMs listed in Table 3.4.

To obtain Q_{ext} , we separately measured the values of the total (loaded) Q-factor Q_L and the unloaded Q-factor Q_0 , and used a relationship that follows from the definitions of the Q-factors (see Glossary):

$$\frac{1}{Q_{ext}} = \frac{1}{Q_L} - \frac{1}{Q_0}. \quad (5.1)$$

For SRF cavities, a cryogenic test is usually necessary to accurately measure Q_{ext} values if they are much greater than the unloaded Q-factors Q_0 at room temperature. According to the Equation 5.1, a change in Q_{ext} only slightly affects measured values of the total Q-factors Q_L that are already dominated by the Ohmic losses. However, in our case, all of the dangerous dipole modes listed in Table 3.4 are damped to Q_{ext} lower than or comparable to their room-temperature Q_0 (typically around 5×10^3 in a niobium cavity or 1.5×10^4 in a copper cavity). Therefore, it was sufficient to do a

series of much simpler room-temperature tests to characterize HOM damping.

The mentioned higher typical values of Q_0 in a copper cavity are related to the fact that conductivity of copper at room temperature is about 10 times higher than that of niobium. Hence, Q_{ext} could be calculated more accurately in the copper prototype which was fabricated prior to the niobium cavity (see Chapter 4). The higher Q_0 also means reduced mode overlapping. Mode overlapping happens if bandwidths of neighboring HOMs are comparable to their frequency separation. Bandwidths of the HOMs are inversely proportional to their Q-factors and are therefore smaller in the copper cavity.

Some HOM measurement were done in the copper cavity in a "stacked" setup (the cells are held together by applying vertical pressure). As was discussed in Chapter 4, an attempt to weld the parts of the copper cavity together was unsuccessful, leaving gaps between the cells. The gaps made it impossible to complete the HOM damping measurements in the copper prototype. However, the same measurement techniques were later applied to the niobium cavity. Despite the stronger mode overlapping in the niobium cavity, we could still identify and separate the dangerous modes listed in Table 3.4. Below we discuss the general techniques used for both cavities, and the final results are listed for the niobium cavity.

5.1 Measurement setup

A typical setup for the HOM measurements is shown in Figure 5-1. In this setup, the cavity's HOM waveguide ports were tapered out to match the dimensions of the standard waveguide WR510. The farther ends of the tapers were either shorted with metal plates, or left open, or connected to specially made RF loads described in Chapter 4. The FPC was already made with the dimensions of a standard waveguide WR430 and did not need to be tapered out. Similar to the HOM waveguides, the FPC was either shorted, or left open, or connected to a load. For mode excitation through the FPC, the waveguide could also be connected to a waveguide-to-coaxial mode converter, as shown in Figure 5-1.

The HOMs were primarily excited through two weakly coupled loop antennas inserted on the opposite sides of the beam-pipe. A loop antenna is simply a piece of metal wire formed in a loop with both ends connected to a coaxial line (a zoomed-in photo of a loop antenna is shown on the right of Figure 5-1). The antenna couples to RF modes that have the magnetic field component perpendicular to the plane of the loop.

The strength of coupling in our setup could be varied by adjusting the depth of the antenna insertion. Weak coupling was used to not affect the measurements of the Q-factors associated with the waveguide damping. Thus, the antennas only introduced small perturbations to the measured modes. The weakness of the coupling was verified by making sure the transmission between two loop antennas inserted on the opposite sides of the cavity was lower than -40 dB at the observed frequency range.

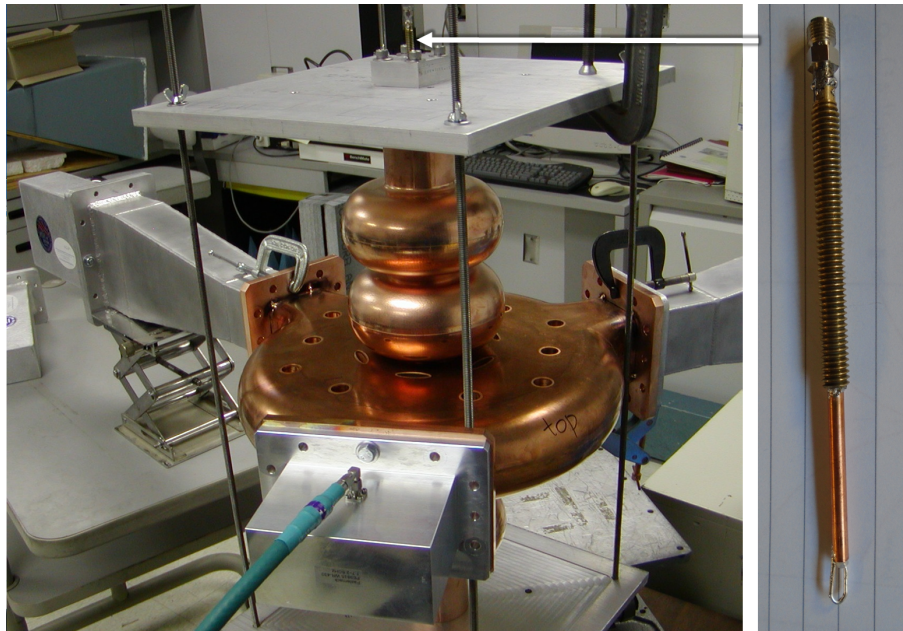


Figure 5-1: A typical setup for HOM damping measurements shown for the copper cavity. The FPC is connected to a waveguide-to-coaxial mode converter. The HOM waveguides are tapered out and terminated with RF loads. Loop antennas are inserted in the beam-pipe and aligned with the central axis.

The antennas were rotated around the cavity's central axis in order to only excite one polarization of the dipole modes at a time (X or Y). The selective excitation of

one polarization is related to the fact that the dipole HOMs couple to the TE₁₁ mode of the beam-pipe. A correctly positioned loop antenna only excites the polarization of the TE₁₁ mode with the electric field in the plane of the loop, which was clearly seen in the experiment by observing the shape of the transmission signal.

The measurements consisted of obtaining transmission (S_{21}) profiles as functions of the frequency for different combinations of the waveguide boundary conditions and excitation schemes. The S_{21} measured in dB is defined as

$$S_{21}[\text{dB}] = 10 \log_{10} \frac{P_{out}}{P_{in}}, \quad (5.2)$$

where P_{in} is the input power to the cavity and P_{out} is the output power from the cavity. The Q-factors were estimated using the shapes of the measured S_{21} profiles.

To measure the field patterns of the HOMs, a bead-pull setup was incorporated in the test stand (the bead-pull technique is described in [94]). The bead-pull setup was similar to the one described in Section 4.2. For the HOM measurements, however, the bead polyester thread was shifted off-axis by about 1 cm to make room for the loop antennas that were exactly aligned with the cavity's central axis.

5.2 Identifying the modes

The first step in measuring the HOM damping properties was to identify the dangerous modes from Table 3.4 as peaks in the experimental S_{21} data. Once the mapping was done, we could proceed with measuring the Q-factors (see the next section).

First, we compared the frequencies of the peaks in the S_{21} profile to the simulated frequencies of the HOMs. Based on the tolerances of fabrication (see the detailed drawings in Supplemental Materials [10]), we expected the frequencies in the fabricated cavity to be within 50 MHz from the simulated frequencies (Tables 3.4 and 3.5). However, in some cases multiple peaks appeared within the range of possible frequencies, making a simple frequency check insufficient to identify the modes.

Next, we simulated the approximate shape of the S_{21} profile for the designed

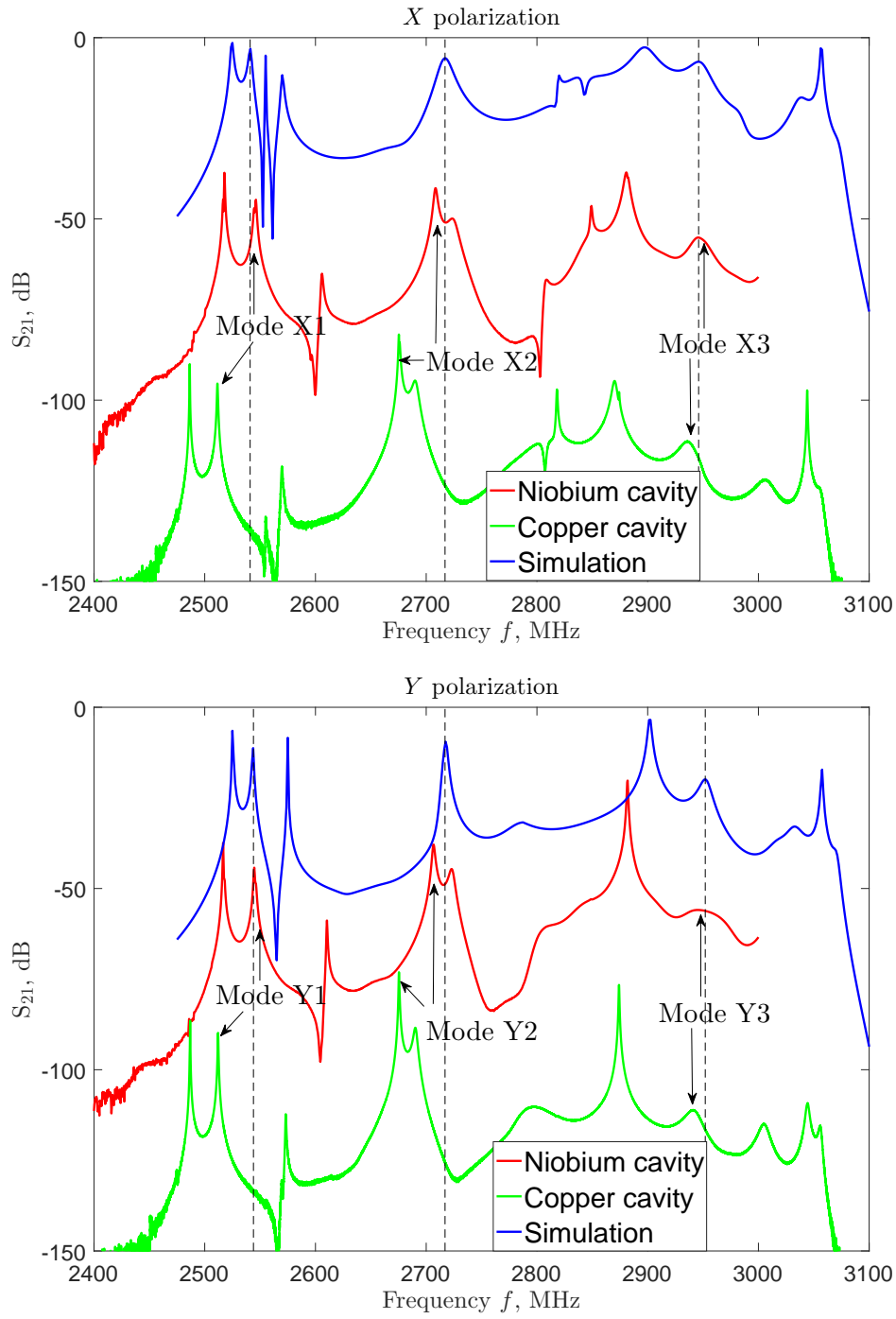


Figure 5-2: Comparison between the measurement and the simulation of the S_{21} profile for the X and the Y polarizations. Measured S_{21} for copper cavity was shifted down by 50 dB for illustration purposes. All waveguides were terminated with RF loads. Similarity of the shapes gives an insight on which simulation peaks correspond to the modes in the fabricated cavities. Mode overlapping (merging of two peaks with close frequencies) can be seen for the simulation peaks at around 2.7 GHz for both X and Y polarizations due to the low Q-factors of the modes.

cavity. We set up a “Driven Modal” HFSS simulation that included models of the loop antennas in the beam-pipe (see Supplemental Materials [11]). The simulated profile was then compared to the measured S_{21} data. Such comparison for both X and Y polarizations is shown in Figure 5-2 for the welded niobium cavity and the copper prototype. The measurement in the copper prototype was done before the attempt to weld the cavity, and the cells were held together by applying vertical pressure. S_{21} in the copper cavity was measured up to the frequency of 3.1 GHz, however, the measurements in the niobium cavity were only limited to 3.0 GHz due to the range of the network analyzer available at the time.

We expected the high impedance HOMs from Table 3.4 to correspond to visible peaks in S_{21} , as long as the antennas were correctly positioned to couple into the modes. The peaks corresponding to the dangerous modes did not necessarily correspond to the highest S_{21} because coupling to the beam is different from coupling to the antennas. It can be seen in Figure 5-2 that the relative strengths of the peaks in the simulation resemble the relative strengths of the peaks in the experimentally obtained S_{21} . The absolute coupling strength does not matter for our purposes, as it is only a function of how the antennas are positioned in the experiment or the simulation (see Appendix A and additional files in Supplemental Materials [11]).

The frequencies of the peaks in the experimental data deviated from the frequencies of the peaks in the simulation because of fabrication tolerances mentioned above. Mode overlapping (merging of two peaks with close frequencies) can also be seen in Figure 5-2 for the simulation peaks at 2.7 GHz (X_2 and Y_2 modes) due to the low Q-factors of the modes.

Field patterns of the obtained solutions were observed for all the S_{21} peaks. Among field patterns for the modes polarized in X direction, we chose three that corresponded to the dangerous modes X_1 , X_2 , and X_3 . The same process was repeated for the Y -polarization and the modes Y_1 , Y_2 , and Y_3 were identified. The field patterns for these six modes are shown in Figure 5-3. Thus, the six dangerous HOMs were mapped to the S_{21} marked with the vertical dashed lines in Figure 5-2.

Frequency deviations of the modes identified in the niobium cavity from the sim-

Table 5.1: Differences in frequencies of the modes identified in the niobium cavity from the design frequencies (from Tables 3.4 and 3.5).

Mode	Design f , GHz	Measured f , GHz	Δf , MHz
X_1	2.538	2.546	8
X_2	2.713	2.705	8
X_3	2.936	2.972	36
Y_1	2.539	2.545	6
Y_2	2.711	2.708	3
Y_3	2.940	2.969	29

ulated frequencies are summarized in Table 5.1. It can be seen that the frequency deviations of the X_3 and the Y_3 modes were the largest, which is consistent with their very low Q-factors (see measurements below, Table 5.2). Indeed, strong coupling of the two modes to the waveguides makes their frequencies very sensitive to the boundary conditions.

By rotating the loop antennas around the axis of the cavity, it was observed that the polarizations of the X_1 and Y_1 modes did not exactly align with the X and Y axis. The two polarizations were still orthogonal to each other but rotated by about 40° relative to the X and Y axis. This rotation can be explained by the fact that the two modes have relatively low fields in the PBG cell and thus their polarizations are only weakly affected by the waveguides. Instead, the polarizations could be dictated by small asymmetries in the elliptical cells caused by the fabrication tolerances.

To verify the mode identification, we compared two different ways to excite the mode: the FPC-antenna excitation and the two-antenna excitation. Due to their symmetries, some HOMs could not be excited by the FPC and we expected the corresponding peaks to disappear from the S_{21} profile. To demonstrate the idea, we only describe the results for the X polarization here, although the same was done for the Y polarization. According to the simulation, such "disappearing" HOMs include the X_1 mode and the mode neighboring the X_2 mode. This expectation was indeed confirmed experimentally by comparing the S_{21} profiles for the copper cavity for the two methods (Figure 5-4), indicating the accuracy of the mode identification.

Finally, the bead-pull technique was used to verify that the measured peaks in S_{21}

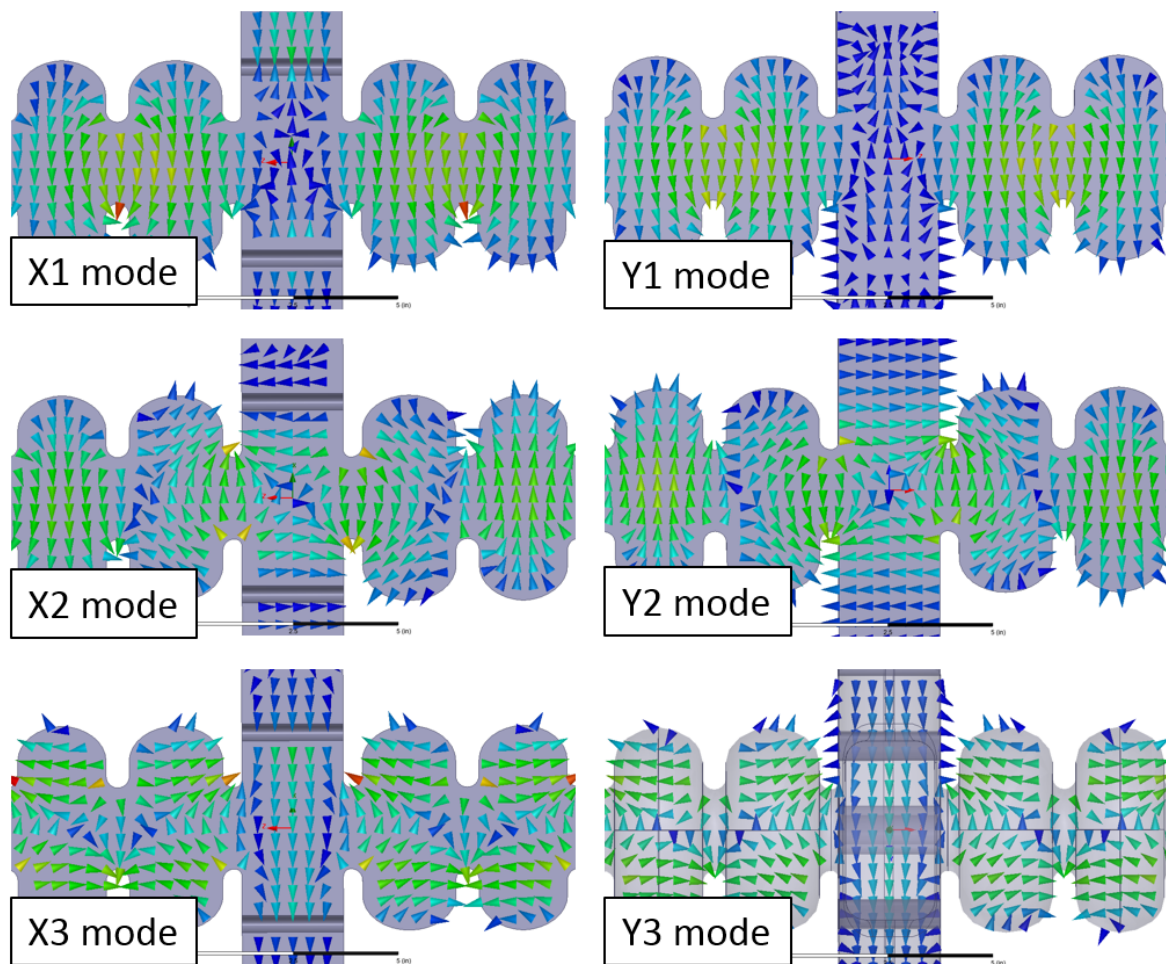


Figure 5-3: Simulated electric field patterns of the modes corresponding to the six peaks in Figure 5-2 marked with the vertical dashed lines (see Appendix A and additional files in Supplemental Materials [11]). These patterns match with the patterns of the X_1 , X_2 , and X_3 modes simulated in Chapter 3.

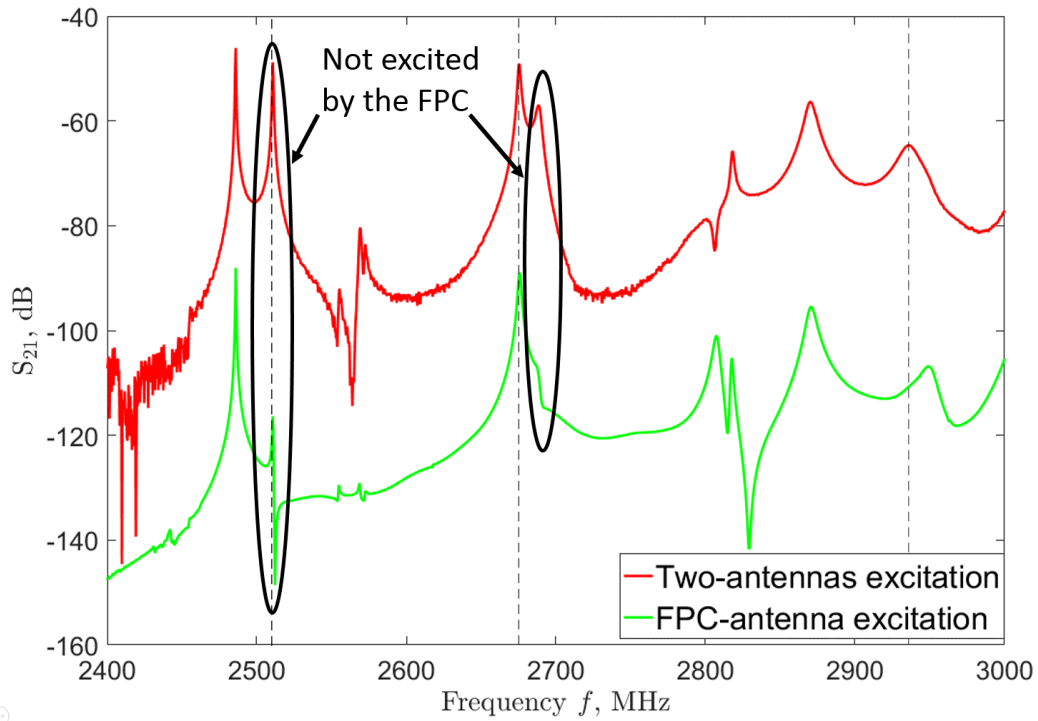


Figure 5-4: Comparison between the two different excitation methods: the two-antenna excitation and the FPC-antenna excitation. The green curve is shifted down by 60 dB illustration purposes. Some peaks exist if the first excitation method is used but disappear in the second method is used. Such modes must have the field pattern prohibiting the FPC-excitation (zero electric field along the X -axis).

had the right field profiles. We measured phase deviation of the signal transmitted between the two loop antennas, which is proportional to the following combination of fields: $\epsilon E^2 - (1/2)\mu H^2$ [102]. For the case of the monopole modes, this expression is reduced to just the electric field, since \mathbf{H} is zero on the central axis and small along the bead line. We first measured the bead-pull profiles for the monopole modes below 3 GHz (the upper-frequency limitation of the available network analyzers, model HP8714ET). Only the five previously mentioned passband modes fall within this frequency range. Their monopole profiles are compared to simulations in Figure 5-5. Agreement between the shapes of the measurements and the simulated profiles indicates the reliability of the used technique.

We then measured the bead-pull profiles for the dipole modes below 3 GHz. The combination of fields $\epsilon E^2 - (1/2)\mu H^2$ was calculated for the simulated modes and the expected phase deviation was estimated as a function of the location of the bead. It was then compared to the measured phase deviation (Figure 5-6). Thus, the bead-pull measurement further confirmed the accuracy of the identification of the modes.

5.3 Quality factor measurements

In this section, we describe measurements of external Q-factors of the dangerous HOMs that were done using two different damping methods. The first method relies on RF loads (see Chapter 4 for the fabrication) to provide HOM damping and was expected to provide Q-factors that agree with the earlier simulations (Chapter 3). The second method can be viewed as an additional damping scheme. The method used sliding shorts instead of the RF loads. The goal of the second method was to demonstrate that a stronger damping can be achieved for a particular HOM if needed.

In addition to the HOM measurements presented below, the same setup was also used to measure the coupling strength of the accelerating mode to the FPC. For that, we compared the S_{21} profiles obtained with the two different ways to excite the mode: the two-antenna excitation and the FPC-antenna excitation. In the copper cavity, the total Q-factors of the mode were $Q_L^{antennas} = 1.507 \times 10^4$ and $Q_L^{FPC-antenna} = 9.01 \times$

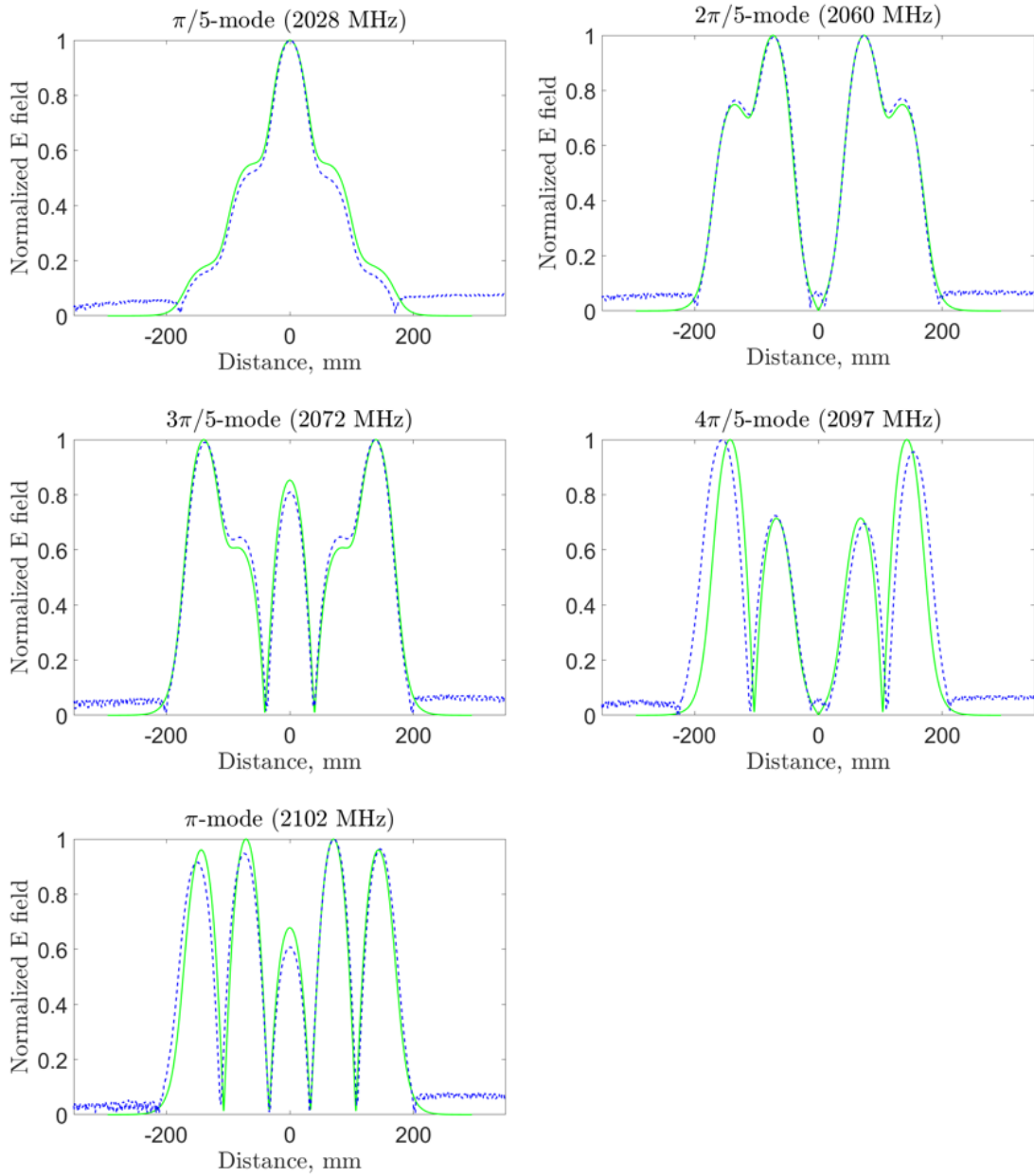


Figure 5-5: Comparison between the bead-pull field measurements (solid green lines) and the simulated profiles (dashed blue lines, see the simulation files in Supplemental Materials [4]) for the monopole modes with frequencies below 3 GHz. Only the 5 passband modes fall within the measured frequency range 0 - 3 GHz.

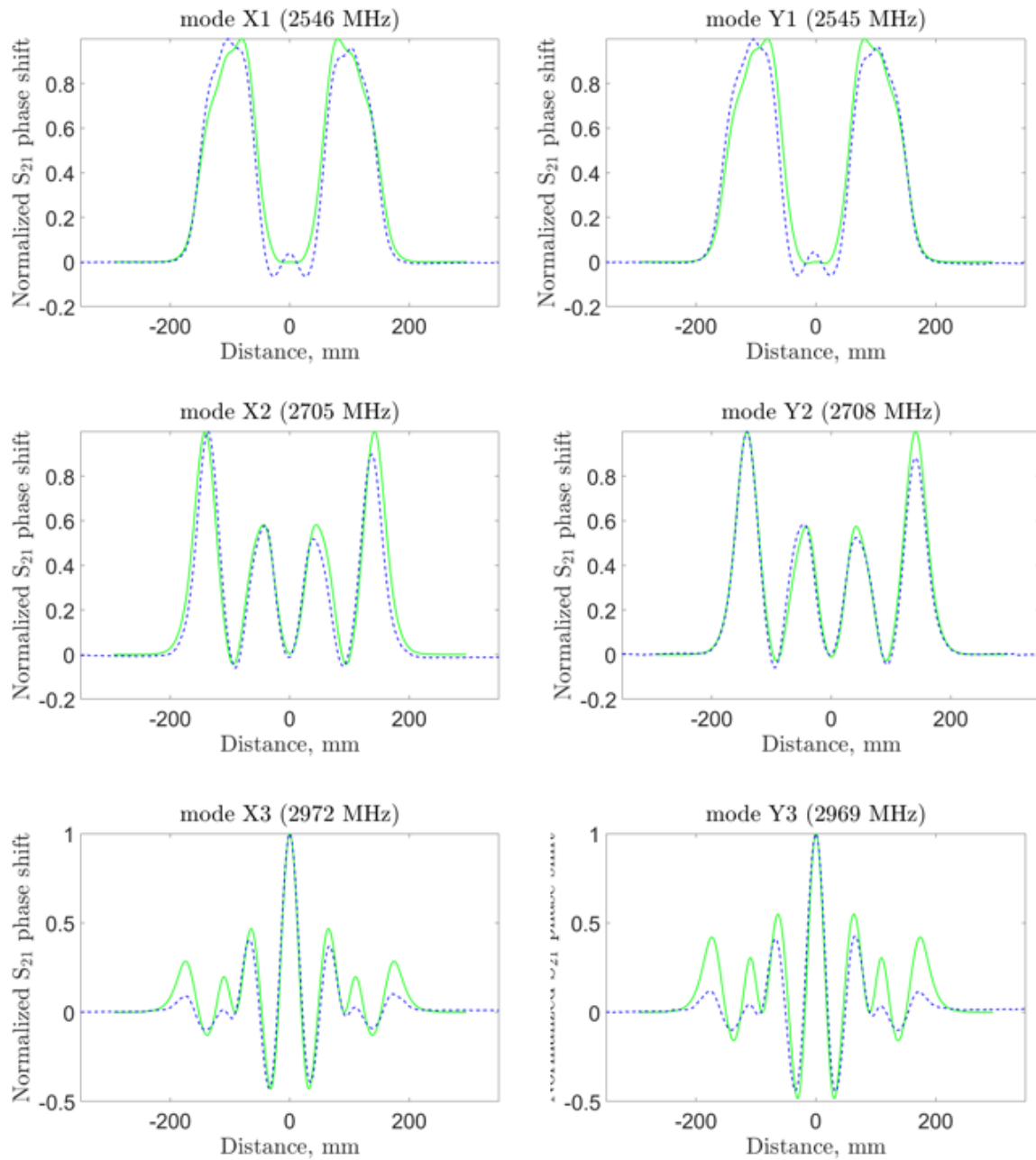


Figure 5-6: Comparison between the bead-pull measurements (solid green lines) and the simulated profiles (dashed blue lines, see the simulation files in Supplemental Materials [4]) for the dipole modes with frequencies below 3 GHz. Six of the ten dangerous modes fall within the measured frequency range 0 - 3 GHz. Shapes of the measured curves resemble the shapes of simulated curves, indicating that the identification of the modes in the experimental S_{21} profile is correct.

10^3 . Using Equation (5.1), the coupling Q-factor was found to be $Q_{ext} = 2.24 \times 10^4$. The same quantity was estimated by analyzing the shape of the corresponding dip in the S_{11} profile obtained using the FPC-excitation: $Q_{ext} = 2.37 \times 10^4$. Both values agree within 20% with the design coupling strength $Q_{ext} = 2 \times 10^4$ (see Chapter 3).

5.3.1 Measurements with RF loads

To obtain the external Q-factors Q_{ext} for HOMs, we used Equation (5.1). According to Equation (5.1), two measurements were required: the measurement of the total Q-factors Q_L and the measurement of the unloaded Q-factors Q_0 .

To measure Q_L , we had to provide absorption boundaries to all three waveguides. For that, the waveguides were terminated with specially made RF loads or a waveguide-to-coaxial mode converter (if excitation through the FPC was needed), as shown in Figure 5-1. To measure Q_0 , the waveguides were shorted with metal plates. The two loop antennas were used to excite the modes. This method worked well for $Q_{ext} \gg 10^2$, when frequency and field distribution independent of where the waveguides are shorted.

Using this technique, quality factors for six dangerous dipole HOMs below 3 GHz were measured. The upper-frequency limit of 3 GHz was due to the available network analyzers at Niowave Inc, where the measurements were made. A MATLAB code was used to process the obtained S_{21} profiles for the different boundary conditions on the waveguides and to calculate the Q-factors through the widths of the peaks. An example of S_{21} data for the X_1 mode is shown in Figure 5-7.

The results of the measurements are summarized in Table 5.2. For all of the measured modes except the modes X_3 and Y_3 we can see a relatively good agreement between the simulations and the measurements (within 30%). Deviation from the theory within 30% is reasonable for these measurements due to the high sensitivity of the external Q-factors to manufacturing errors. However, the modes X_3 and Y_3 showed Q_{ext} far from the expectations, and even lower than the expected values.

We estimated errors in the Q-factors measurements due to peak overlapping. Overlapping introduces asymmetry to a peak in S_{21} and makes the left side slope different

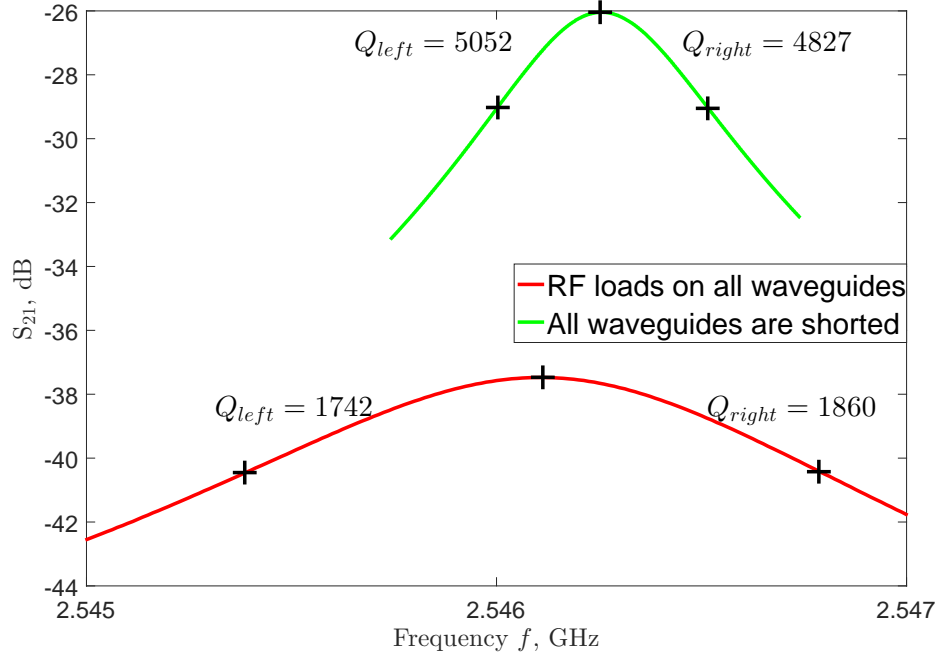


Figure 5-7: Comparison between the profile of the S_{21} peaks of the X_1 mode for the two boundary conditions on the waveguides. The cross-shaped markers are used to independently estimate Q -factors for the left and the right parts of the peaks.

from the right side slope. We estimated the errors by comparing Q factors computed separately for the left and the right sides of the S_{21} peaks. The resulting errors are within $\pm 12\%$ for all the modes and cannot explain the measured Q -values for the modes X_3 and Y_3 . Extremely low Q_{ext} of X_3 and Y_3 make them sensitive to the boundary conditions in the waveguides and the shape of the periphery of the PBG cell. It is therefore possible that the field patterns of the modes in the fabricated cavity were slightly different from those predicted in the simulations, which resulted in lower values of Q_{ext} .

5.3.2 Measurements with sliding shorts

As was discussed in Chapter 4, three sliding shorts for the three waveguides of the cavity were fabricated. The sliding shorts consisted of sections of a waveguide with a variable length and antennas to couple out the power of the damped mode (see Figure 4-14). As opposed to HOM measurements with RF loads, the sliding short

Table 5.2: Comparison between simulated and measured external Q factors for 6 of the dangerous HOMs.

Mode	f , GHz	Q_0 , measured	Q_L , measured	Q_{ext} , measured	Q_{ext} , simulated
X_1	2.546	4940	1801	2.7×10^3	2.7×10^3
X_2	2.705	4165	806	9.4×10^2	7.5×10^2
X_3	2.972	5501	145	1.4×10^2	3.0×10^2
Y_1	2.545	5042	1957	3.0×10^3	2.7×10^3
Y_2	2.708	5274	1022	1.3×10^3	9.4×10^2
Y_3	2.969	6723	110	1.1×10^2	2.6×10^2

method requires a precise adjustment of the shorts for a particular mode. If one particularly dangerous HOM is found in the structure, it can be damped very efficiently with one or several sliding shorts by sacrificing damping of other HOMs.

Using the sliding short method, a mode can be damped to an even lower Q_{ext} that is achievable with perfect RF loads. This can be explained by the fact that the field pattern of the damped mode is significantly distorted when the length of the short is adjusted properly. The cavity mode interacts with the mode inside the sliding short, which results in strong fields in the waveguide. These strong fields allow us to achieve enhanced damping of the mode.

Because of the mode mixing, we found that adjustment of all three sliding shorts was a rather complex task. Instead, we decided to demonstrate the principle of sliding short damping using only the FPC sliding short in application to the most dangerous dipole mode polarized in X direction. According to Table 3.4, this is the X_2 mode at the frequency of 2.7 GHz (it has the highest shunt impedance). Below we describe the method we used to adjust the sliding short.

First, the two optimal parameters of the short were found: the length of the short and the coupling strength of the antenna at the end of the short. The length of the short was adjusted so that the standing wave mode in the short approximately matched the frequency of the damped HOM. The exact matching never happened because of the mode mixing. Then, the coupling of the antenna was adjusted. The two extreme cases (the case of zero coupling and the case of a perfect load) correspond to higher Q-factors than can be achieved with some optimal coupling. An HFSS

simulation was used to find this optimal coupling. Figure 5-8 shows the simulation setup, with the sliding short represented by the FPC extension, and the antenna represented by a piece of a coaxial waveguide.

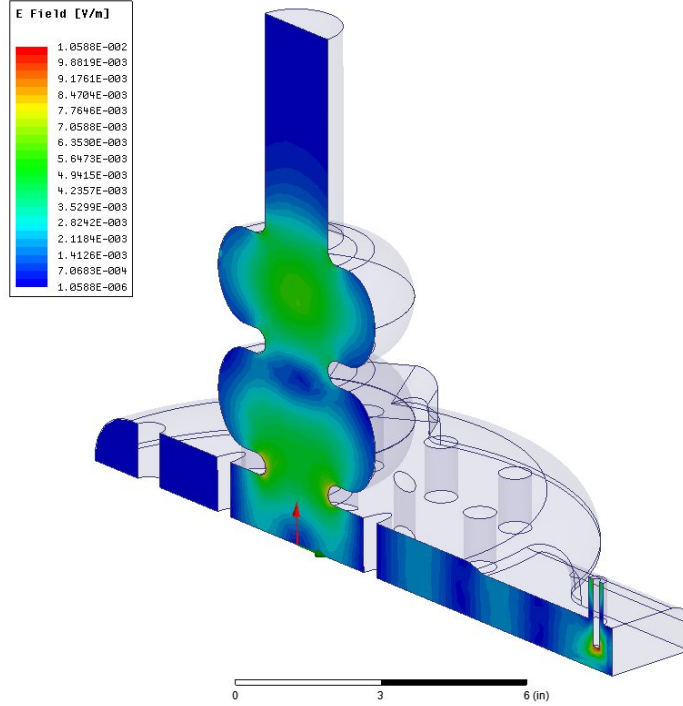


Figure 5-8: An HFSS simulation of damping of the X_2 mode with the FPC sliding short. One-quarter of the structure is shown because of the $X - Y$ and the $X - Z$ symmetry planes. The color is showing the magnitude of the electric field in the $X - Z$ plane. A significant part of the mode's energy is coupled to the waveguide due to the resonance condition between the cavity mode and the waveguide mode.

It was found that for the length of the short of 67 mm and the coupling strength between the waveguide and the antenna $S_{21} = -5$ dB, the X_2 mode could be damped with the $Q_{ext} = 270$. These parameters were tested experimentally. The coupling strength was adjusted by moving the antenna up or down in the short. It was found that by varying the two parameters we could achieve $Q_{ext} \leq 400$. Measuring Q-factor lower than 400 is difficult due to the very large bandwidth which causes mode overlapping.

The achieved Q_{ext} of 400 or less is significantly lower than $Q_{ext} = 940$ which was obtained with the RF loads (see Table 5.2). It was therefore demonstrated that the sliding short method is an effective way to damp one particularly problematic HOM

if it appears in future experiments.

5.4 Summary

In this chapter, we presented HOM measurements in the fabricated five-cell PBG cavity. The measurements included the frequencies, the field profiles, and the external Q-factors of the monopole passband modes and the dipole HOMs listed in Table 3.4. Six of the dangerous modes from Table 3.4 were measured, with the external Q-factors lower than the predictions or within 30% from the predictions. This proves that the structure achieves effective HOM damping, necessary to increase the BBU current threshold. Experiments with sliding short damping showed that an even stronger damping can be achieved for a particular mode if it is found to be especially dangerous in a beam experiment.

Chapter 6

Cryogenic tests of the niobium five-cell cavity

In this Chapter, we will discuss cryogenic tests that were conducted with the fabricated 5-cell niobium cavity with a PBG cell, shown in Figure 4-7. The type of cryogenic testing described below is called “vertical testing” and is a common technique for testing SRF cavities [96, 98, 99, 100]. In a vertical test, the ultimate performance of a cavity is tested in terms of the maximum achievable accelerating gradient and the unloaded Q-factor, with the absence of a particle beam. The word “vertical” refers to the orientation of the tested cavity. When no particle beam is involved, the vertical orientation of the cavity is more convenient for testing in helium dewars. The temperature of liquid helium in a vertical test can be varied by changing the pressure inside the dewar (temperature vs pressure diagram is shown in Figure 6-1).

There were several reasons to conduct a vertical testing of the designed cavity. The first reason was to test the reliability of the fabrication process. For a cavity of such complex shape, microscopic gaps can occur in the joints where the parts were electron-beam welded. The smallest gaps only show up when the cavity is immersed in superfluid helium. This phenomenon is referred to as a “superleak”. Helium becomes superfluid at a temperature below the λ -point (2.17 K at the atmospheric pressure), as can be seen in Figure 6-1. Hence, a cryogenic test was needed.

The second reason was to assess the effectiveness of the surface preparation in the

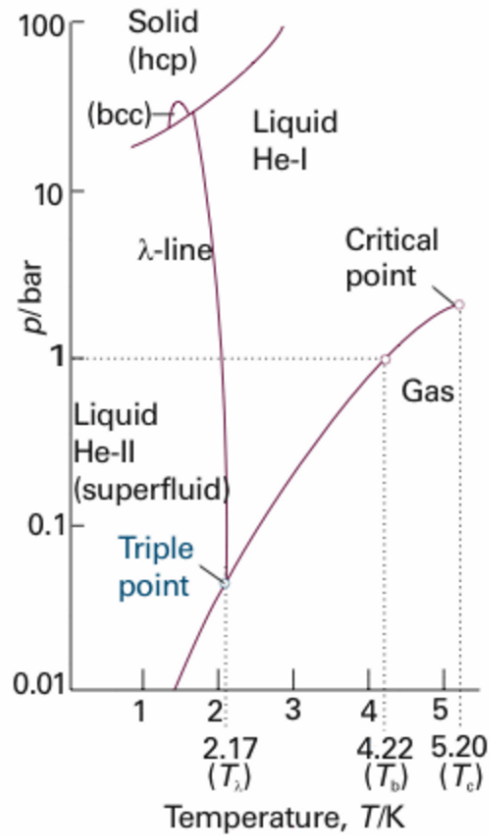


Figure 6-1: Phase diagram of ^4He at low temperatures. The dependence of the temperature of liquid helium on pressure (lower red curve) allows varying the temperature in a cryotest by changing the pressure inside the dewar. Superfluid state can be achieved by lowering the dewar pressure below the pressure of the “triple point”.

cavity. Uniformity of material removal during chemical processing depends on the flow of the acid solution inside the cavity, which has not been studied for a cavity of this shape. Comparison of the measured unloaded Q-factor to the theoretical prediction can reveal a problem in the surface treatment procedure (e.g. the “Q-disease” [31]).

The third reason was to find the maximum achievable accelerating gradient in the cavity. The achievable gradient can be limited by quenching, multipacting, and field emission. The PBG cell could be prone to multipacting because its shape was optimized for HOM damping rather than for the accelerating performance. Therefore, even a low-level multipacting was possible. In the worst case scenario an unexpected “hard barrier” could have been encountered - a level of accelerating field in the cavity that could not be surpassed by feeding in more RF power. The vertical testing gave

us an opportunity to check such possibility.

For all these reasons, the vertical testing is considered to be an essential step in the process of all SRF cavities' certifications.

6.1 First cryogenic testing at LANL

After the fabrication (see Chapter 4), the niobium cavity was shipped to LANL, where it was assembled with other parts necessary for the vertical test in a class 100 clean room. Parts of the assembly are shown in Figure 6-2. RF coupling to the cavity was done through an adjustable coaxial drive probe mounted in the cavity's beam-pipe. A non-adjustable pickup probe was mounted on the opposite side of the beam-pipe. With the two probes, both reflection and transmission measurements could be used to characterize the cavity's behavior.

Both probes were hollow polished aluminum rods designed to match the 50Ω impedance of coaxial lines. The pickup probe was designed to provide external quality factor $Q_{ext} = 6 \times 10^{11} \gg Q_0$, and the drive probe was designed to provide Q_{ext} in the range $2 \times 10^7 < Q_{ext} < 10^{10}$. Adjustability of the drive probe was needed to achieve critical coupling at different temperatures and gradients. It was provided by bellows that could be squeezed or extended to change Q_{ext} , as can be seen in Figure 6-2 (a). A macor support plate was placed in the beam-pipe to prevent the long drive probe from tilting relative to the axis.

After assembling, the structure was sealed and taken outside of the clean room and hanged on the "insert" - a system of supports that could be lowered in a cryostat. The cavity mounted on the insert is shown in Figure 6-2 (b). The movable part of the drive probe assembly was connected to long metal bars that allowed moving the probe up and down. The drive and the pickup RF cables were connected to the lid of the insert. Time-domain reflectometry (TDR) was used to make sure that there were no unexpected reflections in the drive and the pickup transmission lines. The vacuum line (the large pipe on the right of Figure 6-2 (b)) was connected to the cavity. An ion pump located on the lid of the insert was used to provide high vacuum inside the

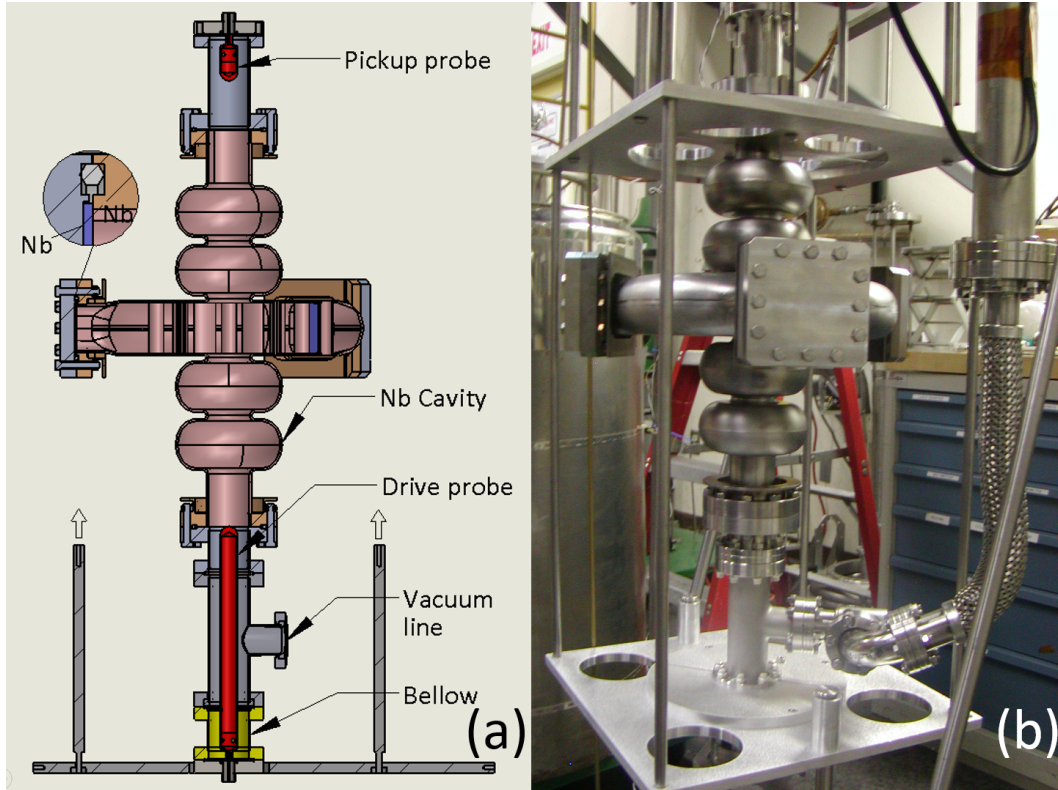


Figure 6-2: A drawing (a) and a photograph (b) of the 5-cell cavity with the drive probe assembly the pickup probe assembly.

cavity.

First, the cavity was pumped to the low pressure of 6×10^{-7} Torr. Then, a baking process (an additional step of preparation to the cryogenic test) was started. It is believed that baking can reduce the degradation of the Q-factor at high accelerating gradients [31], although accelerating gradients needed to observe this effect were not achieved in the test (see below). Heating tapes were wrapped around the cavity, the vacuum line, and the bellows. The assembly was baked at $120\text{ }^{\circ}\text{C}$ for 2 days. The cavity was then pumped down to 5×10^{-8} Torr before lowering it into the cryostat. A temporary leak occurred while the cavity was cooling down after the baking. Using a leak detector, we quickly traced the leak to the FPC flange. We tightened the bolts in the flange to the torque of 30 ft-lb, which fixed the leak.

After the needed vacuum was reached, the insert was lifted with a crane and lowered in a cryostat, shown in Figure 6-3. The cryostat was equipped with a magnetic

field compensating coil that reduced the ambient magnetic field at the location of the cavity to < 10 mG [101]. The cavity was quickly covered with helium to prevent hydrides from forming on the inside surface (Q-disease).

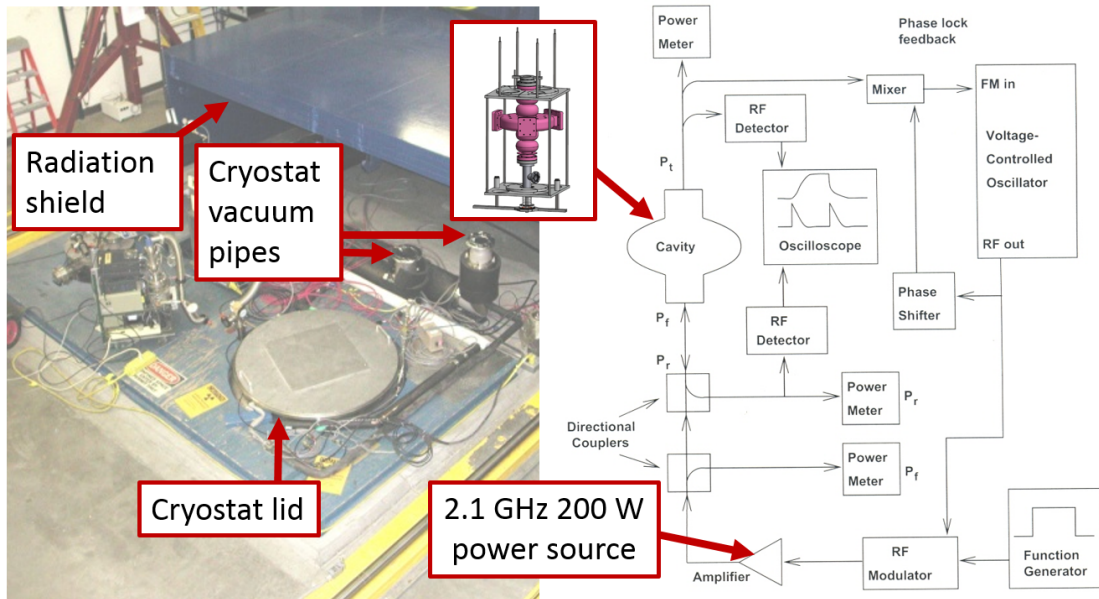


Figure 6-3: A photo of the cryostat and a schematic of the RF setup used for the vertical testing at LANL. The cryostat is a well 2.97 m deep and 0.965 m in diameter, covered with a lid in the photo. The RF setup includes a standard for vertical testing phase-lock loop to lock on the cavity’s frequency (picture is taken from [31]).

Cables from the top lid of the insert were connected to the RF amplifier and the control room. A TWT amplifier was used to provide RF power at the frequency of 2.1 GHz with power varying from 200 mW to 200 W. In the control room, a phase lock loop was used for a precise control of the generator’s frequency. The phase lock loop is a feedback loop that detects a variation in the cavity’s frequency due to mechanical vibrations and adjusts the RF generator’s frequency accordingly.

In the test, we measured Q-factors and field levels for different monopole “pass-band” modes in the cavity, ranging in frequency from 2.028 to 2.105 GHz. As was discussed in Chapter 3, the 5-cell cavity has 5 passband modes that are classified according to their phase advance over the length of one cell: from $\pi/5$ to π . Electric field profiles along the central axis, simulated for different modes in the fabricated cavity, are plotted in Figure 6-4 (see the simulation files in Supplemental Materials

[4]). The $\pi/5$ mode was not excited in this experiment due to its relatively weak coupling to the drive probe (indeed, its field in the beampipes is much lower than that of the other four modes, as shown in Figure 6-4).

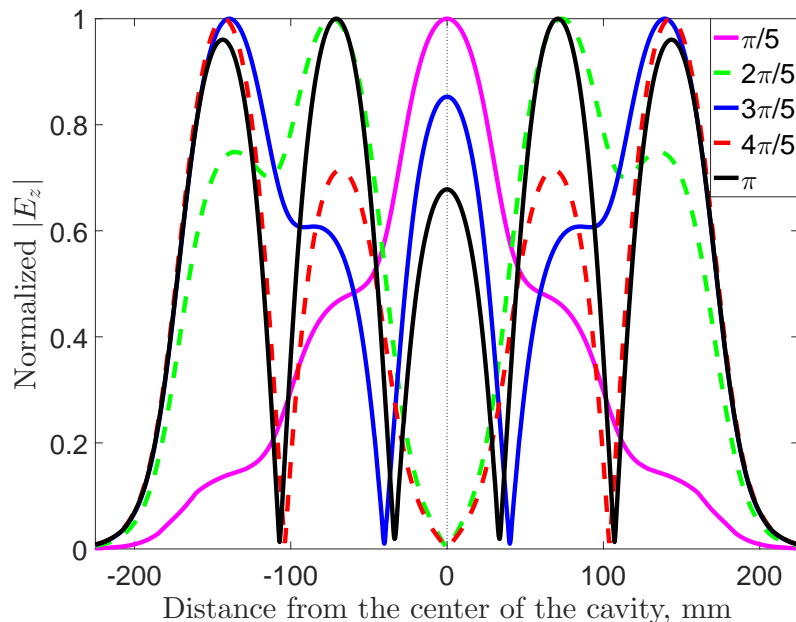


Figure 6-4: Simulated gradient profiles for the 5 passband modes in the five-cell cavity (see the simulation files in Supplemental Materials [4]).

It was found that even when the drive probe was fully inserted into the cavity (strongest coupling), the passband modes were highly undercoupled. In the undercoupled regime, the coupling factor

$$\beta = \frac{Q_0}{Q_{ext}} \quad (6.1)$$

is less than 1. This means that either Q_0 of the modes were much lower than expected, or Q_{ext} were much higher than expected. If the second was true, going to lower cryogenic temperatures would have improved the coupling.

We therefore went to lower temperatures by lowering the pressure inside the cryostat (see Figure 6-1). Despite the minor leak that occurred after the baking and was quickly fixed, the cavity showed no leaks in superfluid helium. According to Equation (2.25), the surface resistance of niobium decreases with lowering the temperature,

hence the unloaded Q-factors of the modes must go up. However, coupling to the cavity's π -mode did not change after going from a helium bath temperature of 4 K to 2 K. This indicated that this mode had a Q-factor dominated by non-superconducting losses.

After the cavity was pulled out of the cryostat, the inside surface of the cavity was inspected with a small movable camera. Examples of photographs taken during the inspection are shown in Figure 6-5. After a thorough investigation, no evident defects were found on the surface.



Figure 6-5: Photographs of the inside of the cavity, taken during the inspection. No visible defects were found.

Longer drive and pickup probes were made for coupling to the low-Q modes (simulated minimum Q_{ext} of the drive probe was 1.1×10^5 when the probe is all the way in). The cavity was reassembled with the new probes in the clean room. Since the inside of the cavity could have been contaminated during the inspection, the cavity was high pressure rinsed, taken out of the clean room, and baked again. The assembly was lowered into the cryostat and immersed in liquid helium. The experiment was then repeated at a helium bath temperature of 4 K.

Even with the new probes, the accelerating mode was still undercoupled. However, this time, we could use the phase lock loop to estimate Q_0 for the π -mode in a pulsed regime. In a pulsed regime, the field in the cavity is not in equilibrium with the input power. At the beginning of an RF pulse, all the input power is reflected. After some time, the reflected power decays and stabilizes at a certain level below

the input power. By measuring the slope of the decay-curve the unloaded Q-factors for the π -mode and the $3\pi/5$ -mode were estimated to be unexpectedly low values: $Q_{0\pi} = 1.6 \times 10^6$, $Q_{03\pi/5} = 9.3 \times 10^5$. The decay curve of the reflected power in the π -mode is shown in Figure 6-6. Because the Q-factors for the two modes were so much lower than expected, it was not possible to feed any significant power into the cavity in these modes.

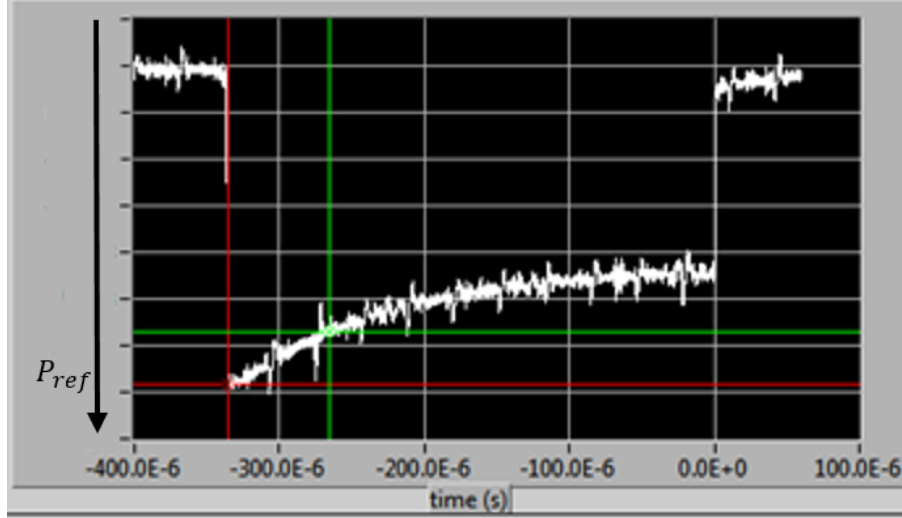


Figure 6-6: Power reflected from the cavity when excited with a pulse at the frequency of the π -mode. Decay time was calculated by measuring the slope of the curve just after the pulse was turned on (by comparing the points given by the intersections of the red and the blue lines). The power is measured in arbitrary units.

The $2\pi/5$ and $4\pi/5$ modes showed much higher Q factors: $Q_{02\pi/5} = 2.2 \times 10^8$, $Q_{04\pi/5} = 2.7 \times 10^8$. For each of these two modes, we were able to adjust the drive probe to have the near-critical coupling ($\beta \approx 1$). We were able to feed up to 135W of power into the cavity and measure Q_0 vs E_{peak} .

Measured values of Q_0 for different modes are plotted in Figure 6-7 as functions of E_{peak} - the peak surface electric field in the corresponding mode. The surface field was used instead of the typically used accelerating gradient in order to compare the relative field levels in modes with very different shunt impedance values. The π -mode and the $3\pi/5$ -mode are only represented by single points in Figure 6-7 because no significant fields were achieved for these modes.

The maximum achievable field in the $2\pi/5$ mode was limited by a quench-like

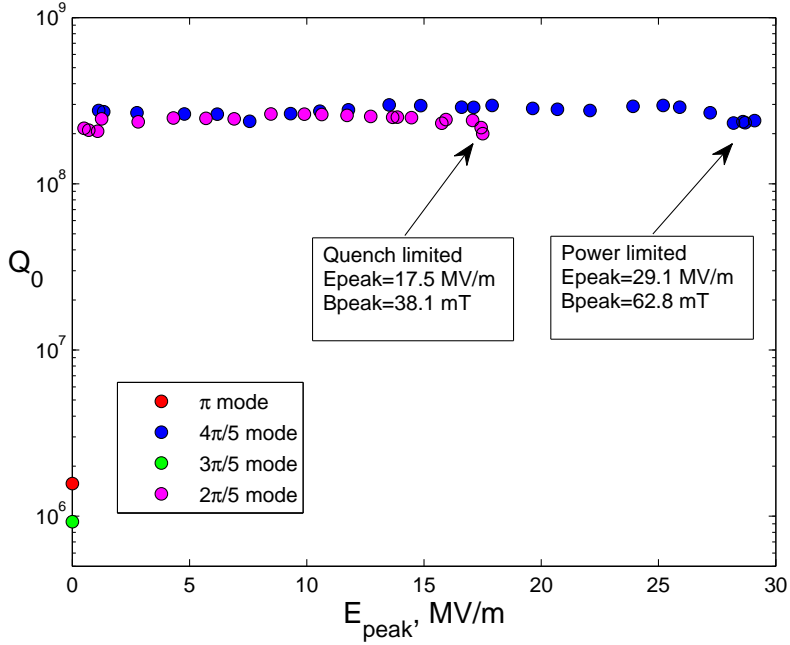


Figure 6-7: Cavity’s quality factor for different modes as a function of the peak surface electric field at 4K. The drive probe was adjusted to provide near critical coupling to the $2\pi/5$ and $4\pi/5$ modes, or max achievable coupling for π and $3\pi/5$ modes.

behavior with the rapid change in reflected power from near zero to 100% and back, as depicted in Figure 2-12. The quench did not cure after a few minutes of conditioning, which indicates that it was a hard barrier. For the $4\pi/5$ mode, several similar quenches were processed and we eventually reached the limit of maximum available input RF power. At the surface field of about 29 MV/m, a rapid increase in X-rays was observed indicating field emission, but was quickly processed. No consistent multipacting barriers were encountered.

Unloaded quality factors, measured for the four passband modes at the temperature of 4K, were compared to corresponding theoretical values. In order to obtain the theoretical values for Q_0 , we used the expression for the BCS resistance R_{BCS} as a function of temperature (Equation (2.25)). The exact value of temperature was 4.0 K at the altitude at LANL, where atmospheric pressure is about 600 Torr. The BCS resistance was estimated to be $1.189 \mu\Omega$ at the temperature of 4.0 K. We also estimated the residual resistance R_0 due to magnetic flux trapped in the walls of the cavity. Using an empirical formula from [78], we found $R_0 \approx 18 \text{ n}\Omega \ll R_{BCS}$ for the

Table 6.1: Theoretical and measured unloaded Q Factors for the passband modes.

Passband mode	Theoretical G	Theoretical Q_0	Measured Q_0
$\pi/5$	220	2.0×10^8	not measured
$2\pi/5$	272	2.4×10^8	2.2×10^8
$3\pi/5$	249	2.1×10^8	9.3×10^5
$4\pi/5$	272	2.3×10^8	2.7×10^8
π	262	2.2×10^8	1.6×10^6

measured value of DC magnetic field. Hence, the residual resistance contribution to the total surface resistance was neglected: $R_s \approx R_{BCS}$.

As discussed in Chapter 3, the unloaded Q-factors can be found from the surface resistance R_s , if the geometry constants G for the modes are obtained (Equation (3.9)). The geometry constants for all five passband modes were calculated in Ansys HFSS. Then, we computed theoretical Q-factors using Equation (3.9) for the modes and compared them to the measured values (Table 6.1). The measured Q-factors for the modes $2\pi/5$ and $4\pi/5$ agreed reasonably well with theoretical predictions while the measured Q-factors for modes $3\pi/5$ and π were about 2 orders of magnitude lower than the prediction. $Q_{0\ 3\pi/5}$ and $Q_{0\ \pi}$ were limited by some losses of non-superconducting nature.

6.2 Identification of the problem and modification to the joint design

The problem with anomalous non-superconducting losses needed to be investigated. In order to understand where the source of the losses was, we looked at gradient profiles for the four modes (Figure 6-4). It can be seen in the plot that the two modes that are not affected by the losses have the small field in the PBG cell, while the two modes with a low Q_0 have a field in the PBG cell comparable in magnitude to fields in the other cells. This was a strong indication that the source of the losses was located in the PBG cell.

On the other hand, SRF PBG single cells have been fabricated previously at

Niowave Inc., and successfully tested and had high Q-factors [63, 64]. This time, we followed a very similar fabricating procedure. The only significant difference was the addition of the waveguide couplers to the periphery of the PBG cell.

As was discussed in Chapter 4, all three waveguides were covered with niobium plates that, once squeezed, were supposed to provide an RF seal (Figure 4-10). The $3\pi/5$ and the π modes were confined inside of the PBG array and had negligible fields at niobium plates that covered the HOM waveguides. However, there was a significant field on the FPC cover due to the removed PBG rod. This made the FPC cover the most likely place to produce the abnormal losses.

Assuming that the FPC joint was indeed the source of the losses, we defined the quality factor associated with just the losses in the joint $Q_{joint} = \omega U / P_{joint}$, where ω is the angular frequency, U is the total energy stored in the cavity and P_{joint} is the power lost in the joint. We could then separate the two contributions to the unloaded Q-factor:

$$\frac{1}{Q_0} = \frac{1}{Q_{cav}} + \frac{1}{Q_{joint}}, \quad (6.2)$$

where Q_{cav} is related to the expected losses in the cavity walls. In the cryogenic experiment Q_0 for the accelerating mode was dominated by the joint losses due to the fact that $Q_{joint} \ll Q_{cav}$. However, the opposite was true for a room-temperature test, since the measured Q-factors in the 10^6 range were much greater than a Q-factor due to normal-conducting losses (in the 10^3 range). This made diagnosing the problem more complicated as, at room temperature, changes in the joint design do not cause any noticeable changes in Q_0 .

In order to avoid doing multiple superconducting experiments to diagnose the problem, an indirect approach involving a trapped waveguide mode was used. It was found that there exists a trapped waveguide mode at 1.777 GHz, localized close to the joint (Figure 6-8). Therefore, while having a field pattern at the joint similar to the π mode, its Q_0 is much more sensitive to changes in joint losses. The mode could be excited with long and bent antennas that were inserted through the beam-pipes of the cavity. Its Q factor was calculated from the width of the transmission (S_{21})

curve.

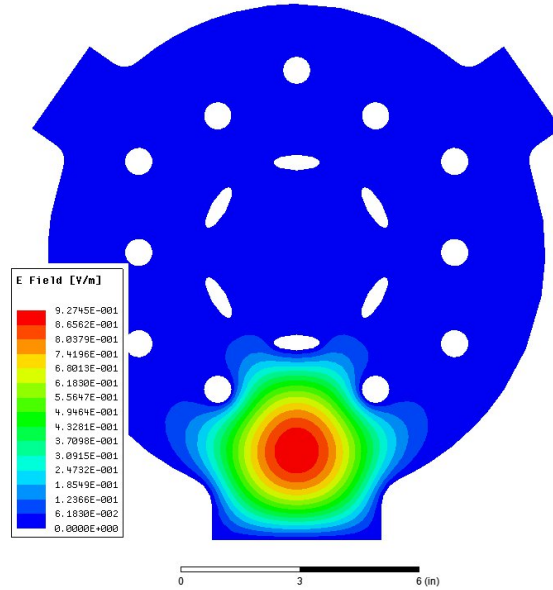


Figure 6-8: Magnitude of the E field of the trapped waveguide mode in a plane that goes through the center of the PBG cell. The mode is an effective tool in diagnosing the low Q problem. The picture is taken from an eigenmode simulation described in Supplemental Materials [9].

The measured Q factors for the trapped mode are summarized in Table 6.2. For the case of zero joint losses, Q_0 (equal to Q_{walls}) can be estimated using niobium conductivity at room temperature $6.57 \times 10^6 \Omega^{-1}$ and the geometry constant $G = 187 \Omega$ of the mode. The measured value, however, was much smaller than that estimate and varied greatly when the niobium cover plate (shown in blue in Figure 4-10) was manually pressed down to the cavity.

This indicated an obvious poor electrical contact between the walls of the cavity and the covering niobium plate. The poor contact was a result of the cover plate only touching the cavity walls at a few points, as opposed to a uniform contact along the entire perimeter. The actual nature of the losses may be related to an oxidation layer of Nb_2O_5 that forms on the surface of niobium.

Once the problem was identified, several different solutions were suggested. The solution that was implemented consisted of two steps. First, an adjustment was made to the depth of the groove for the aluminum gasket. Such adjustment allowed for more

Table 6.2: Theoretical and measured quality factors for the trapped waveguide mode. The theoretical Q_0 is based on the measured conductivity σ and the simulated G constant (see the simulation files in Supplemental Materials [9]).

	Q_0
Expected value for the case of zero joint losses	5710
Measured value for the old (poor) joint	140
Measured value for the new joint	5650

compression of the two gaskets before the two sides of the flange come to contact. The fabrication process of the aluminum gasket was significantly improved so that the difference in its thickness only deviated by 0.002 inches along the entire perimeter.

Second, the shape of the niobium plate was modified to improve the RF contact as the plate is pressed into the cavity. In particular, a narrow “tooth” was added to the plate minimize the area of the niobium gasket that gets compressed when the flange is tightened (Figure 6-9). That way, only a small fraction of the total force against the flange is provided by the niobium gasket, and most force is provided by the aluminum gasket. The new design was shown to work at room-temperature tests. Table 6.2 shows the final Q-factor of the trapped mode. The agreement between the final measured Q-factor and the expectation proved that the problem was solved.

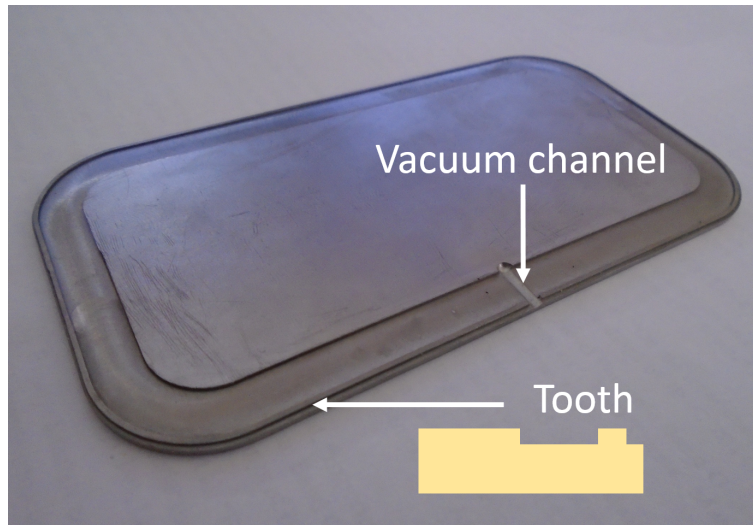


Figure 6-9: The modified niobium gasket used in the FPC joint. A part of the gasket was cut out to form a “tooth” that gets pressed against the flange.

6.3 Second cryogenic testing at Niowave Inc.

After the modifications were made, the cavity underwent another surface treatment that consisted of BCP flash etching and high-pressure rinsing. The cavity was re-tested at Niowave in December of 2015. Besides the improved joint, the cavity was also welded into a titanium helium vessel (the process of welding the cavity into the helium vessel was described in Chapter 4). The cavity in the helium vessel just before the second cryogenic test is shown in Figure 6-10.

Similar to the first experiment at LANL, coupling to the cavity was done through a drive and a pickup probes, located in the beam-pipes. This time, the probes were non-adjustable and did not match the 50Ω impedance of the coaxial lines. The drive antenna was designed to be fairly overcoupled (target coupling $\beta = 5$ for the accelerating mode) in order to have more RF power available for possible processing of multipacting. Indeed, a higher coupling β means that the power generator can be near-critically coupled to the cavity ($Q_{ext} \approx Q_0$) if Q_0 decreases because of multipacting. A solid state 100 W amplifier by Mini Circuits was chosen as the 2.1 GHz RF power source.

This time, no baking was performed prior to the cryotest. The cavity in the helium vessel was placed in the vacuum region of a cryostat, shown in Figure 6-11. A μ -metal shield was used to bring the ambient magnetic field in the cryostat down to 7 mG.

Cavity cooldown proceeded smoothly and without interruption, taking approximately four hours to reach the superconducting transition. Cavity vacuum was maintained below 10^{-8} Torr. Unless otherwise noted, measurements described below were conducted with the helium boiling at atmospheric pressure of 760 Torr ($T=4.2$ K). A temperature sensor attached to upper part of the helium vessel served as a helium level meter. A rise in temperature indicated that the cavity was not fully covered in helium, and the flow of helium would be increased.

Measured pulse decay times were used to calculate loaded Q-factors Q_L at low power levels for all the 5 passband modes (Table 6.3). The obtained values of Q_L for all of the modes agree reasonably well with the expectations based on simulated Q_{ext} and

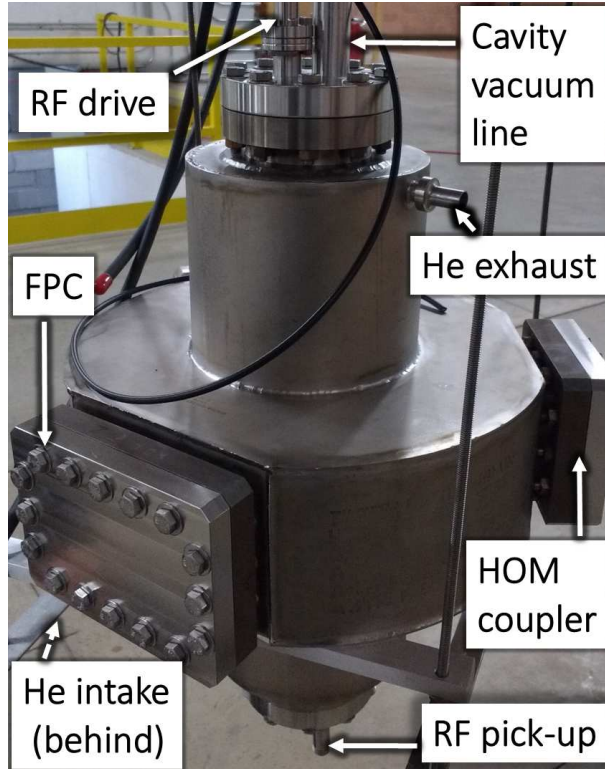


Figure 6-10: A photograph of the 2.1 GHz 5-cell cavity in the helium vessel ready to be placed in a cryostat in preparation for the second cryogenic test.

the BCS model for the surface resistance (equation (2.25)). The residual resistance was neglected, as before. The $\pi/5$ mode was the only undercoupled passband mode due to it having low fields in the end cells, as can be seen in Figure 6-4. Therefore, for the $\pi/5$ mode $Q_L \approx Q_0$, and comparing its Q_L to the expectation was particularly interesting as it could have revealed presence of the anomalous losses observed before. The fact that the measured Q_L for the $\pi/5$ mode agreed well with the expectation, together with the fact that the mode had a significant field in the center cell, proved that the problem of low Q was solved.

The dependence of Q_0 on the accelerating gradient E was measured for the accelerating mode in the CW regime. Forward, reflected, and transmitted power levels (P_f , P_r , P_t), in addition to the Q_L at low power measured before, gave us more than enough data to calculate Q_0 and E . Hence, four different methods were used with a goal of estimating measurement errors by comparing the methods. In one of the methods we used P_t to calculate the energy stored in the cavity, and P_f and P_r to

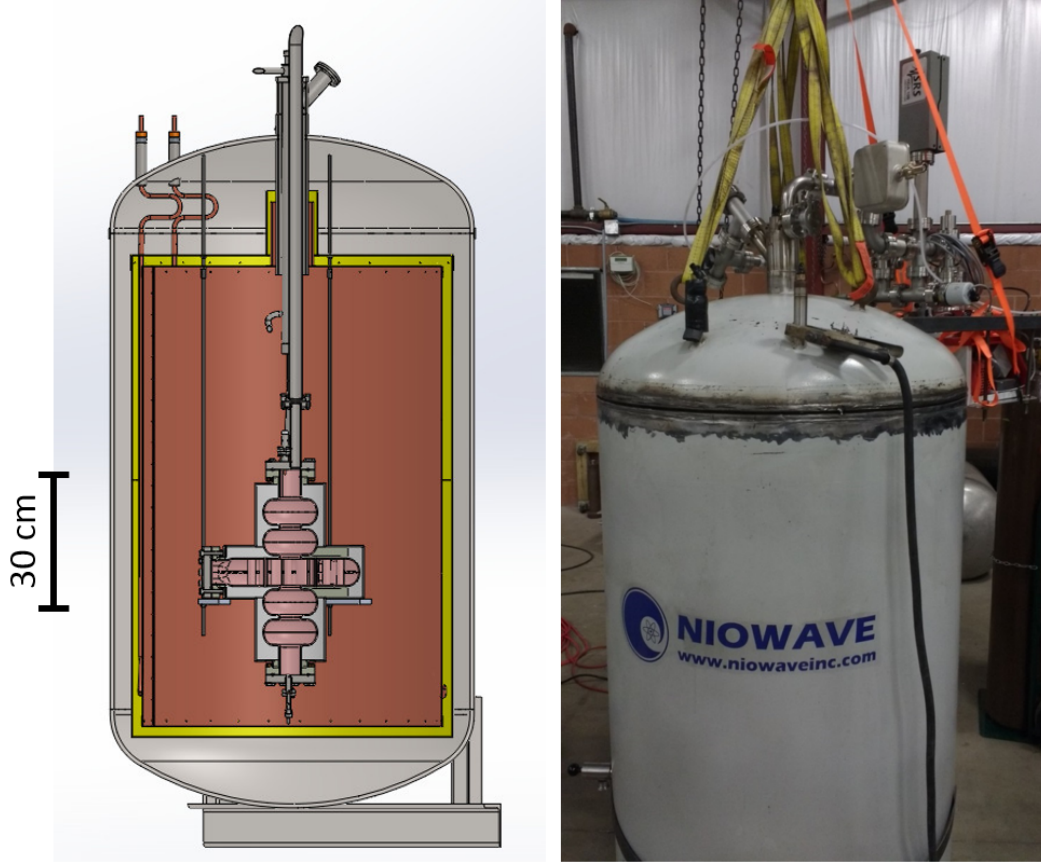


Figure 6-11: A schematic and a photograph of the cryostat used in the second cryogenic test.

calculate Q_0 [31].

In the other three methods, we ignored one of the three measured powers (P_f , P_r , or P_t), and replaced the ignored data with a calculation based on the other two powers and the assumption that Q_{ext} stayed constant throughout the experiment. The methods rely on the fact that the following combination of measured power levels should stay constant throughout the experiment:

$$\frac{Q_{ext}^{pickup}}{Q_{ext}^{drive}} = \frac{P_f}{P_t} \left(1 \pm \sqrt{\frac{P_r}{P_f}} \right)^2 = const, \quad (6.3)$$

where the "+" sign is for the overcoupled regime and the "-" sign is for the undercoupled regime. The relation (6.3) follows from the definitions of Q_{ext}^{pickup} , Q_{ext}^{drive} , Q_0 , and

Table 6.3: Comparison between the low-field Q_L measured at the temperature of 4.2 K and the expected values of Q_L based on the estimated Q_{ext} and Q_0 for different modes.

Mode	Q_{ext} , simulated	Q_0 , simulated	Q_L , simulated	Q_L , measured
$\pi/5$	6.45×10^8	1.50×10^8	1.21×10^8	1.19×10^8
$2\pi/5$	3.87×10^7	1.87×10^8	3.21×10^7	5.54×10^7
$3\pi/5$	2.92×10^7	1.72×10^8	2.50×10^7	4.60×10^7
$4\pi/5$	1.95×10^7	1.87×10^8	1.77×10^7	1.72×10^7
π	2.84×10^7	1.81×10^8	2.45×10^7	2.50×10^7

the following formula for the coupling β [31]:

$$\beta = \left(1 \pm \sqrt{\frac{P_r}{P_f}}\right) / \left(1 \mp \sqrt{\frac{P_r}{P_f}}\right). \quad (6.4)$$

Taking the first data point as an accurate measurement and using the mentioned constant, we computed one of the powers P_f , P_r , or P_t from the other two so that all three powers were self-consistent. We then repeated our calculation of Q_0 and E using the computed power instead of the measured power. The three different ways to construct self-consistent powers gave us the three mentioned methods.

Figure 6-12 shows Q_0 vs E obtained using the four methods together with their average with error bars based on the differences between the methods. The point at $E = 4.6$ MV/m in Figure 6-12 corresponds to the expected value of Q_0 (listed in Table 6.3) assuming no Q-degradation, and the accelerating gradient estimate based on the available RF power and measured losses in the transmission lines. The expected accelerating gradient was not achieved, possibly because of standing wave patterns in the transmission lines that may have limited the RF power delivered to the cavity.

At low power the obtained value of Q_0 was 1.55×10^8 (Figure 6-12), close to the expected value 1.81×10^8 . As forward power was increased, some minimal conditioning was performed. At maximum available RF power, an accelerating gradient of (3.0 ± 0.3) MV/m was achieved. Using the ratios of the cavity's peak surface fields to the accelerating gradient from Table 3.3, the maximum achieved surface fields were found

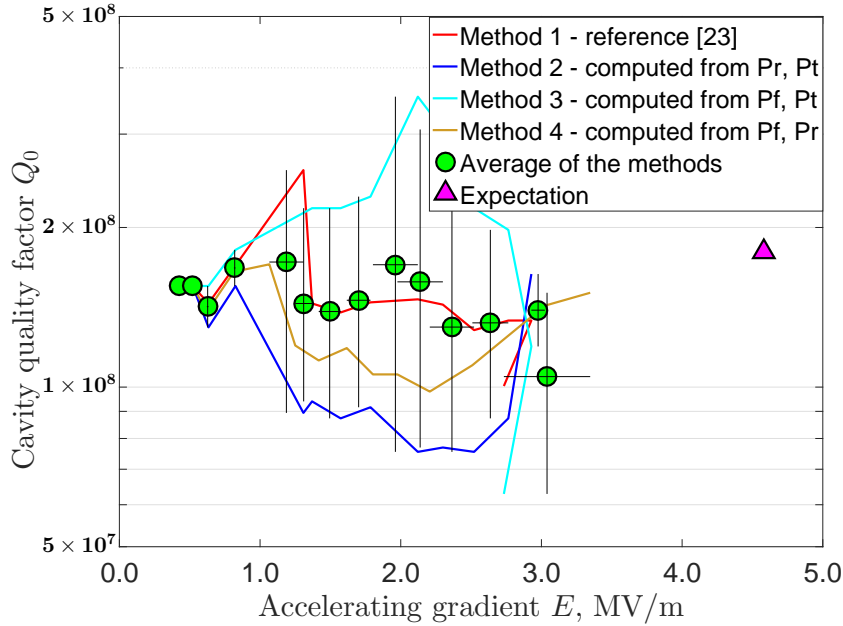


Figure 6-12: Unloaded Q-factor and accelerating gradient in the accelerating mode, obtained during the second test at Niowave Inc. The helium bath temperature was 4.2 K. The point at $E = 4.6$ MV/m corresponds to the expected value of Q_0 (listed in Table 6.3) assuming no Q-degradation, and the accelerating gradient estimate based on the available RF power and measured losses in the transmission lines.

to be $E_{\text{surf}}^{\text{peak}} = (8.0 \pm 0.8)$ MV/m and $B_{\text{peak}}^{\text{surf}} = (13.4 \pm 1.3)$ mT.

The possibility of sub-atmospheric pressure operation was also demonstrated by pumping the helium vessel pressure down to 435 Torr. It corresponds to a helium temperature drop from 4.2K to 3.68K. However, we did not have a chance to operate stably for a long time at this temperature because of the lack of liquid helium.

The fact that the Q_0 for both the $\pi/5$ and the π modes agreed with the expectations indicated that the implemented surface treatment was effective in the cavity. No hard barriers in the accelerating gradient were observed during the test, which indicated the absence of fundamental limits to the cavity's operation for a gradient of at least a few MV/m. No cavity leaks were observed during the tests in superfluid helium.

6.4 Summary

To summarize the chapter, two cryogenic tests were conducted with the fabricated five-cell niobium cavity. The first test was unsuccessful, revealing the problem of a low unloaded Q-factor of the accelerating mode. The problem was traced to a poor waveguide joint and fixed. The second cryogenic test was successful, showing the cavity's operation at the desired Q-factor at accelerating gradients up to a few MV/m. Overall, the tests showed that the cavity is ready to be put in a complete cryomodule assembly. However, the expected accelerating gradient was not achieved, possibly because of standing wave patterns in the transmission lines that may have limited the RF power delivered to the cavity.

Chapter 7

Discussion and future work

7.1 Summary of results

We designed, built, and tested the first SRF multi-cell accelerating cavity with a PBG coupling cell. The cavity was optimized to achieve a more effective HOM damping than conventional multi-cell SRF cavities employing elliptical cells. At the same time, the main accelerating properties of the designed cavity are not significantly compromised. The new design has higher “real-estate” gradient due to the placement of waveguide couplers.

The HOM spectrum in the designed cavity was carefully analyzed using eigenmode and wakefield simulations with good agreement between the two methods. The results of HOM damping simulations are summarized in Figure 7-1 (similar to Figure 3-18 in Chapter 3). Shunt impedances in the left part of the Figure show how strongly the modes interact with the particle beam. The quality factors in the right part of the Figure indicate how well the modes are damped. As can be seen in the plot, most of the high-impedance HOMs are damped to fairly low external Q factors on the order of 10^3 . The green arrows in Figure 7-1 show the Q-factors corresponding to the two highest-impedance dipole modes. Due to the stronger HOM damping, the PBG 5-cell cavity is expected have a much higher BBU current threshold than the TESLA 9-cell cavity, which is an example of a highly-optimized multi-cell SRF cavity. Numerical computations of the BBU threshold are beyond the scope of this thesis work.

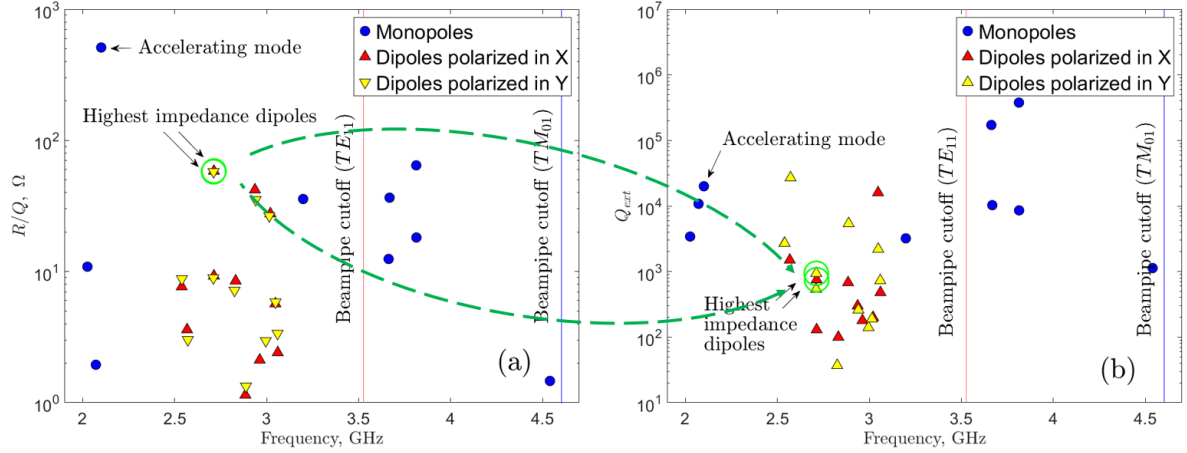


Figure 7-1: Shunt impedances (a) and external Q factors (b) for monopoles and dipoles in the 5-cell PBG cavity (simulation). Most of the high-impedance HOMs are damped to fairly low external Q-factors on the order of 10^3 (the green arrows show the Q-factors corresponding to the two highest-impedance dipole modes). Strong HOM damping means higher achievable beam current in the accelerator.

External Q factors for 6 dangerous HOMs were experimentally measured in the fabricated cavity. The measurements for all but two modes agreed well with the simulations. The two modes for which agreement was not observed demonstrated even stronger damping than was predicted, possibly due to fabrication errors that changed the field patterns of the modes. HOM damping by means of a sliding short was demonstrated, reducing the Q-factor of one of the dangerous modes to 4×10^2 .

The designed 5-cell cavity had one of the most complex shapes among SRF cavity designs (in comparison, for example, with the designs from [27, 42, 43, 44]). Fabrication of the cavity was a challenging task by itself. The most difficult part of the fabrication was electron beam welding of the cavity's joints. Fabrication and tuning mechanisms were successfully tested on a copper prototype and later used for the niobium cavity. The accelerating gradient profile in the tuned cavity matched the desired profile to a 5% accuracy. Chemical surface treatment was done to the niobium cavity to improve its cryogenic performance.

The fabricated cavity was tested at cryogenic temperatures with all ports closed. The first test was unsuccessful due to a problem in an RF joint. The problem was solved and the cavity was successfully re-tested. Some results of the successful test

are shown in Figure 7-2 (similar to Figure 6-12 in Chapter 5). At low power, the obtained value of Q_0 was 1.55×10^8 , close to the expected value 1.81×10^8 . At maximum available RF power, an accelerating gradient of (3.0 ± 0.3) MV/m was achieved, somewhat below the expectation. The corresponding surface fields were found to be $E_{\text{surf}}^{\text{peak}} = (8.0 \pm 0.8)$ MV/m and $B_{\text{peak}}^{\text{surf}} = (13.4 \pm 1.3)$ mT. A possible explanation to why the RF power in the cavity was lower than expected is standing wave patterns in the transmission lines. If this is the case, the problem can be eliminated by using matching 50 Ohm antennas in the cavity, if another experiment is planned.

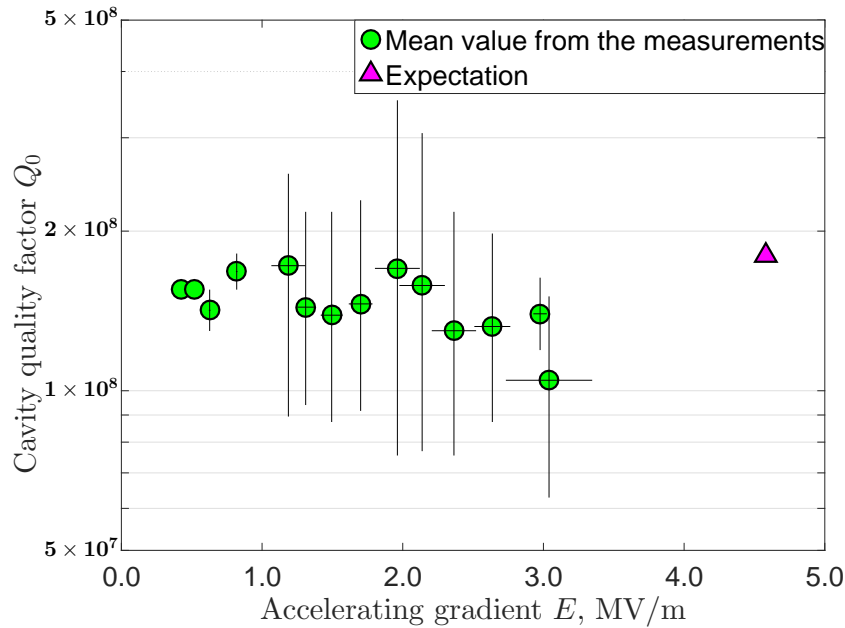


Figure 7-2: Unloaded Q-factor and accelerating gradient in the accelerating mode, obtained during the second cryogenic test. The helium bath temperature was 4.2 K. The point at $E = 4.6$ MV/m corresponds to the expected value of Q_0 assuming no Q-degradation, and the accelerating gradient estimate based on the available RF power. The expected accelerating gradient was not achieved possibly due to some unaccounted losses in the transmission lines. However, the cavity performed as expected (measured Q agreed with the expectation) at the fields up to 3 MV/m.

No cavity leaks were observed during the tests in superfluid helium, proving the reliability of difficult electron-beam welding. The fact that the Q-factor of the accelerating mode agreed with the expectations indicated that the implemented surface

treatment was effective in the cavity of such a complex shape. No hard barriers in the accelerating gradient were observed during the test, which indicated the absence of fundamental limits to the cavity's operation for a gradient of at least a few MV/m.

Overall, there is a long-term benefit for the accelerator community in the development of new structures for high-current, high-intensity accelerators. The designed cavity is promising for increasing the currents in these machines and reducing the length of accelerator required to get to a given energy.

7.2 Future work

More testing needs to be done with the fabricated cavity before it can be employed in real-life experiments. In particular, the HOM measurements and the cryogenic testing can be expanded to a wider range of parameters.

A more thorough HOM measurement can be done if the right equipment is available. The measurements described in Chapter 6 of this thesis only confirm the simulated damping properties in the frequency range of the available network analyzer: from 0 to 3 GHz. It is required to increase the upper-frequency limit to measure the all of the dangerous dipole modes listed in Table 3.4. Simulations and measurements of the quadrupole HOMs can also be added to the analysis.

The maximum accelerating gradient achieved in the second cryogenic testing (Chapter 5) was limited by the available RF power at 2.1 GHz. With a more powerful amplifier, the plot shown in Figure 7-2 can also be extended to higher levels of the accelerating gradient. By doing so, the ultimate performance of the cavity can be measured in terms of the maximum achievable fields. Based on the fact that the designed cavity has accelerating properties similar other multi-cell SRF cavities (Table 3.3), we expect the maximum achievable gradient in the 5-cell cavity to be on the order of 20 MV/m. This gradient can be achieved in a vertical test by using an RF amplifier capable of producing a few hundred Watts of power and going to cryogenic temperatures below 4 K. The latter requires a larger amount of liquid helium but is routinely done in vertical tests (see, for example, [63, 64]). Also, experimental

verification of the high Q-factor of the accelerating mode when the HOM ports have their anticipated dissipative loads (rather than being closed as in the experiments described in Chapter 6) is desirable.

The tests conducted with the 5-cell cavity indicated that the cavity is ready to be put in a cryomodule assembly. The cryomodule assembly was proposed by Niowave Inc. and is schematically shown in Figure 7-3. In addition to the cavity and the helium vessel, the proposed cryomodule comprises a liquid nitrogen cooled thermal shield, two μ -metal magnetic shields, and a steel vacuum vessel. RF loads are placed inside of the cryomodule, but outside of the helium-cooled region. The cryomodule will require an extensive mechanical and cryogenic design.

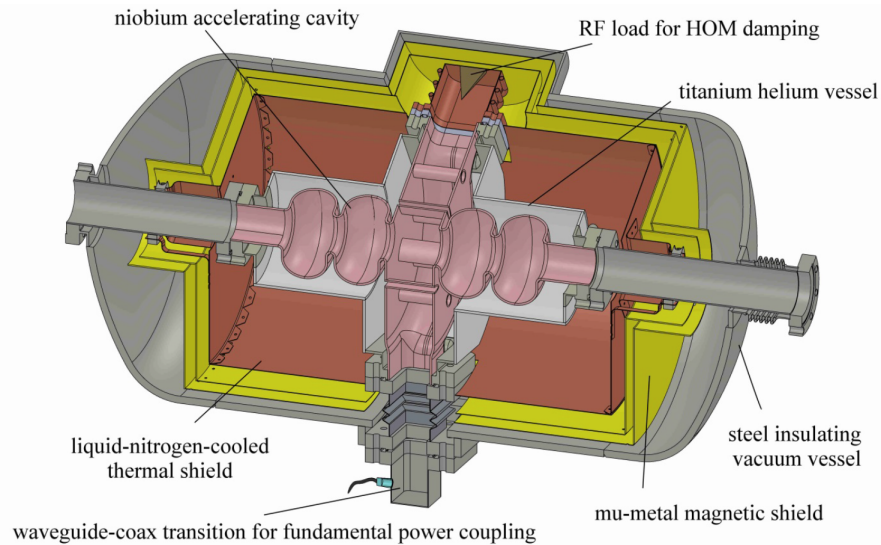


Figure 7-3: A Solid Works drawing of a cryomodule assembly housing the 5-cell cavity, proposed as a continuation of the project.

A possible next step after building the cryomodule is to conduct a “horizontal” test with an electron beam (as described, for example, in [103]). The test will bridge the gap between cryotesting of the cavity in a test dewar and actual use in an accelerator, and will yield useful data with respect to the efficiency of cavity’s cooling. The experiment is proposed by Niowave Inc. to accelerate electron bunches of a small current to the energy of several MeV, limited by the available RF power. An assembly for the proposed experiment is shown in Figure 7-4.

After the demonstration of acceleration, HOM damping performance can be evaluated by driving the cavity with electron bunches of high charge and modulating the beam with different frequencies. Distortion of the beam will be observed on the beam diagnostic as the current approaches BBU limits. These HOM measurements would complete the measurements described in Chapter 6.

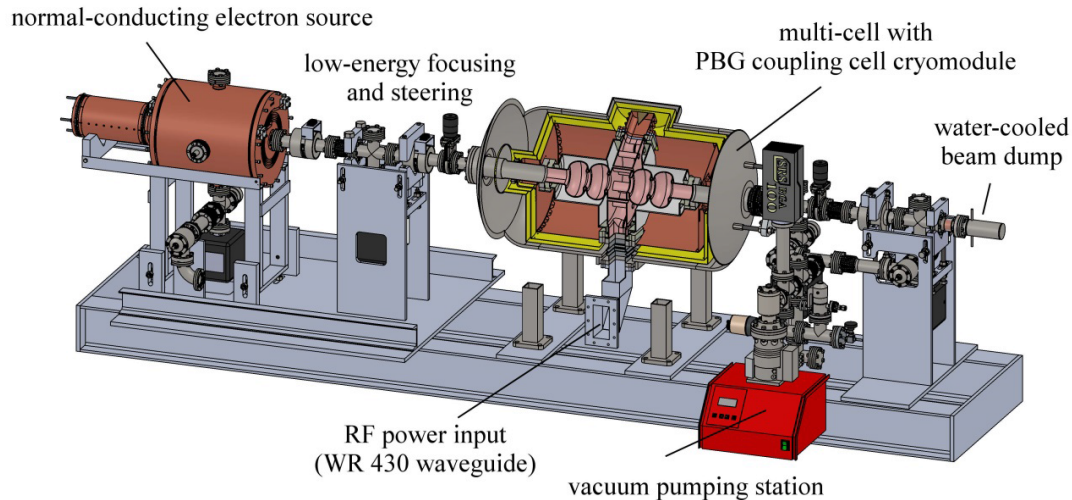


Figure 7-4: Concept of the “horizontal test” to demonstrate acceleration of an electron beam and probe HOM damping.

If the horizontal test is successful, the cryomodule can be used in a real accelerator beamline. One possible application for the cryomodule is a proposed harmonic linac for the electron - relativistic-heavy-ion collider (eRHIC) at Brookhaven National Laboratory [104]. In eRHIC, hadrons from one of the Relativistic Heavy Ion Collider (RHIC) storage rings will interact with electrons accelerated in an eleven-pass superconducting energy recovery linac. One accelerator physics issue being considered in the design is that the nonlinearities of the accelerating linac in the ERL produce a spread in energy which will degrade the polarization of the electron beam. These nonlinearities can be compensated with a harmonic SRF linac at a multiple of the main linac frequency. The 5-cell PBG cavity is viewed as a candidate for the harmonic linac because of its strong HOM damping.

Appendix A

Simulations setup

In this Appendix, setups and choices of parameters for various simulations are discussed in details. In the Thesis, three types of electromagnetic simulations are used: the wakefield simulations, the eigenmode simulations, and the driven modal simulations. The most important examples of simulations of all three types are discussed in the three sections of the Appendix. The actual simulation files can be found in the directories listed in the section Supplemental Materials in the end of the Thesis.

A.1 CST wakefield simulations

In this section, we describe the wakefield simulations mentioned in Section 3.5.1 of this Thesis. The simulations were performed using the CST Wakefield Solver [70]. In a wakefield simulation, electromagnetic fields are driven by a bunch of charged particles, passing the observed structure parallel to the main coordinate axis Z (an example is shown in Figure A-1).

The excited fields are calculated with a time domain solver. The solver computes the electromagnetic fields step by step through time by the so-called “Leap Frog 2” updating scheme. It is proven that this method remains stable if the step width for the integration does not exceed a known limit [70]. This value of the maximum usable time step is directly related to the minimum mesh step width used in the discretization of the structure.

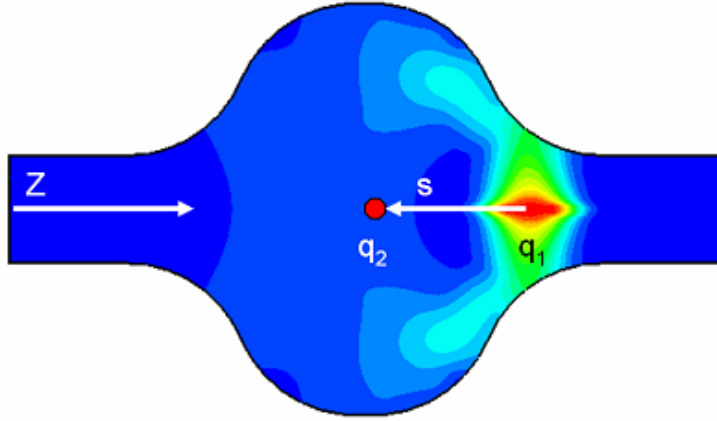


Figure A-1: A diagram of an example wakefield simulation, taken from the CST user manual. The color shows the magnitude of the the electric field.

The CST wakefield solver calculates the longitudinal and the transverse wake potentials $w_{\parallel}(s)$ and $w_{\perp}(s)$ that are used to describe the change of momentum on a test charge, which travels at a distance s behind the excitation bunch, in the structure provided by the user. The wake potentials are formally defined in Equations (2.1) and (2.2). The solver can also be used to compute the Fourier-transform of an obtained wake potential profile to find the longitudinal and the transverse wake impedances defined in Equations (2.3) and (2.4).

In the design environment, there are several features that have to be defined by the user to run the code. Here we describe the most important parameters and list them in Table A.1.

- Structure design

In the structure design environment, 3D shapes can be created to model an RF structure (e.g. an accelerating cavity). Created models are compatible with most CAD software packages. For our simulations, the geometry of the vacuum interior of the cavity was imported from an HFSS simulation (see later in this Appendix). The geometry is shown in Figure A-2.

- Output ports

Three output ports were created for all three waveguides to provide the right

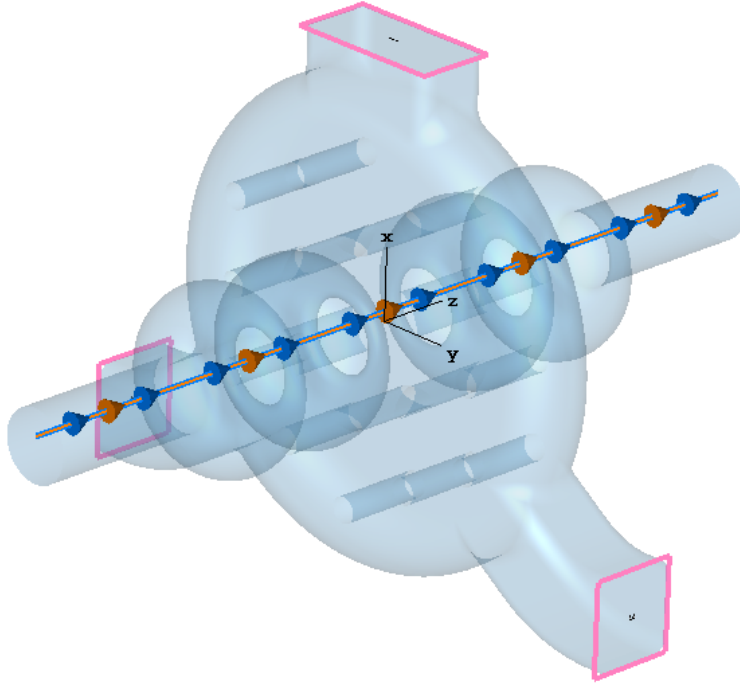


Figure A-2: The structure used in the wakefield simulations. The vacuum region is shown in blue. The waveguide ports are shown with pink lines. The beam path is shown with blue and orange arrows (the path is displaced in X in this picture).

boundary conditions. In CST, ports have to be defined perpendicular to one of the axes (X , Y , or Z). Hence, the HOM waveguides were extended with bent sections of the waveguide, as shown in Figure A-2. The ports are shown in the Figure with pink lines.

- Particle beam

In the described simulations, the particle beam trajectory was defined as a straight line parallel to the Z axis, shifted from the center either in X or in Y directions to excite X or Y -polarized HOMs. Besides the trajectory, an important parameter of the beam is its longitudinal spread σ_z . A shorter bunch can be used to excite modes of higher frequencies, up to $f_{max} \approx c/\sigma_z$ (for ultrarelativistic bunches). However, shorter bunch length requires a finer mesh and, therefore, a more time-consuming simulation. The value of $\sigma_z = 0.2$ inches was chosen ($f_{max} = 59$ GHz) so that excitation of modes with the frequencies

of interest (2 - 5 GHz) is not affected by the non-zero length of the bunch.

- Mesh

A hexahedral mesh is automatically created by the CST wakefield solver. CST's perfect boundary approximation (PBA) allows complex geometries to be simulated with fewer mesh points than is used with a rectangular grid. Dimensions of mesh cells are chosen relative to the wavelength corresponding to the lower limit of the frequency range specified by the user. Different mesh parameters were tested and the mesh was refined until no significant change in the calculated wake potential and impedance was observed.

- Background material

A lossy metal was defined in order to provide an additional mechanism of the energy decay. As was discussed in Section 3.5.1, the value of the energy decay time did not matter to us as long as the peaks of wake impedance did not overlap. Therefore, a lossy metal boundary was defined to save computational time.

- Boundary conditions

No boundary conditions were specified for the described simulations as the full structure was surrounded by the background material.

- Field monitors

Field monitors were defined at the frequencies of the wake impedance peaks. After the monitors were defined, each simulation was run again to obtain the field profiles of the dangerous HOMs.

A.2 HFSS eigenmode simulations

The eigenmode solver of Ansys HFSS [71] was used for the eigenmode simulations described in Chapter 3. In an eigenmode simulation, natural solutions to Maxwell's

Table A.1: Parameters used in the wakefield simulation described in Section 3.5.1.

Particle beam	Relativistic β	1
	Charge, q	1×10^{-12} C
	Longitudinal spread, σ_z	0.2 inches
	Direction	$+Z$
	Transverse displacement	0.25 inches in X or in Y
Waveguide ports	Number of modes, FPC port	3
	Number of modes, HOM port 1	2
	Number of modes, HOM port 2	2
Frequency range	2 - 5 GHz	
Wakefield range, s_{max}	2500 in	
Mesh	Type	Hexagonal PBA mesh
	Lines per wavelength	10
	Lower mesh limit	10
	Mesh line raio limit	10
Background material	Conductivity, σ	5.96×10^4 S/m
	Permeability, μ	1

equations are calculated for a given structure, with the absence of a particle beam or excitation ports. Such solutions are called eigenmodes, or resonances, of the structure.

Here we will describe two kinds of eigenmode simulations that were used in Chapter 3: the 2D simulations (Sections 3.1.3) and the 3D simulations (Section 3.5.2). Ansys HFSS is a three-dimensional solver, so a 3D geometry must be provided by the user. In order to use the solver for effectively 2D simulations, we reduced the length of the structure in the third dimension to merely one mesh cell.

Similar to wakefield simulations, several important parameters have to be defined to run an eigenmode simulation:

- Structure design

HFSS offers a set of basic tools for drawing complex shapes. Simple 3D shapes (sphere, cylinder, etc.) can be added together or subtracted from each other to create the desired vacuum region. In the performed simulations, all dimensions of the created shapes were parameterized to facilitate the optimization process.

- Boundary conditions

Symmetry planes of the simulated structures were used to reduce the simulated volume by cutting the structure and defining an appropriate boundary condition on the cutting plane. The boundaries, used in the simulations, include the perfect E boundary (the electric field is perpendicular to the plane), the perfect H boundary (the magnetic field is perpendicular to the plane), master and slave boundaries (fields at the planes are shifted in phase relative to each other by a certain amount).

- PML volumes

Volumes of the PML material [93] were used to effectively create a no-reflection boundary at the borders of the structures. This feature of the eigenmode solver is useful for calculating external Q-factors, as discussed in Chapter 3.

- Mesh

An automatic tetrahedral mesh was created by the solver. HFSS created an initial mesh that was then refined until the specified accuracy was achieved. Curvilinear mesh elements were applied to the curved surfaces to accurately discretize the complex shapes.

- Eigenmode solver settings

We specified the number of eigenmode solutions to be found with frequencies above the “minimum frequency” (also defined by the user). The solver kept obtaining the solutions and refining the mesh until the converging condition was achieved. The solver stopped when the frequency deviation per one mesh refining step was smaller than the specified value, or the maximum number of steps was achieved.

- Background material

The perfect conductor was used as background material in all eigenmode simulations.

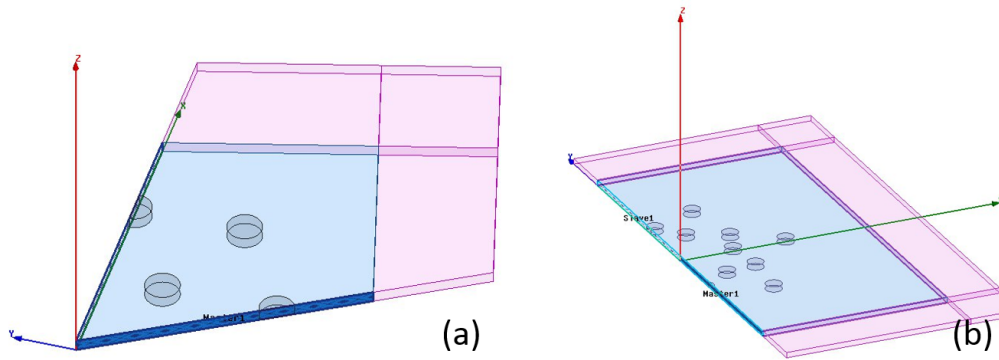


Figure A-3: Geometrical design for the simulations used in Section 3.1.3. A 60° slice of the structure is used to simulate the monopole mode (a), and a 180° slice was used to simulate the dipole mode (b). Vacuum regions are shown in blue. PML volumes are shown in pink. “Master” and “slave” boundary conditions were used with the appropriate phase advances.

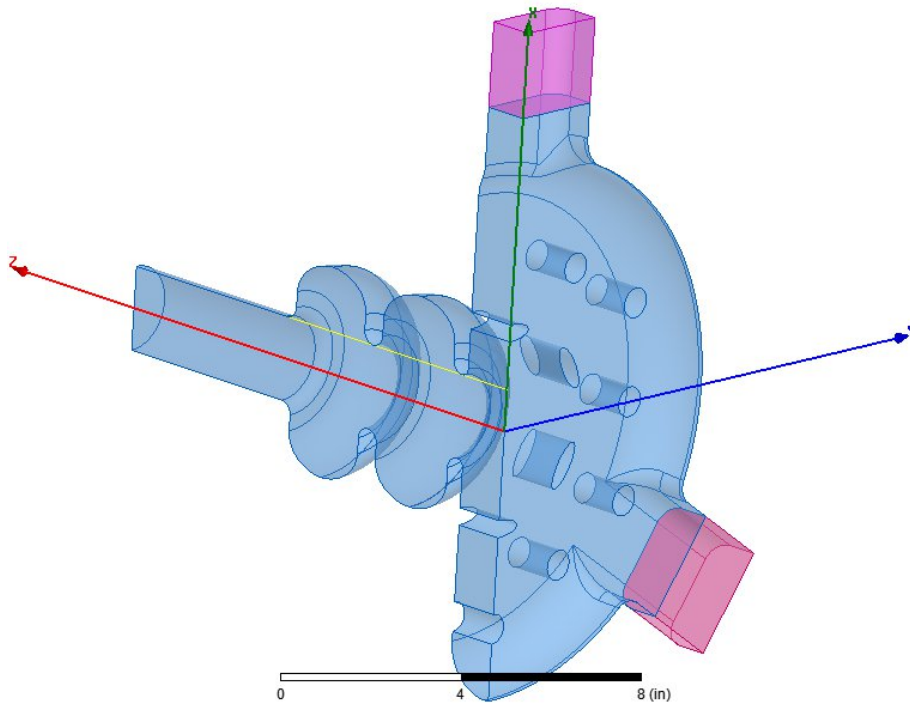


Figure A-4: Geometrical design for the simulations used in Section 3.5.2. A quarter of the structure is simulated to take advantage of the symmetry planes. The waveguides are covered with PML. The yellow line was used for R/Q calculation (see Section 3.5.2).

Table A.2: Parameters for the eigenmode simulations described in Section 3.1.3.

Boundary conditions	Master and slave on the cutting planes	$\Delta\phi = 0$ (monopole)
		$\Delta\phi = \pi$ (dipole)
Perfectly Matched layer (PML)	Thickness	2 inches
	Min frequency	10 GHz
Solver settings	Number of modes	1
	Minimum frequency	11.5 GHz
	Order of basic functions	First
	Maximum Δf per pass	0.1%
Mesh	Type	Auto tetrahedral
	Curvilinear elements	Yes
Background material	Perfect conductor	

Table A.3: Parameters for the eigenmode simulations described in Section 3.5.2.

Boundary conditions	Perfect H on the $X - Z$ cutting plane	for X -modes
	Perfect E on the $X - Z$ cutting plane	for Y -modes
	Perfect H on the $X - Y$ cutting plane	for modes, antisymmetric around the $X - Y$ plane
	Perfect E on the $X - Y$ cutting plane	for modes, symmetric around the $X - Y$ plane
Perfectly Matched layer (PML)	Thickness	2 inches
	Min frequency	2 GHz
Solver settings	Number of modes	1
	Minimum frequency	Depends on the mode
	Order of basic functions	Second
	Maximum Δf per pass	0.0025%
Mesh	Type	Auto tetrahedral
	Curvilinear elements	Yes
Background material	Perfect conductor	

Figures A-3 and A-4 show geometrical setups for the simulations used in the Sections 3.1.3 and 3.5.2, respectively. The parameters for those simulations are listed in Tables A.2 and A.3.

A.3 HFSS driven modal simulations

HFSS “driven modal” (or “network analysis”) simulation is a type of electromagnetic simulation distinct from an eigenmode simulation. A simulated structure is viewed as a network and is analyzed in the frequency domain. Solutions to Maxwell’s equations are found at a frequency (or a set of frequency values - frequency sweep) specified by the user. A source of excitation (e.g. a waveguide port) is necessary to run a driven modal simulation. Driven modal simulations are used for HOM identification in Section 5.2. The geometry for this simulation is shown in Figure A-5.

Parameters needed to run a driven modal simulation are similar to the ones described in Section A.2 for the eigenmode simulation. A few differences are:

- Driven modal solver settings

Solution frequency (or a frequency sweep) are defined by the user. As a convergence criterion, a deviation in S-parameters is used instead of a deviation in frequency. The maximum number of passes and the order of basic functions are defined similarly to the eigenmode settings.

- Excitations

In our simulations, waveguide ports were used as sources of excitation. For the ports, the number of modes needs to be defined together with the so-called “integration line”. A port can be defined on any surface (a cross-section of a coaxial line was used, as shown in Figure A-5).

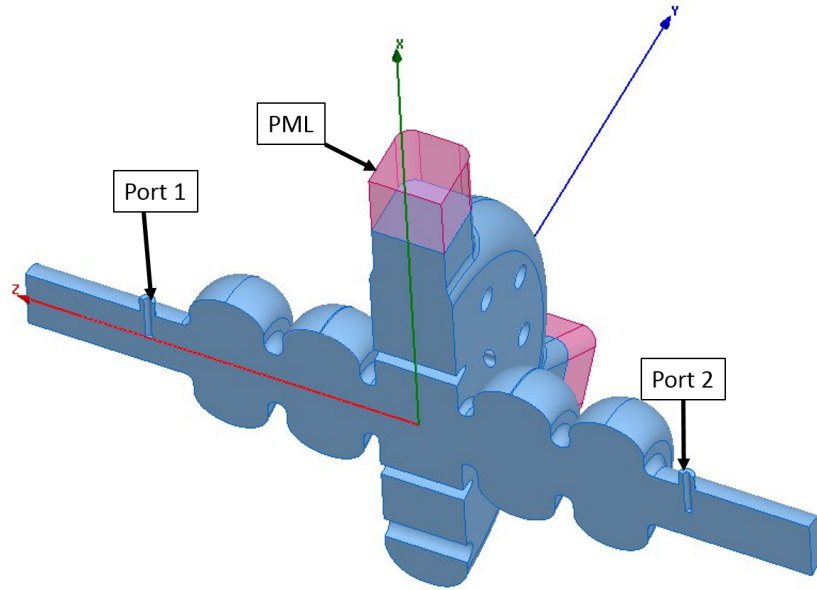


Figure A-5: Geometrical design for the simulations used in Section 5.2. Half of the structure is used in the simulations to take advantage of the $X - Z$ symmetry plane. Vacuum regions are shown in blue. PML volumes are shown in pink. The two ports are defined on the cross-sections of the coaxial lines.

Table A.4: Parameters for the driven modal simulations described in Section 5.2.

Boundary conditions	Perfect H on the $X - Z$ cutting plane	for X -modes
	Perfect E on the $X - Z$ cutting plane	for Y -modes
Perfectly Matched layer (PML)	Thickness	2 inches
	Min frequency	2 GHz
Solver settings	Frequency sweer	2.475 - 3.1 GHz
	Sweep type	Interpolating
	Order of basic functions	Second
	Maximum ΔS per pass	0.0025
	Maximum number of passes	3
Mesh	Type	Auto tetrahedral
	Curvilinear elements	Yes
Background material	Perfect conductor	
Excitations (ports 1 and 2)	Number of modes	1
	Integration line	in Z direction

Bibliography

- [1] G. Aad, T. Abajyan, B. Abbott, and et al. Observation of a new particle in the search for the Standard Model Higgs boson with the ATLAS detector at the LHC. *Physics Letters B*, 716(1):1 - 29, 2012.
- [2] S. Chatrchyan, V. Khachatryan, A.M. Sirunyan, and et al. Observation of a new boson at a mass of 125 gev with the CMS experiment at the LHC. *Physics Letters B*, 716(1):30 - 61, 2012.
- [3] Adrian Cho. The Discovery of the Higgs Boson. 338(6114):1524 - 1525, Dec 2012.
- [4] The Higgs Boson. *Science (New York)*, 338(6114):1558 - 1559, Dec 2012.
- [5] M. Bardeen and et al. Planning the Future of U. S. Particle Physics Report of the 2013 Community Summer Study. Snowmass, Mississippi, 2013.
- [6] M. Tigner: “Does Accelerator-Based Particle Physics have a Future?” *Physics Today*, Jan 2001 Vol 54, Nb 1.
- [7] The ATLAS Collaboration, “Physics at a High-Luminosity LHC with ATLAS”, July 2013, arXiv:1307.7292.
- [8] “CLIC e+e- Linear Collider Studies”, Aug 2012, arXiv:1208.1402.
- [9] ILC Technical Design Report, 12 June 2013.
- [10] R.B. Neal et al, “The Stanford Two-Mile Accelerator”, 1968.
- [11] S.Y. Lee, “Accelerator Physics”, third edition, Wold Scientific.
- [12] Steven J. Russell et al., “Current Status of the MaRIE”, Los Alamos National Laboratory, March 2013.
- [13] Massimo Altarelli et al., “The Technical Design Report (TDR) of the European XFEL”, July 2007.
- [14] “LCLS Strategic Facility Developments Plan”, July 2015.
- [15] “NSLS-II Strategic Plan”, 2015.

- [16] M. Borland, G. Decker, A. Nassiri, M. White, Proceedings of the 2007 Particle Accelerator Conference, Albuquerque, New Mexico, 2007, paper TUPMN089, p. 1121.
- [17] Y.K. Wu, “Overview of Present and Future Compton Photon Sources”, IPAC2012.
- [18] W. Gai, G. Hoffstaetter, M. Hogan, and V. Shiltsev. Accelerator Technology Test-Beds and Test Beams. Snowmass, Mississippi, 2013.
- [19] W.P. Leemans; et al., “Multi-GeV Electron Beams from Capillary-Discharge-Guided Subpetawatt Laser Pulses in the Self-Trapping Regime”. Physical Review Letters 113 (25): 245002.
- [20] M.W. Poole, S. I. Bennett, M. A. Bowler, N. Bliss, J. A. Clarke, D. M. Dykes, R. C. Farrow, C. Gerth, D. J. Holder, M. A. MacDonald, B. Muratori, H. I. Owens, F. M. Quinn, E. A. Seddon, S. I. Smith, V. P. Suller, and N. R. Thompson, in Proceedings of the 2003 Particle Accelerator Conference, Portland, OR, p. 189.
- [21] T. Kasuga et al., in Proceedings of the 2007 Particle Accelerator Conference, Albuquerque, New Mexico, 2007, paper TUPMN044, p. 1016.
- [22] G.H. Hoffstaetter, I.V. Bazarov, D.H. Bilderback, J. Codner, B. Dunham, D. Dale, K. Finkelstein, M. Forster, S. Greenwald, S.M. Gruner, Y. Li, M. Liepe, C. Mayes, D. Sagan, C.K. Sinclair, C. Song, A. Temnykh, M. Tigner, Y. Xie, in Proceedings of the 2007 Particle Accelerator Conference, Albuquerque, New Mexico, 2007, paper MOOBAB02, p. 107.
- [23] E.C. Aschenauer et al., “eRHIC Design Study: An Electron-Ion Collider at BNL”, Dec 2014, arXiv:1409.1633.
- [24] G.H. Hoffstaetter and I. Bazarov, Phys. Rev. Special Topics - Accelerators and Beams, 7:54401, 2004.
- [25] H. Wiedemann, Particle accelerator physics, fourth edition, Springer.
- [26] R.A. Rimmer et al., Proceedings of PAC07 in Albuquerque, NM, USA, paper WEPMS068, p. 2493.
- [27] Z. Liu and A. Nassiri, Phys. Rev. ST Accel. Beams 13:012001, 2010.
- [28] F. Marhauser et al., Proceedings of the 11th EPAC, Genoa, 2008, p. 886, paper MOPP140.
- [29] R. Calaga et al., Proceedings of the 9th EPAC, Lucerne, 2004, p. 1227, paper TUPKF078.
- [30] V. N. Litvinenko et al., Proceedings of the 21st PAC, Knoxville, 2005, p. 2242, paper RPPT032.

- [31] H.Padamsee, J.Knobloch and T.Hays, "RF Superconductivity for Accelerators", WILEY-VCH, Second Edition.
- [32] S. Belomestnykh, *Reviews of Accelerator Science and Technology* 5:147, 2012.
- [33] A. Grassellino et al., "N doping: progress in development and understanding", *Proceedings of SRF2015*, paper MOBA06.
- [34] D.L. Hall et al., "Nb₃Sn cavities: material characterization and coating process optimization", *Proceedings of SRF2015*, paper TUBA04.
- [35] T. Tajima et al, "Status of MgB₂ coating studies for SRF applications", *Proceedings of SRF2013*, Paris, France, paper WEIOB01.
- [36] S. Peggs et al, "ESS Technical Design Report", April 23, 2013.
- [37] R.C. York et al, "FRIB: A new accelerator facility for the production of rare isotope beams", *Proceedings of SRF2009*, Berlin, Germany, paper FROAAU02.
- [38] Niowave Inc, "High-Power Superconducting Electron Linacs for Cargo Scanning Applications", poster on *IPAC2015*, Richmond, WV, USA.
- [39] Niowave Inc, "A Fast Spectrum Neutron Source for Material Irradiation Using a Superconducting Electron Linac", poster on *IPAC2015*, Richmond, WV, USA.
- [40] Terry Grimm et al., "Mo-99 Production Using a Superconducting Electron Linac", Mo-99 Topical Meeting, Washington DC, June 2014.
- [41] TESLA Test Facility Linac Design Report, edited by D. A. Edwards, DESY, 1995.
- [42] H.Sakai, K.Shinoe, T.Furuya, S.Sakanaka, T.Suwada, T.Takahashi, K.Umemori, M.Sawamura, *Proceedings of ERL07 in Daresbury, UK*, p.56.
- [43] M.Liepe, *Proceedings of the 11th Workshop on RF Superconductivity (SRF2003) in Lubeck/Travemunde, Germany*, paper MoP33.
- [44] H.Wang, R.Rimmer, F.Marhauser, *Proceedings of PAC07 in Albuquerque, NM, USA*, paper WEPMS070, p. 2496.
- [45] F. Marhauser, W. Clemens, G. Cheng, G. Ciovati, E.F. Daly, D. Forehand, J. Henry, P. Kneisel, S. Manning, R. Manus, R.A. Rimmer, C. Tennant, H. Wang, *Proceedings of EPAC08 in Genoa, Italy*, paper MOPP140, p. 886.
- [46] John D. Joannopoulos, Steven G. Johnson, Joshua N. Winn, Robert D. Meade, "Photonic crystals. Molding the Flow of Light", Second Edition, Princeton University Press (2008).
- [47] Remo Proietti Zaccaria, "Butterfly wing color: A photonic crystal demonstration", *Optics and Lasers in Engineering*, Volume 76, January 2016, Pages 70-73.

- [48] Astratov, VN; Bogomolov, VN; Kaplyanskii, AA; Prokofiev, AV; Samoilovich, LA; Samoilovich, SM; Vlasov, Yu A (1995), "Optical spectroscopy of opal matrices with CdS embedded in its pores: Quantum confinement and photonic band gap effects", *Il Nuovo Cimento D* 17 (11-12): 1349-1354.
- [49] <https://en.wikipedia.org/wiki/Opal>
- [50] E.I. Smirnova, C. Chen, M.A. Shapiro, J.R. Sirigiri, and R.J. Temkin. *J. of Appl. Phys.*, 91(3):960, 2002.
- [51] J.Zhang, A.M.Cook, B.J.Munroe, M.A.Shapiro, R.J.Temkin, H.Xu, *Proceedings of IPAC 2015 in Richmond, VA, USA*, paper WEPWA062, p. 2646.
- [52] Brian J. Munroe, "Experimental studies of Novel Accelerator Structures at 11 GHz and 17 GHz", PhD thesis, MIT, 2015.
- [53] C.A.Bauer, G.R.Werner, J.R.Cary, *J. Appl. Phys.* 104, 053107, 2008.
- [54] E. A. Nanni. A 250 GHz photonic band gap gyrotron amplifier. PhD thesis, MIT, 2013.
- [55] J. Hummelt et al, "Overmoded traveling wave tubes for MM and THz applications", proceedings of 2015 40th International Conference on Infrared, Millimeter and Terahertz Waves (IRMMW-THz). Hong Kong, China.
- [56] E.I. Smirnova, A.S. Kesar, I. Mastovsky, M.A. Shapiro, and R.J. Temkin, *Phys. Rev. Lett.*, 95(7):074801, 2005.
- [57] Roark A. Marsh, "Experimental study of photonic band gap accelerator structures", PhD thesis, MIT, 2009.
- [58] Roark A. Marsh, Michael A. Shapiro, Richard J. Temkin, Valery A. Dolgashev, Lisa L. Laurent, James R. Lewandowski, A. Dian Yeremian, and Sami G. Tantawi, "X-band photonic band-gap accelerator structure breakdown experiment". *Physical Review Special Topics - Accelerators and Beams*, 14(2):021301, February 2011.
- [59] Brian J. Munroe, Alan M. Cook, Michael A. Shapiro, Richard J. Temkin, Valery A. Dolgashev, Lisa L. Laurent, James R. Lewandowski, A. Dian Yeremian, Sami G. Tantawi, and Roark A. Marsh, "High power breakdown testing of a photonic band-gap accelerator structure with elliptical rods. *Physical Review Special Topics*" - *Accelerators and Beams*, 16(1):012005, January 2013.
- [60] E.I. Simakov, S.A.Arsenyev, C.E.Buechler, R.L.Edwards, W.P.Romero, M.Conde, G.Ha, J.G.Power, E.E.Wisniewski, C.Jing, *Physical Review Letters*, 116, 064801 (2016).
- [61] D.R. Smith, D. Li, D.C. Vier, N. Kroll, and S. Schultz, *AIP Conf. Proc.*, 398:518, 1997.

- [62] M.R. Masullo, M. Panniello, V.G. Vaccaro, A. Andreone, E. Di Gennaro, F. Francomacaro, G. Lamura, V. Palmieri, and D. Tonini, Proceedings of the 2006 European Particle Accelerator Conference, p.454, MOPCH167, 2006.
- [63] E.I.Simakov, W.B.Haynes, M.A.Madrid, F.P.Romero, T.Tajima, W.Tuzel, C.H.Boulware, T.L.Grimm, Phys. Rev. Lett. 109, 164801 (2012).
- [64] E.I. Simakov, S.A. Arsenyev, W.B. Haynes, D.Yu. Shchegolkov, N.A. Suvorova, T. Tajima, C.H. Boulware, T.L. Grimm, Appl. Phys. Lett. 104, 242603 (2014).
- [65] TESLA Technical Design Report, edited by R. Brinkmann et al., DESY, 2001.
- [66] M. Liepe, "Superconducting RF for the Cornell energy-recovery-linac main linac", Proceedings of SRF2011, Chicago, IL USA, paper MOPO016.
- [67] T.P.Wangler, "RF Linear Accelerators", WILEY-VCH, Second Edition.
- [68] T. Weiland and R. Wanzenberg, Fontiers of Particle Beams: Intensity Limitations, Proc. Joint U.S.-CERN School of Particle Accelerators at Hilton Head Island, Lecture Notes Phys. 400.
- [69] K. Bane and M. Sands. Wakefields of very short bunches in an accelerating cavity. SLAC-PUB-4441, (November), 1987.
- [70] Computer Simulation Technology, CST Particle Studio, www.cst.com.
- [71] ANSYS, Ansys Inc., www.ansys.com.
- [72] G.H. Hoffstaetter, I.V. Bazarov and C.Song, Phys. Rev. ST Accel. Beams 10:044401, 2007.
- [73] Evgenya I. Smirnova. Novel Photonic Band Gap Structures for Accelerator Applications. PhD thesis, MIT, 2005.
- [74] J.Zhang, "Experimental Studies of Hybrid Photonic Band Gap Accelerator Structures", PhD thesis, MIT, 2016.
- [75] H. K. Onnes, Electrician 67, 657 (1911).
- [76] J. Bardeen et al., Phys. Rev., 108:1175 (1957).
- [77] J. Halbritter, Z. Physic, 238:466-476 (1970).
- [78] B. Piosczyk, P. Kneisel, O.Stoltz, and J. Halbritter, IEEE Transactions on Nuclear Science, 20:108, 1973.
- [79] H. A. Schwettman, J. P. Turneure, and R. F. Waites, J. Appl. Phys. 45, 914 (1974).
- [80] J. Knobloch, IEEE Transactions on Applied Superconductivity 9, 1016 (1999).

- [81] R. H. Fowler and L. Nordheim, Proc. Roy. Soc. London A 119, 173 (1928).
- [82] R.A. Marsh, B.J. Munroe, M.A. Shapiro, and R.J. Temkin, Proceedings of the 2009 US Particle Accelerator Conference, WE6RFP081, 2009.
- [83] B.J. Munroe, R.A. Marsh, M.A. Shapiro, and R.J. Temkin, Proceedings of the 2010 International Particle Accelerator Conference, THOD063, 2010.
- [84] B.J. Munroe, A.M. Cook, M.A. Shapiro, R.J. Temkin, V.A. Dolgashev, L.L. Laurent, J.R. Lewandowski, A.D. Yeremian, S.G. Tantawi, and R.A. Marsh, Phys. Rev. ST Accel. Beams 16:012005, 2013.
- [85] E.I. Simakov, S.S. Kurennoy, J.F. O'Hara, E.R. Olivas, and D.Yu. Shchegolkov, Phys. Rev. Special Topics - Accelerators and Beams 17, 022001, 2014.
- [86] P. Kneisel et al., PAC05, p. 4012.
- [87] P. Kneisel et. el, Proceedings of PAC07, Albuquerque, NM, USA, paper WEPMS063, p. 2487.
- [88] R. Rimmer et. el, Proceedings of PAC09, Vancouver, BC, Canada, paper WE5PFP056, p. 2130.
- [89] F. Marhauser et. el, Proceedings of EPAC08, Genoa, Italy, paper MOPP140, p. 886.
- [90] R. Rimmer et. el, Proceedings of IPAC 2010, Kyoto, Japan, paper WEPEC076, p. 3052.
- [91] R. Rimmer et. el, Proceedings of PAC07, Albuquerque, NM, USA, paper WEPMS068, p. 2493.
- [92] S.A.Arsenyev and E.I.Simakov, Proceedings of AAC2012 in Austin, Texas, USA, AIP Conf. Proc. 1507, 425 (2012).
- [93] S.G. Johnson, "Notes on Perfectly Matched Layers (PMLs)", www.math.mit.edu.
- [94] D.A.Goldberg and R.A.Rimmer, IEEE Conference Proceedings of the 1993 Particle Accelerator Conference, vol. 2, p. 871.
- [95] Haipeng Wang et al, "CRAB cavity and cryomodule prototype development for the advanced photon source", WEOCS7, Proceedings of PAC 2011.
- [96] W.Hartung et al, "Niobium Quarter-Wave Resonator Development for the Rare Isotope Accelerator", TUP14, Proceedings of SRF 2003.
- [97] L.Monaco et al, "Experimental and theoretical analysis of the TESLA-like SRF cavity flanges", MOPCH170, Proceedings of EPAC 2006.

- [98] Binping Xiao, Luis Alberty, Sergey Belomestnykh, Ilan Ben-Zvi, Rama Calaga, Chris Cullen, Ofelia Capatina, Lee Hammons, Zenghai Li, Carlos Marques, John Skaritka, Silvia Verdu-Andres, and Qiong Wu, Phys. Rev. ST Accel. Beams 18, 041004 - Published 28 April 2015.
- [99] Haipeng Wang et. al., Proceedings of PAC 2011 in New York, NY, USA, paper WEOCS7, p. 1472.
- [100] Y.Yamamoto, H.Hayano, E.Kako, S.Noguchi, T.Shishido, K.Watanabe, Nuclear Instruments and Methods in Physics Research A 729 (2013) 589 - 595.
- [101] T. Tajima, K.C.D. Chan, R.L. Edwards, R.C. Genzlinger, W.B. Haynes, J.P. Kelley, F.L. Krawczyk, J.E. Ledford, M.A. Madrid, D.I. Montoya et al., Proceedings of SRF2001 in Tsukuba, Japan, paper PH002, p. 578.
- [102] E.L.Ginzton, "Microwave Measurements", Literary Licensing, LLC, 2012.
- [103] E. Harms, K. Carlson, B. Chase, E. Cullerton, A. Hocker, C. Jensen, P. Joireman, A. Klebaner, T. Kubicki, M. Kucera et al., Proceedings of 15th International Conference on RF Superconductivity (SRF2011). 25-29 Jul 2011. Chicago, Illinois, USA, pp 4.
- [104] S.Belomestnykh, I.Ben-Zvi, Y.Hao, V.Litvinenko, V.Ptitsyn, Wencan Xu, Proceedings of IPAC 2014 in Dresden, Germany, paper TUPME084, p. 1547.

Supplemental materials

These supplemental materials contain the actual simulation files referenced throughout the thesis. A manual is provided with each simulation, containing instructions on how to use them. The materials are stored on a server of the library of the Plasma Science and Fusion Center (PSFC) at Massachusetts Institute of Technology. The files can be accessed within the PSFC by the following link http://library.psfc.mit.edu/catalog/restricted/theses/arsenyev/Supplemental_materials/. In the directory, the materials are stored as follows:

- [1] Supplemental_materials/Eigenmode_lattice_optimization
- [2] Supplemental_materials/Eigenmode_3D_design
- [3] Supplemental_materials/Eigenmode_circuit_model
- [4] Supplemental_materials/Eigenmode_HOM_simulations
- [5] Supplemental_materials/MATLAB_3D_optimization
- [6] Supplemental_materials/Wakefield_simulations
- [7] Supplemental_materials/MATLAB_Z_fit
- [8] Supplemental_materials/MATLAB_circuit_model
- [9] Supplemental_materials/Eigenmode_trapped_mode
- [10] Supplemental_materials/Drawings
- [11] Supplemental_materials/Driven_modal_identifying_HOMs

Please contact the author of this thesis (sergejs@alum.mit.edu) with any questions about the materials.